

Sensitivity of solar cells

Von der Fakultät für Mathematik und Physik
der Gottfried Wilhelm Leibniz Universität Hannover
zur Erlangung des Grades

Doktor der Naturwissenschaften

– Dr. rer. nat. –

genehmigte Dissertation von

Dipl.-Phys.

Matthias Müller

geboren am 26. Juli 1983 in Meiningen

2014

Referent: 1. PD Dr. Pietro P. Altermatt

Korreferent: 2. Prof. Dr. Herbert Pfnür

Korreferent: 3. Prof. Dr. Achim Schulze

Tag der Promotion: 18. Juli 2014

Юле

Abstract

The success of a solar cell concept in mass production depends not only on the realized cell efficiency, but crucially on the stability of the fabrication process, i.e. on the distribution of the current–voltage (I–V) parameters. In this work, such distributions are modeled using two- or three-dimensional full-size device simulations of Al-BSF and passivated emitter and rear (PERC) solar cells. The number of these time-consuming simulations is drastically reduced by changing all input parameters concurrently in a Design of Experiment (DoE) approach. A simple polynomial response surface methodology (RSM) model is obtained from these simulations by regression analysis. The RSM contains all the mutual non-linear interactions between the device parameters, and is therefore called a metamodel. The metamodel is applied in order to: 1) find maximum efficiency; 2) compute how sensitively each device parameter influences the I–V parameters; 3) explain, predict, and manipulate the distribution of the I–V parameters in mass production; and 4) find an optimum starting point for experiments. On the example of the SolarWorld Al-BSF solar cell production, it is shown (i) how to analyze data from mass production, and (ii) how to obtain a physical interpretation of the observed variations. This enables one (iii) to decide on strategies for reducing these variations and herewith to improve production yield. I successfully model the observed production variations and successfully track down main causes for these variations. On the example of a PERC concept, it is demonstrated how the choice of the distance between the rear local point contacts leads to either maximal median efficiency but with a broad distribution, or to a slightly reduced median cell efficiency but with a narrower distribution and a reduced number of bad cells.

The development of PERC solar cell concepts requires improved characterization techniques and evaluation schemes. Solar cells can be fabricated with different emitters, i.e. different diffusions, underneath and between the front contacts, which is then called a selective emitter. To account for different emitter recombination behavior, a method is developed to measure the emitter saturation current density J_{0e} with lateral resolution. The method uses PL lifetime imaging at several injection densities to laterally evaluate J_{0e} by applying the method of Kane and Swanson pixel by pixel. The method is successfully applied to investigate the dependence of J_{0e} on the laser power of a selective emitter structure, where the expected behavior of a maximum J_{0e} for medium laser intensities is observed. The method is suitable to evaluate the selective emitter process and its optimization.

For the characterization of the contact resistance on selective emitters with the transfer length method (TLM), two diffusions with different sheet resistances require an adjusted evaluation. I present a test structure and its model to separate the sheet resistances of both diffusions and the contact resistivity within one TLM measurement.

The rear side of screen-printed PERC solar cells is locally contacted. Two methods for determining the Si/Al rear contact resistance are analyzed and improved: the series resistance analysis and the transfer length method (TLM). An experimental set of PERC solar cells with varying metallization fraction is used, and the experiment is analyzed using numerical device simulations. In the first method, the resistive losses are extracted from the I-V-curves of the PERC cells, and the rear contact resistance is separated by subtracting the analytically calculated base contribution. The state-of-the-art analytical calculations of the base resistance deviate significantly from my numerical simulations, causing such a high level of uncertainty that I do not recommend this method. An upper limit of the rear contact resistance per line contact is determined to be about $2 \Omega\text{cm}$. In the second method, the rear line contacts are separated and measured with the TLM. Still, the series resistance loss in the base has to be quantified considering a thick base and the rear line contact geometry. I separate the base component by numerical device simulations and find that the rear contact resistance per line contact is below $0.5 \Omega\text{cm}$. This implies that rear contact resistance reduces cell efficiency of screen-printed PERC solar cells only by about $0.1\%_{\text{abs}}$ for metallization fractions higher than 3.5%, i.e. the rear contact resistance causes no significant loss in the investigated PERC solar cells currently. All of my improved evaluations lead to lower resistance values than previously reported and to a reduced uncertainty. The TLM method is therefore suggested to be favorable.

Keywords:

Crystalline silicon solar cell, PERC, Selective emitter, Sensitivity analysis, Metamodeling, TLM, contact resistance, emitter saturation current density

Zusammenfassung

Der Erfolg eines Solarzellenkonzeptes in der Massenfertigung hängt nicht nur von der erreichbaren Zelleffizienz ab, sondern auch entscheidend von der Stabilität des Herstellungsprozesses, d. h. von der Verteilung der Strom-Spannungs-Parameter (I–V). In dieser Arbeit werden solche Verteilungen modelliert. Zwei- oder dreidimensionale Bauelementesimulationen von „Al-BSF“ und „passivated emitter and rear cell“ (PERC) Solarzellen werden dazu verwendet. Die Anzahl dieser zeitaufwendigen Simulationen wird drastisch reduziert, indem alle Eingangsparameter gleichzeitig in einem „Design of Experiment“ (DoE) Ansatz variiert werden. Ein einfaches polynomisches „response surface methodology“ (RSM) Modell wird aus diesen Simulationen durch Regressionsanalyse erhalten. Das RSM enthält alle gegenseitigen und nichtlinearen Wechselwirkungen zwischen den Eingangsparametern, und wird daher als Metamodell bezeichnet. Das Metamodell wird genutzt, um 1. die maximale Effizienz zu finden, um 2. die Sensitivität jedes Eingangsparameters auf die I–V Parameter zu bestimmen, um 3. die Verteilung der I–V Parameter in der Massenproduktion zu erklären, vorherzusagen und zu manipulieren, und um 4. einen optimalen Ausgangspunkt für Experimente zu finden. Am Beispiel der Al-BSF Produktion der SolarWorld wird gezeigt, wie man 1. Daten aus der Massenproduktion analysiert, wie man 2. eine physikalische Interpretation der beobachteten Schwankungen erlangt. Dadurch wird es 3. ermöglicht, Strategien zu erhalten, um diese Variation zu reduzieren, was die Produktionsausbeute erhöht. Die beobachteten Produktionsschwankungen wurden erfolgreich modelliert und die Hauptursachen für die Variationen konnten bestimmt werden. Am Beispiel eines PERC-Konzepts wird gezeigt, wie die Wahl des Abstandes zwischen den lokalen Rückseitenpunktkontakten entweder zu maximaler Median-Effizienz mit einer breiten Verteilung führt, oder zu einer leicht reduzierten Median-Zelleffizienz, aber mit einer engeren Verteilung und somit einer reduzierten Anzahl von Zellen, die einen Mindestwirkungsgrad unterschreiten.

Die Entwicklung des PERC-Solarzellenkonzeptes erfordert verbesserte Charakterisierungstechniken und Auswerteverfahren. Solche Solarzellen können mit selektiven Emittern, d.h. verschiedenen Diffusionen unter und zwischen den Frontkontakten, hergestellt werden. Um diesem unterschiedlichen Emitter-Rekombinations-Verhalten Rechnung zu tragen, wurde ein Verfahren entwickelt, um die Emittersättigungsstromdichte J_{0e} mit lateraler Auflösung zu messen. Das Verfahren verwendet kalibrierte PL Lebensdauerbilder bei verschiedenen Injektionsdichten, so dass J_{0e} durch Anwendung des Verfahrens von Kane und Swanson Pixel für Pixel bestimmt werden kann. Die Methode wurde erfolgreich eingesetzt, um die Abhängigkeit von J_{0e} von der Laserleistung einer selektiven Emitterstruktur zu untersuchen, wobei das erwartete

Verhalten von maximalem J_{0e} für mittlere Laserintensitäten beobachtet wurde. Das Verfahren ist geeignet, um selektive Emitterprozesse und deren Optimierung zu beurteilen. Zur Charakterisierung des Kontaktwiderstandes auf selektiven Emittern mit der Transferlängenmethode (TLM), wird das TLM-Modell angepasst, um den zwei Diffusionen mit unterschiedlichen Schichtwiderständen Rechnung zu tragen. Eine verbesserte Teststruktur und ihr TLM-Modell wird vorgestellt, um die Schichtwiderstände der beiden Diffusionen und den Kontaktwiderstand innerhalb nur einer TLM-Messung zu separieren.

Die Rückseite von Siebdruck-PERC Solarzellen wird lokal kontaktiert. Zwei Verfahren zur Bestimmung des Si/Al Rückseitenkontaktwiderstandes werden analysiert und verbessert: die Serienwiderstandanalyse und die Transferlängenmethode (TLM). Eine Gruppe von experimentell hergestellten PERC Solarzellen mit unterschiedlichen Metallisierungsgraden werden hierzu verwendet, wobei die Experimente unter Verwendung numerischer Simulation analysiert werden. Bei dem ersten Verfahren werden die Widerstandsverluste der PERC-Zellen aus den I-V Kurven extrahiert, und der Rückseitenkontaktwiderstand durch Subtraktion des analytisch berechneten Basisbeitrags getrennt. Aktuelle analytische Gleichungen weichen erheblich von den gezeigten numerischen Simulationen ab, was zu einer hohen Unsicherheit in der Kontaktwiderstandsbestimmung führt. Die Methode der Serienwiderstandanalyse kann nicht empfohlen werden. Eine obere Grenze des Rückseitenkontaktwiderstands pro Linienkontakt wurde zu ca. $2 \Omega\text{cm}$ bestimmt. Bei dem zweiten Verfahren wird der ganzflächige Rückseitenkontakt elektrisch getrennt und mit dem TLM Verfahren gemessen. Jedoch muss der Serienwiderstandsverlust in der Basis quantifiziert werden, wobei eine dicke Basis und die Rückseitenlinienkontaktgeometrie berücksichtigt werden muss. Die Basiskomponente wird durch numerische Simulationen der TLM Teststruktur separiert und der Rückseitenlinienkontaktwiderstand zu kleiner als $0,5 \Omega\text{cm}$ bestimmt. Dies bedeutet, dass der Rückseitenkontaktwiderstand den Zellwirkungsgrad von Siebdruck-PERC Solarzellen nur um etwa $0,1 \%_{\text{abs}}$ für Metallisierungsanteile höher als $3,5 \%$ reduziert, d.h. der Rückseitenkontaktwiderstand ist kein signifikanter Verlustmechanismus in den untersuchten PERC Solarzellen. Alle gezeigten, verbesserten Auswertungen führen zu kleineren Widerstandswerten als bisher in der Literatur berichtet und können mit einer reduzierten Unsicherheit bestimmt werden. Die TLM Methode wird daher empfohlen.

Schlagwörter:

Kristalline Silizium-Solarzelle, PERC, Selektiver Emitter, Sensitivitätsanalyse, Metamodeling, TLM, Kontaktwiderstand, Emittersättigungstromdichte

Table of Contents

Abstract.....	I
Zusammenfassung.....	III
Table of Contents	V
1. Introduction	1
1.1 Overview of industrial research and development on crystalline silicon solar cells in Germany	1
1.2 Outline of the present work.....	4
1.3 Overview of the applied models and methods	6
2. Metamodeling: A method to understand and model the variation of current-voltage parameters of solar cells.....	11
2.1 Introduction	11
2.2 Application of metamodeling to mc PERC solar cells.....	13
2.2.1 Device model.....	14
2.2.2 Metamodel.....	17
2.2.3 Sensitivity analysis	26
2.3 Application and validation of metamodeling on mc Al-BSF solar cell production	32
2.3.1 Production monitoring.....	33
2.3.2 Metamodeling.....	34
2.3.3 Studentization.....	37
2.3.4 Response surface	38
2.3.5 Validation of the metamodeling strategy	39
2.4 Conclusion	42
3. Methods and models for the front side characterization of solar cells with selective emitters	43
3.1 Front side contact resistance measurements on solar cells with selective emitter	43
3.1.1 Introduction	43
3.1.2 Standard TLM measurement on solar cells.....	44
3.1.3 TLM measurement on solar cells considering intermediate fingers.....	47

3.1.4	TLM measurements on solar cells with selective emitters	49
3.1.5	TLM structure separating homogeneous and selective emitter sheet resistance	53
3.1.6	Conclusion.....	58
3.2	Method for imaging the emitter saturation current density with lateral resolution.....	59
3.2.1	Introduction	59
3.2.2	Experimental method	60
3.2.3	Example of an J_{0e} image derivation	64
3.2.4	Simulation method	66
3.2.5	Sample preparation.....	67
3.2.6	Validation and application of the method	68
3.2.7	Conclusion.....	71
4.	Determination of the rear side contact resistance of screen-printed PERC solar cells	73
4.1	Introduction.....	73
4.2	Sample preparation.....	78
4.3	Modeling	79
4.4	Derivation of the lumped series resistance.....	81
4.5	Evaluation of the rear contact resistance R_C	84
4.5.1	Evaluation of R_C of PERC cells with varying metallization fraction	84
4.5.2	Evaluation of R_C using the TLM method.....	89
4.6	Impact of the rear contact resistance on the solar cell performance	94
4.7	Conclusion	96
5.	References	99
6.	List of publications.....	115
	Danksagung	118
	Lebenslauf.....	120

1. Introduction

1.1 Overview of industrial research and development on crystalline silicon solar cells in Germany

The research and development (R&D) on crystalline silicon solar cells in Germany is currently progressing and introducing new solar cell technologies under difficult economic circumstances. The price of photovoltaic (PV) products has declined strongly, even more than the PV learning curve had suggested [1], which has its roots in global overproduction. Nevertheless, the PV development in the past decade can be seen as a big success for human kind, as ‘clean’ electricity from sunlight has become competitive in comparison with the old energy sources such as coal, gas, oil and uranium [2]. However, there is still a necessity of cost reduction in solar cell fabrication. In microelectronics, ‘process shrinks’ enable considerable reduction in costs. Thus investing in R&D in this industry pays off quickly which cannot be said about PV industry. For solar cell R&D, the main routes to decrease costs are to increase the cell efficiency or to save process steps or to reduce consumables. To increase cell efficiency, new cell concepts are investigated, which are between the poles of efficiency gain and additional process steps involving the increase of costs. Two main strategies are thinkable and applied: evolution and revolution. Nowadays, the main fraction of solar cells is fabricated in the aluminium back surface field (Al-BSF) [3] solar cell design (see Figure 1).

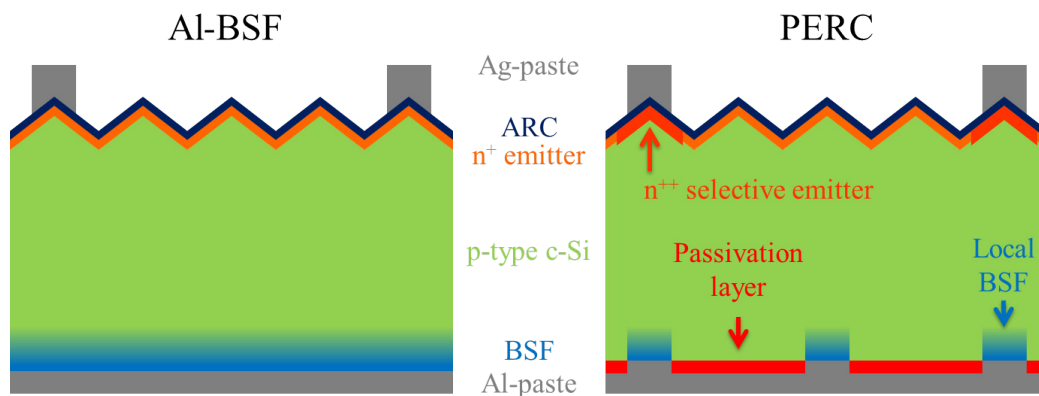


Figure 1: Schematics of the Al-BSF and PERC solar cell design with an anti-reflection coating (ARC).

At present, it allows cell efficiencies for multicrystalline (mc) solar cells of 17 – 18 % and for Czochralski (Cz) of 18.5 – 19.5 %. The evolutionary strategy consists in changing only parts of the Al-BSF solar cell design, going to e.g. the passivated emitter and rear cell (PERC) [4], which mainly changes the rear full area contact to local contacts (see Figure 1). This approach allows one to keep most of the fabrication processes the same and to add only one or two additional process steps. The revolutionary strategy changes the cell concept more radically, requesting more diverse processes for PV industry. Typical examples are the interdigitated back junction back contacted cells (IBC) [5] or the silicon heterojunction (SHJ) [6] solar cell design.

In Germany, efforts towards improved solar cell concepts have been shown by the solar cell manufactures *Hanwa Q Cells*, *Schott Solar*, *Bosch Solar Energy* and *SolarWorld*, and by the equipment suppliers *Centrotherm Photovoltaics* and *Roth & Rau*. New concepts show industrially relevant best efficiencies ranging from 18.9 % to 19.5 % for mc PERC type solar cells and from 19.6 % to 21.3 % for Cz PERC/PERT type solar cells, and for revolutionary concepts (IBC, SHJ) from 21.1 % to 22.1 % (compare Table I).

Even though the PERC concept allows higher efficiencies than the Al-BSF cell, it is still under cost competition, as the additional process steps have to pay off. Nowadays, the solar cell manufactures *Hanwa Q Cells*, *Bosch Solar Energy* and *SolarWorld* fabricate PERC solar cells on a bigger scale and the equipment suppliers *Centrotherm Photovoltaics* and *Roth & Rau* offer and have sold turn-key factories for their PERC and SHJ cell concept, respectively. Whether the higher efficiencies are going to pay off, is still an open question. The Al-BSF cell has been optimized for years now, even though it was not thinkable previously that such high cell efficiency level could be reached. I believe the optimization has not ended yet due to the fact that the mainstream cell concept in production is still that of Al-BSF and the majority of suppliers are likely to focus on its improvement further. The race between Al-BSF and advanced cell concepts is still open. In other words, maybe the question if solar cell fabrication is going to become high- or low-tech has not been answered so far.

Table I: Comparison of reported industrial relevant best crystalline silicon solar cell efficiencies by German solar cell manufactures and equipment suppliers.

Company	Concept	Ref.	Best η [%]	Features	Year
<i>Hanwa Q Cells</i>	PERC	[7]	19.5	mc-Si / p-type / LFC ^b / plating	2011
	PERC	[8]	20.2	Cz-Si / p-type / LFC ^b / plating	2011
	PERT ^a	[9]	20.7	Cz-Si / n-type / BJ ^c / screen-printed	2013
	PERT ^a	[9]	21.3	Cz-Si / n-type / BJ ^c / rear Al PVD ^d	2013
<i>Schott Solar</i>	PERC	[10]	18.9	mc-Si / p-type / LCO ^e / screen-printed	2014
	PERC	[10] [11]	21.0	Cz-Si / p-type / LCO ^e / screen-printed	2012
	PERC	[10]	21.3	Cz-Si / p-type / LCO ^e / plating	2014
<i>Bosch Solar Energy</i>	PERC	[12]	19.6	Cz-Si / p-type / screen-printed	2011
	PERT ^a	[13]	20.7	Cz-Si / n-type / bifacial / screen-printed	2013
	IBC	[14] [15]	22.1	Cz-Si / n-type / ion implantation	2013
<i>SolarWorld</i>	PERC	[16]	20.9	Cz-Si / p-type / screen-printed	2014
<i>Centrotherm</i>	PERC	[17]	19.9	Cz-Si / p-type / LCO ^e / screen-printed	2012
<i>Roth & Rau</i>	SHJ	[18]	21.1	Cz-Si / n-type / a-Si:H / ITO ^f	2013

^a PERT – passivated emitter and rear totally diffused,

^b LFC – laser fired contacts,

^c BJ – back junction,

^d PVD – physical vapor deposition,

^e LCO – local contact openings,

^f ITO – indium tin oxide.

1.2 Outline of the present work

Within this thesis latest topics in solar cell R&D are addressed. The next paragraphs explain their importance and refer to my own original scientific work which has been partly published previously.

The reported record efficiencies (see Table I) do not give a full picture of their industrial applicability. For the introduction of a new solar cell concept into mass production, the understanding and control of variations of the cell efficiency have to be considered or even focused on. The cell efficiency variation is determined by the impact of the variations of the main influencing parameters. In **chapter 2**, a method based on a combination of numerical device simulation and advanced statistical analysis is presented which allows calculating efficiency distributions of solar cell concepts which I exemplify on the PERC concept. The method is successfully validated on the Al-BSF production efficiency distribution of *SolarWorld* in Freiberg. The content of chapter 2 is mainly published in Refs. [19] [20] [21].

For the evolutionary improvement of the Al-BSF solar cell, the front and the rear side recombination and series resistance losses have to be reduced, i.e. within the emitter and the Al-BSF, and the front and rear contact, respectively. Possible optimization routes for the front side are the introduction of selective emitters [17] or etch back emitters [11]. A selective emitter may be described as a two-step emitter, i.e. the emitter is highly-doped underneath the front metal contacts and rather lowly doped in-between (see PERC concept in Figure 1). The idea is to decouple the emitter recombination from the contact formation. The latter is mainly determined by the contact resistance of the front metallization on the emitter. For contact resistance characterization, the transfer length method (TLM) measurement is widely used. In **chapter 3.1**, I show how the TLM may be adjusted to consider a second diffusion beneath the contacts and how a special solar cell TLM test structure allows the separation of the sheet resistances of the first and second diffusions.

Applying two diffusions, the recombination behavior of the emitter in terms of saturation current densities J_{0e} is not laterally homogeneous. State-of-the-art characterization is carried out by the method of Kane and Swanson [22], which only considers a laterally

homogeneous recombination. In **chapter 3.2**, I present an experimental method to overcome this limitation by a combination of photoluminescence (PL) and photoconductance (PC) measurements, which is mainly published in Ref. [23] [24]. Two calibrated lifetime images are derived in high-injection where the method of Kane and Swanson is applied pixel by pixel to derive an emitter saturation current density with lateral resolution.

For the improvement of the rear side, recombination losses have to be reduced. Those arise from the rear contact and the Al-BSF, i.e. defect recombination due to aluminium–oxygen complexes (Al–O complexes) within the Al-BSF [25]. A typical solution is carried out by a passivation of the rear side depositing a dielectric layer which is locally opened and contacted. Typical industrial relevant dielectric layers are stacks from $\text{AlO}_x/\text{SiN}_y$ [10] or $\text{SiO}_x/\text{SiN}_y$ [17] which contain high fixed surface charges as the main passivation mechanism. Surface recombination velocities below 10 cm/s are reported. The local contacts are fabricated by laser fired contacts (LFC) or laser contact openings (LCO), i.e. local rear contacts are fabricated by laser processing and Al sheet layer screen-printing producing a cheap rear side metallization. The main contact properties are the contact recombination and the contact resistance. Investigations about the contact recombination of LFC may be found in Refs. [26] [27]. For LCO contacts, investigations are carried out in Refs. [28] [29]. One route to reduce contact recombination is to lower the contact fraction. Thus the contact resistance becomes more and more important and may limit the efficiency potential of PERC solar cells. In **chapter 4**, current methods to derive the contact resistance of local rear contacts are evaluated and improved using the example of LCO contacts, which is mainly published in Ref. [30]. These improved evaluations of the rear contact resistance of PERC solar cells containing industrial rear side Al pastes lead to lower resistance values than previously reported and to a reduced uncertainty. The rear contact resistance proves not to be a substantial loss mechanism.

1.3 Overview of the applied models and methods

In this chapter, I will give a summary about the models and methods, which are applied and further developed within this thesis. The necessary prior knowledge may be deduced from that, which is found in Refs. [31] [32] [33] [34] [35] [36].

For solar cell modeling and experiment evaluation the basic semiconductor equations are Poisson equation, continuity equations and current density equations. The Poisson equation describes the relationship between the electrostatic potential ψ and the charge distribution,

$$\nabla \cdot (\varepsilon \nabla \psi) = -q(p - n + N_{don}^+ - N_{acc}^-) \quad , \quad (1)$$

where ε is the permittivity of the material, q is the elementary charge, p is the hole carrier density, n is the electron carrier density, N_{don}^+ is the ionized donor concentration and N_{acc}^- is the ionized acceptor concentration. The continuity equations, which conserve the quantity charge carrier, are for electrons

$$\frac{\partial n}{\partial t} = \frac{1}{q} \nabla \cdot \vec{J}_n + G - R \quad , \quad (2)$$

and for holes,

$$\frac{\partial p}{\partial t} = -\frac{1}{q} \nabla \cdot \vec{J}_p + G - R \quad , \quad (3)$$

where G is the optical generation rate of charge carriers, R is the recombination rate of charge carriers, J_n and J_p are the electron and hole current densities, respectively. These are defined by the current density equations in the drift-diffusion approach. The gradient in electrostatic potential and the concentration gradient of charge carriers are the driving forces for the current densities of electrons and holes, respectively,

$$\vec{J}_n = -q\mu_n n \nabla \psi + qD_n \nabla n \quad , \quad (4)$$

$$\vec{J}_p = -q\mu_p p \nabla \psi - qD_p \nabla p \quad , \quad (5)$$

where μ_n and μ_p are the mobilities, and D_n and D_p are the diffusion coefficients for electrons and holes, respectively. The mobilities and diffusion constants are related through the Einstein relationships $D_n = \frac{k_B T}{q} \mu_n$ and $D_p = \frac{k_B T}{q} \mu_p$ for a non-degenerated semiconductor, where k_B is the Boltzmann constant and T is the temperature. For a degenerated semiconductor (e.g. doping densities higher than $1 \times 10^{19} \text{ cm}^{-3}$), Fermi-Dirac statistics is valid and the electron transport equation is extended by the additional term $-nk_B T \nabla \left(\ln \left(\frac{n}{N_C} e^{(E_C - E_{F,n})/(k_B T)} \right) \right)$ and the hole transport equation by $-pk_B T \nabla \left(\ln \left(\frac{p}{N_V} e^{(E_{F,p} - E_V)/(k_B T)} \right) \right)$, respectively. N_C and N_V are the effective density of states for electrons in the conduction band and for holes in the valence band, respectively. $E_{F,n}$ and $E_{F,p}$ are the quasi-Fermi levels for electrons and holes, respectively. A doping and carrier concentration dependent, temperature dependent mobility model may be found in Refs. [37] [38].

Eqs. (1),(2),(3),(4) and (5) build a coupled set of differential equations, which may be solved by an iterative procedure to numerically simulate crystalline solar cells, e.g. with TCAD Sentaurus Device [39]. The advantage of numerical simulations compared to analytical solutions is in the increased accuracy. Analytical solutions are restricted to particular assumptions such as constant photogeneration, constant doping or low injection conditions, which often only approximate real device behavior.

State-of-the-art physical models for the simulation and experiment evaluation are summarized and referred to below. For highly-doped semiconductors, the band gap decreases, i.e. the energy between valence and conduction band, which is called band gap narrowing (BGN). It occurs due to carrier-dopant and carrier-carrier interactions. The used

BGN model for silicon is derived in Ref. [40]. Under illumination of a solar cell, the optical generation of electron-hole pairs is present in the silicon, which is due to absorption. Surface geometries, the optical properties of antireflection coating layers and passivation layers determine mainly the generation rate within the silicon. A carrier photogeneration profile is often derived by geometrical ray tracing with e.g. SUNRAYS [41]. For a high absorption, comparably thick wafers or good light trapping are necessary for the indirect semiconductor silicon, i.e. for wavelengths close to the band edge, a phonon-assisted absorption is dominant. The reversal process of generation is recombination, where created, excess charge carriers are decayed back to their equilibrium densities. If the illumination is stopped suddenly, the excess charge carriers vanish after a ‘mean’ time, called lifetime τ . It is determined by three main recombination processes: the radiative recombination [42] [43], the Auger recombination [44] and the Shockley-Read-Hall (SRH) recombination [33], and at surfaces by surface recombination [33]. The different recombination processes take place in parallel to each other in a semiconductor and the concept of effective lifetime accounts for all of them [32].

In this work, statistical methods are used for the understanding and modeling of variations in solar cell fabrication. An applied introduction to statistical methods is found in Ref. [34]. In solar cell fabrication, influencing process parameters, such as chemical concentrations, gas flows or peak firing temperatures, as well as response parameters, such as the cell efficiency, are distributed. A distribution of a parameter of interest is described by its statistical parameters, such as median, percentiles, lower and upper quartile (25th and 75th percentile), and interquartile range (IQR). A commonly occurring distribution is the Gaussian or normal distribution, shown in Figure 2, which is fully described by the parameters mean μ and standard deviation σ . In a normal distribution, the mean corresponds to the median, $\pm\sigma$ are the about 16th and 84th percentile, i.e. $\pm\sigma$ is within a 68-percentile range around the median, and $\pm 2\sigma$ are about the 2nd and 98th percentile. For an experimental distribution $Y_1 \dots Y_n$, i.e. finite sample size n and unknown standard deviation σ , only the estimate of the mean \bar{Y} and the estimate of the standard deviation s_y can be derived. Distributions are typically plotted as histograms, but more relevant representations are normal probability plots, where the data are plotted against a theoretical normal distribution for comparison.

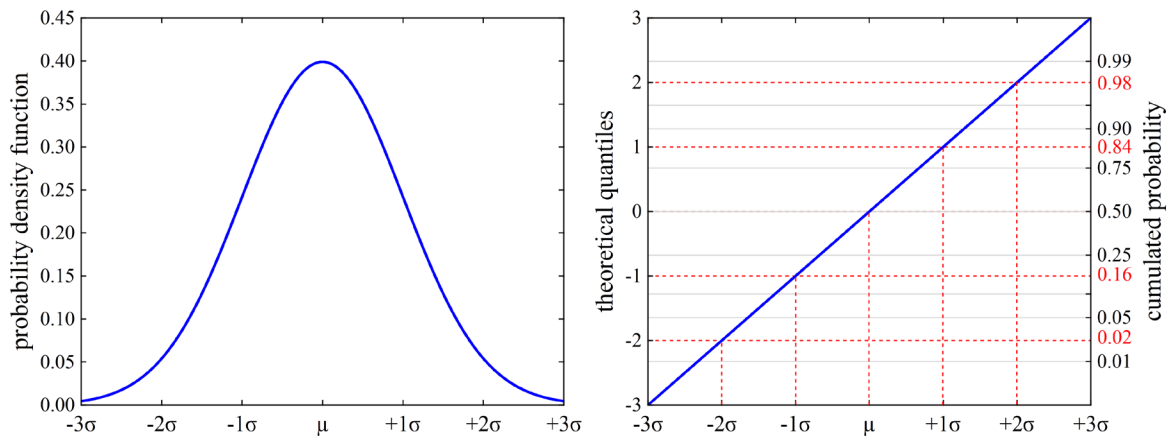


Figure 2: Histogram (left) and normal probability plot (right) of a normal distribution with the mean μ and the standard deviation σ .

In experimental work, the Design of Experiment (DoE) [45] is commonly applied to identify the main influencing parameters, their strength, and to enable their optimization. The DoE is evaluated by the response surface methodology (RSM). DoE and RSM are applied in this thesis on computer experiments to build up polynomial expressions, called metamodels [35]. Thus the number of simulations, i.e. computing time, is drastically reduced and a model is derived, which simply explains, predicts and manipulates distributions in mass production, of e.g. the solar cell efficiency. But the accuracy of numerical simulation is maintained. The metamodel is usable to generate distributions through varying influencing parameters by the Monte Carlo method [46].

A variety of experimental methods are applied and extended within the thesis, which are state-of-the-art characterization techniques for crystalline silicon solar cells. Lifetime measurements are performed using the photoconductance decay (PCD) method with a Sinton Instruments measurement device [47] as it is very robust and has low measurement uncertainty [48] [49]. Unfortunately, the spatial resolution is limited to the area of the inductive-coil detector. To overcome resolution issues, photoluminescence measurements are applied for the characterization of e.g. multicrystalline wafers. The synergy of both methods, i.e. of a photoconductance (PC) calibrated photoluminescence image, allows the derivation of lifetime images with a much higher lateral resolution.

For the electrical characterization, current-voltage curve (I-V-curve) measurements in the dark and under illumination are carried out. From the latter, the short-circuit current density J_{SC} , the open-circuit voltage V_{OC} , the current density at maximum power point (MPP) J_{MPP} , the voltage at maximum power point (MPP) V_{MPP} are derived. The MPP determines the fill factor $FF = \frac{J_{MPP}V_{MPP}}{J_{SC}V_{OC}} = \frac{P_{MPP}}{J_{SC}V_{OC}}$ and the efficiency $\eta = \frac{P_{MPP}}{EA}$, where E is the irradiance and A is the area of the solar cell. During solar cell operation, power losses arise partly due to series resistance. The series resistance of a solar cell lumps busbar, finger, front contact, emitter, base, rear contact, rear metallization resistance. A variety of methods for the lumped series resistance determination exist [50]. Within this thesis, the resistance extraction from two or more illuminated I-V-curves is preferred as the current flow pattern within a solar cell remains similar and injection-dependent effects are reduced. For a lateral resolution of the series resistance, again a PL technique is applied [51], which bases on two different illumination levels. The derivation of the lumped series resistance with lateral resolution allows the evaluation of the resistance homogeneity, e.g. the identification of increased contact resistance due to firing issues. For the measurement of contact resistances the transfer length method [52] (TLM) is applied, which can be seen as a standard for contact resistance measurements.

2. Metamodeling: A method to understand and model the variation of current-voltage parameters of solar cells

2.1 Introduction

The key to the success of a cell concept in production is not only the realized cell efficiency level, but also the efficiency distribution (see Figure 3). Its understanding and control demand a detailed comprehension of the *variation* of the process and the cell parameters. In this chapter, I show how the cell efficiency variation can be understood, predicted and reduced by changes to specific process steps.

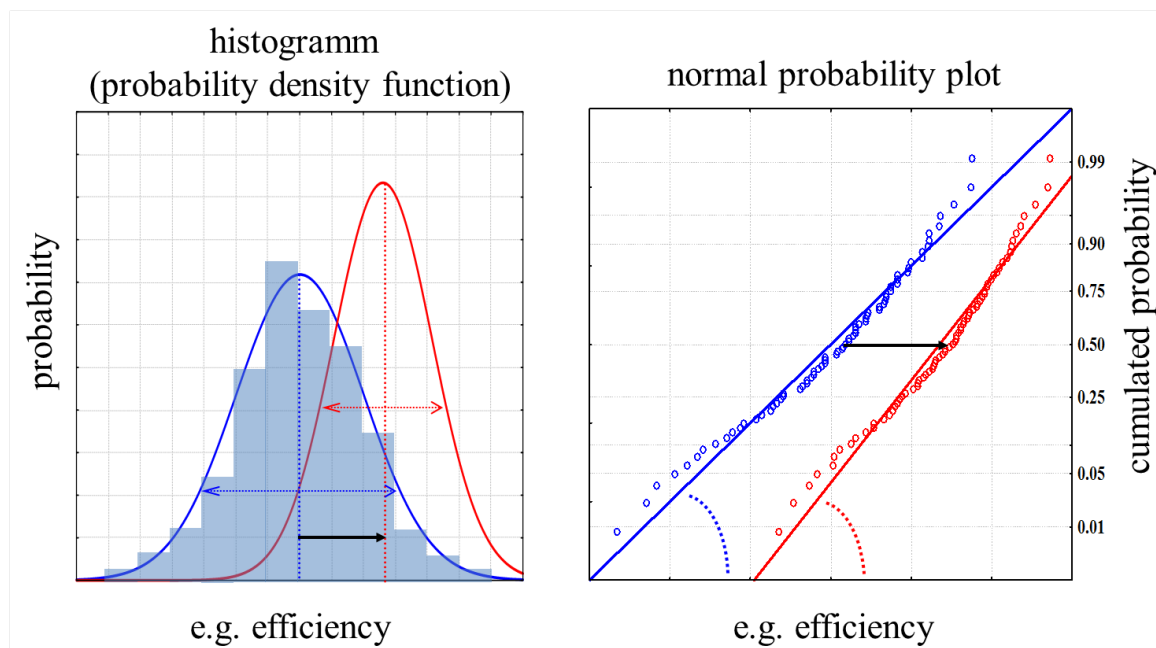


Figure 3: Sketch of two efficiency distributions: the initial distribution (blue) is improved by maximization and reduction of its variation (red). The left graph shows the histogram while the right graph represents the normal probability plot of the same distributions.

The variation is modeled with a combination of numerical device simulation and advanced statistical analysis borrowed from the microelectronics industry [19]. Only a small number of numerical device simulations is necessary because a Design of Experiment (DoE) is set up, where all input parameters are varied concurrently. The simulation results are then

fitted with polynomial expressions using the so-called response surface methodology (RSM). The resulting model is again continuous and is called a metamodel [35]. The derived metamodel is used to model the cell parameter variation using, e.g. normally, distributed input parameters (see Figure 4 for a flow chart).

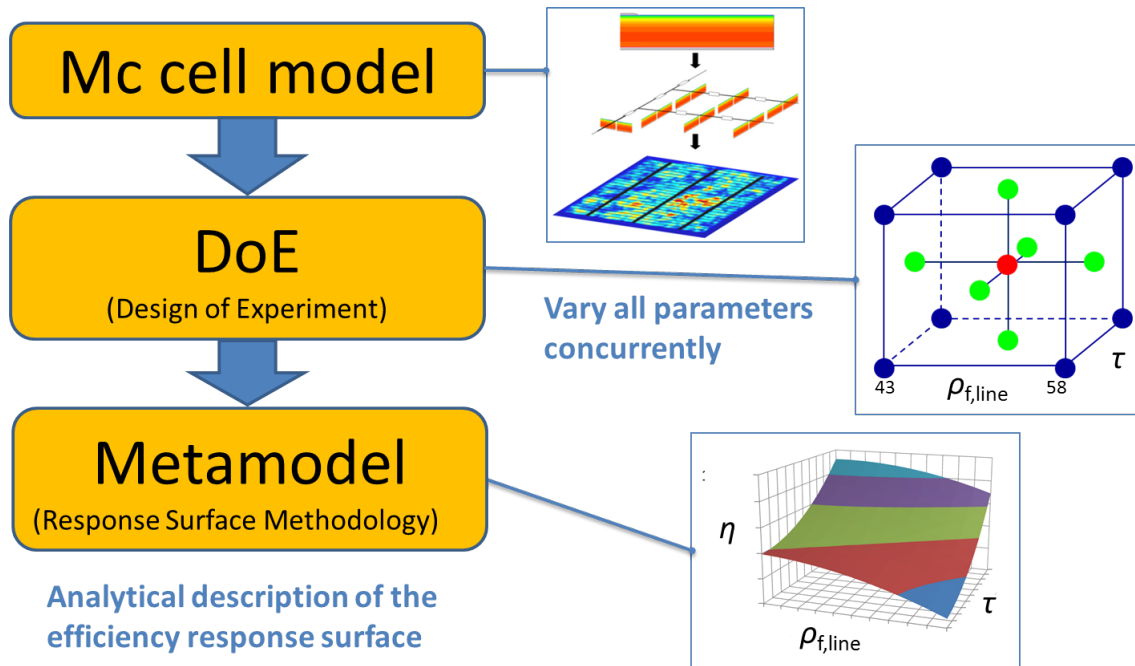


Figure 4: The three main steps of the metamodelling strategy: (i) setting up e.g. a multicrystalline (mc) cell model, (ii) incorporating the variation by a Design of Experiment (DoE) approach, and (iii) evaluating the DoE by the response surface methodology (RSM), resulting in the metamodel.

The strategy allows for the evaluation of process variations, for the prediction of optimal process parameters, and for a sensitivity analysis to quantify and minimize the impact of process fluctuations on cell efficiency, i.e. production yield.

On the one hand, a high accuracy level is achieved by using numerical device simulations, on the other hand the derived metamodel is simple and well suited for performing a global optimization, a sensitivity analysis of the influencing factors, and enables one to predict the expected distribution of cell parameters in production. An optimal starting point for experimental development work may be derived as well.

The metamodeling strategy will first be explained on the example of multicrystalline PERC solar cells and then be applied to multicrystalline Al-BSF solar cells for validation.

2.2 Application of metamodeling to mc PERC solar cells

In the following chapter, the variation of important influencing factors is simulated, which characterize process variations. In a PERC – passivated emitter and rear cell [4] – these factors include wafer resistivity, wafer SRH lifetime, rear contact distance, rear surface recombination velocity, damage of the local rear contacts, and the rear contact resistivity. Varying each of these six parameters, e.g. in 5 steps, would necessitate $5^6 = 15625$ simulations for all combinations, which would take an impracticably long computing time. Therefore a Design of Experiment (DoE) approach is used, whereby all input parameters are varied concurrently in a Central Composite Inscribed Design as exemplified in Figure 5 for three dimensions [34]. This DoE design reduces the number of simulations in the above example to 77.

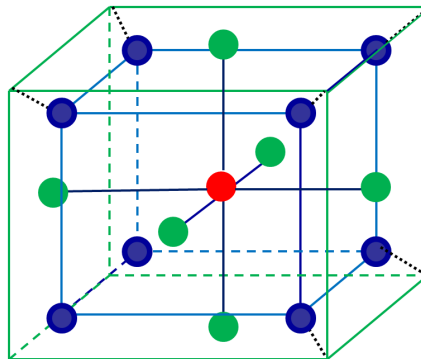


Figure 5: Schematic of a Central Composite Inscribed Design of Experiment (DoE) for three influencing factors, which are varied along their respective axes. Axial points are marked in green, cube points in blue, and the center point in red.

The 77 simulation results are then fitted with polynomial expressions in a regression analysis, using the so-called response surface methodology (RSM) [34]. The resulting model is again continuous and is called a *metamodel* [35]. While it is an approximation of

the Input/Output (I/O) function [35], it is important to note that it contains all the *mutual* interactions of the influencing factors, although only a minimal number of simulations are carried out.

It is shown below that this evaluation scheme is a viable alternative to the state-of-the-art analytical models of PERC cells, such as Pitchmaster [53], GridSim [54], and the methods published in Refs. [55] [56] [57] [58], as well as to simplified numerical device models [59] [60]. On the one hand, a high accuracy level is achieved by using numerical device simulations, on the other hand the derived metamodel is simple and well suited for performing a global optimization, a sensitivity analysis of the influencing factors, and it enables one to predict the expected distribution of cell parameters in production. An optimal starting point for experimental development work is also presented.

2.2.1 Device model

For the numerical solution of the semiconductor differential equations in the drift-diffusion approach, the software TCAD Sentaurus Device [39] and state-of-the-art physical models [36] [61] [62] are used. The photogeneration profile is obtained with the ray-tracing software Sunrays [41], and the front metallization is included using LTspice [63].

The geometrically irreducible *standard domain* for the device simulation is shown in Figure 6. The standard domain is as high as the cell thickness and its width and length is chosen to be half of the rear local contact distance, called index d_i . At first sight, this may contradict the emitter geometry, because the front metal finger distance is generally unequal to the index (half pitch). However, the front surface is chosen to be fully covered with a metal contact, and the contact recombination velocity is adjusted to be so low that the measured [22] emitter saturation current J_{0e} is reproduced in the model [64] (by using a measured doping profile). In this way, the index can be freely varied, irrespective of the front finger distance.

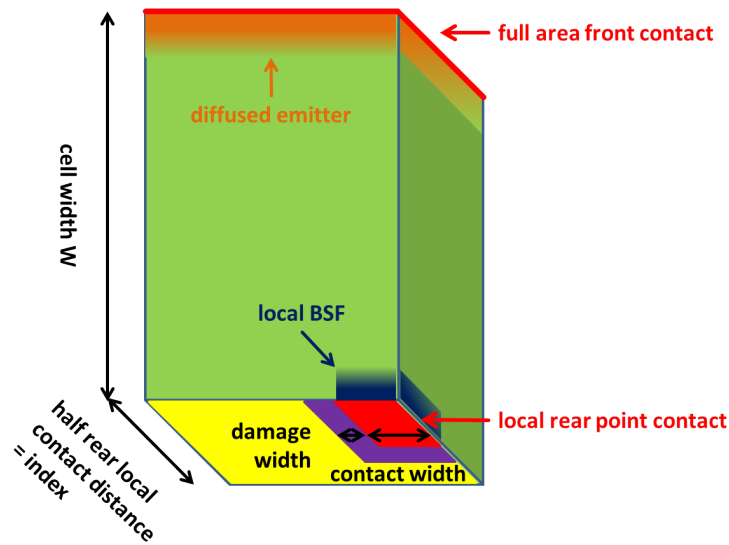


Figure 6: Irreducible standard domain for numerically modeling a rear locally contacted solar cell. Note that the index is half of the rear local contact distance (half pitch).

This choice of the standard domain causes a homogeneous electron current flow across the p-n junction into the front metal, and therefore neglects the resistive losses in the emitter arising, in reality, due to lateral currents flowing towards the front contact fingers. These resistive losses will be included later, in the simulation results in Section 2.2.2 B, with an analytical equation. In the model, the front contact is fully transparent to the incoming light. The shading caused by the front metal fingers is even neglected to keep the DoE simple, and add shading afterwards in the response model. Note that the resistive losses associated with the rear local contacts, including spreading resistance in the bulk, are fully and correctly taken into account in the simulation domain. The device parameters of the central point of the DoE, shown in Figure 5, are listed in Table II.

The Shockley-Read-Hall (SRH) recombination in the bulk is included with a single defect energy at midgap having equal SRH lifetime parameters for electrons and holes, $\tau = \tau_p = \tau_n$. The SRH surface recombination at the passivating dielectric layer at the rear is also included, again with a single defect energy at midgap and equal surface recombination parameters for electrons and holes, $S_{\text{rear}} = S_{n,\text{rear}} = S_{p,\text{rear}}$.

Table II: Geometric, electrical and electronic domain parameters for the central point (shown in Figure 5 as a red dot).

Parameter	Symbol	Value	Unit
Cell thickness	W	160	μm
Index	d_i	325	μm
Rear contact width		22	μm
Rear damage width		11	μm
Front contact resistivity	$\rho_{c,\text{front}}$	2×10^{-3}	Ωcm^2
Rear contact resistivity	ρ_c	2×10^{-3}	Ωcm^2
Wafer resistivity	ρ_w	1.5	Ωcm
Wafer boron doping density	N_A	9.74×10^{15}	cm^{-3}
Measured emitter doping profile:			
Peak doping density	$c(\text{P})_{\text{Peak}}$	2.4×10^{20}	cm^{-3}
Junction depth		0.5	μm
Gaussian BSF doping profile:			
Peak doping density	$c(\text{Al})_{\text{Peak}}$	5×10^{18}	cm^{-3}
Junction depth		0.3	μm
Lateral depth		0.3	μm
SRH recombination parameters:			
Bulk electron	τ_n	90×10^{-6}	s
Bulk hole	τ_p	90×10^{-6}	s
Surface electron	$S_{n,\text{rear}}$	105	cm/s
Surface hole	$S_{p,\text{rear}}$	105	cm/s
Damaged surface electron	$S_{n,\text{dam}}$	1000	cm/s
Damaged surface hole	$S_{p,\text{dam}}$	1000	cm/s
Front surface hole	$S_{p,\text{front}}$	845596	cm/s

To minimize the number of mesh points, the rear contact is given a quadratic shape. Comparisons with a circular shape do not show relevant deviations. The rear contact has, in reality, a very weak back surface field (BSF), which is included in the model via a Gaussian doping profile, as given in Table II. In industrial applications, the local rear contacts may be surrounded by a damaged dielectric layer, as indicated in Figure 6, causing an increased surface recombination velocity $S_{\text{dam}} = S_{n,\text{dam}} = S_{p,\text{dam}}$, compared to S_{rear} . These losses may also represent additional losses, e.g. arising from distorted BSFs, laser damage, etc.

2.2.2 Metamodel

A. Variation of parameters in the device model

To incorporate the influence of variations into the device model, the six input parameters (influencing factors) are varied in a systematic, Central Composite Inscribed (CCI) Design of Experiments (DoE), as exemplified in Figure 3 for three dimensions. The Central Composite design is appropriate for a second-order (quadratic) response model, and involves 5 different values (levels) for each input parameter, whereas the axial points are orthogonally scaled.

These parameter variations are obtained using the software JMP [65] and are listed in Table III. They cover a typical range for this multicrystalline PERC cell structure: SRH lifetime τ as reported in [66], rear surface recombination velocity S_{rear} as in [67] [68], damaged surface recombination velocity S_{dam} as in [26], and rear contact resistivity ρ_c as in [69]. Most parameters are varied in a linear scale, but S_{dam} is varied logarithmically, because it spans some orders of magnitude.

Table III: The values of each input parameter at the dots in Figure 5, obtained from the Central Composite Inscribed DoE.

Number	d_i [μm]	ρ_w [Ωcm]	τ [s]	S_{rear} [cm/s]	S_{dam} [cm/s]	ρ_c [Ωcm^2]
Lower axial points	150	0.50	30×10^{-6}	10.00	1.0×10^1	1.0×10^{-5}
Lower cube points	226	0.93	56×10^{-6}	51.04	7.3×10^1	8.7×10^{-4}
Center point	325	1.50	90×10^{-6}	105.00	1.0×10^3	2.0×10^{-3}
Upper cube points	424	2.07	120×10^{-6}	158.96	1.4×10^4	3.1×10^{-3}
Upper axial points	500	2.50	150×10^{-6}	200.00	1.0×10^5	4.0×10^{-3}

B. Evaluation of the DoE – response surface methodology (RSM)

The results of the 77 device simulations are analyzed with the response surface methodology (RSM) [45]. The derived metamodel is based on the following second-degree polynomial functions with linear, quadratic and two-factor interaction terms:

$$E(x) = \beta_0 + \sum_{i=1}^k \beta_i x_i + \sum_{i=1}^k \sum_{j \geq 1}^k \beta_{ij} x_i x_j \quad (6)$$

The influencing factors x are the index d_i , the wafer resistivity ρ_w , SRH lifetime τ , rear surface recombination velocity S_{rear} , damaged surface recombination velocity S_{dam} and the rear contact resistivity ρ_c , while the responses E are the cell efficiency η , the fill factor FF , the short-circuit current density J_{SC} and the open-circuit voltage V_{OC} . A least-square fit is carried out using JMP [65] to determine the coefficients β . The significance of each term of the polynomial function is tested as a predictor for cell parameters by means of a multivariate regression analysis, applying a rather strict significance level of less than 0.01 as the criterion for inclusion. The normal probability assumption is tested for the residuals, which ensures that the model is consistent. Finally, only the model with the highest coefficient of determination (adjusted R-squared) is chosen. The resulting coefficients with corresponding standard errors of the polynomial functions are provided in Table IV.

Table IV: Coefficients of the polynomial function, Eq. (6). Missing coefficients indicate non-significant terms in the metamodel for η , FF , J_{SC} and V_{OC} , respectively.

Term β	Coefficient η	Std Error η	Coefficient FF	Std Error FF	Coefficient J_{SC}	Std Error J_{SC}	Coefficient V_{OC}	Std Error V_{OC}
Constant	$2.11 \times 10^{+01}$	2.2×10^{-01}	8.33×10^{-01}	1.1×10^{-03}	$3.99 \times 10^{+01}$	1.1×10^{-01}	6.33×10^{-01}	4.9×10^{-03}
d_i	2.01×10^{-03}	9.5×10^{-04}	7.66×10^{-05}	5.8×10^{-06}	-4.72×10^{-04}	5.0×10^{-04}	1.18×10^{-05}	2.1×10^{-05}
ρ_w	-4.05×10^{-01}	4.5×10^{-02}	-2.59×10^{-03}	3.4×10^{-04}	3.01×10^{-01}	6.9×10^{-02}	-9.75×10^{-03}	1.1×10^{-03}
τ	2.78×10^{-02}	2.2×10^{-03}	9.72×10^{-06}	4.4×10^{-06}	1.36×10^{-02}	1.2×10^{-03}	5.34×10^{-04}	5.2×10^{-05}
S_{rear}	-2.91×10^{-03}	5.3×10^{-04}	-6.24×10^{-06}	7.8×10^{-07}	-1.56×10^{-03}	7.2×10^{-05}	-5.98×10^{-05}	1.2×10^{-05}
S_{dam}	4.26×10^{-03}	7.1×10^{-02}	-2.38×10^{-03}	1.7×10^{-04}	-4.53×10^{-02}	3.6×10^{-02}	4.75×10^{-03}	1.6×10^{-03}
$\log(\rho_c)$	7.28×10^{-02}	2.3×10^{-02}	2.77×10^{-03}	1.3×10^{-04}				
d_i^2	-7.65×10^{-06}	1.4×10^{-06}	-1.37×10^{-07}	8.2×10^{-09}	-2.31×10^{-06}	7.5×10^{-07}	-8.42×10^{-08}	3.1×10^{-08}
$d_i \times \rho_w$	-6.58×10^{-04}	1.3×10^{-04}	-3.13×10^{-05}	7.8×10^{-07}				
$d_i \times \tau$			3.64×10^{-08}	1.3×10^{-08}				
$d_i \times S_{dam}$	1.36×10^{-03}	6.6×10^{-05}	4.06×10^{-06}	3.9×10^{-07}	9.75×10^{-04}	3.6×10^{-05}	2.20×10^{-05}	1.5×10^{-06}
$d_i \times \log(\rho_c)$	-5.00×10^{-04}	6.6×10^{-05}	-1.92×10^{-05}	3.9×10^{-07}				
ρ_w^2					-7.33×10^{-02}	2.3×10^{-02}		
$\rho_w \times \tau$							2.78×10^{-05}	8.7×10^{-06}
$\rho_w \times S_{dam}$				9.5×10^{-04}	6.86×10^{-05}		-1.68×10^{-03}	2.6×10^{-04}
τ^2	-9.53×10^{-05}	1.2×10^{-05}			-5.73×10^{-05}	6.4×10^{-06}	-1.87×10^{-06}	2.6×10^{-07}
$S_{rear} \times \tau$	-1.12×10^{-05}	4.1×10^{-06}					-2.64×10^{-07}	9.1×10^{-08}
$S_{dam} \times \tau$	-1.00×10^{-03}	1.9×10^{-04}					-2.77×10^{-05}	4.3×10^{-06}
$S_{dam} \times S_{rear}$	4.58×10^{-04}	1.2×10^{-04}					1.20×10^{-05}	2.7×10^{-06}
S_{dam}^2	-1.09×10^{-01}	1.1×10^{-02}			-7.30×10^{-02}	5.7×10^{-03}	-2.24×10^{-03}	2.4×10^{-04}

The adjusted response graph in Figure 7 shows the 24 correlations between the influencing factors x and the cell parameters E as red lines. Each curve is obtained by setting all the other factors to their central value. The blue symbols mark the 77 numerical device simulations. These are adjusted to the central value of the other factors using the parameter difference in the metamodel. The deviations show the residues of the simulated data points to the metamodel.

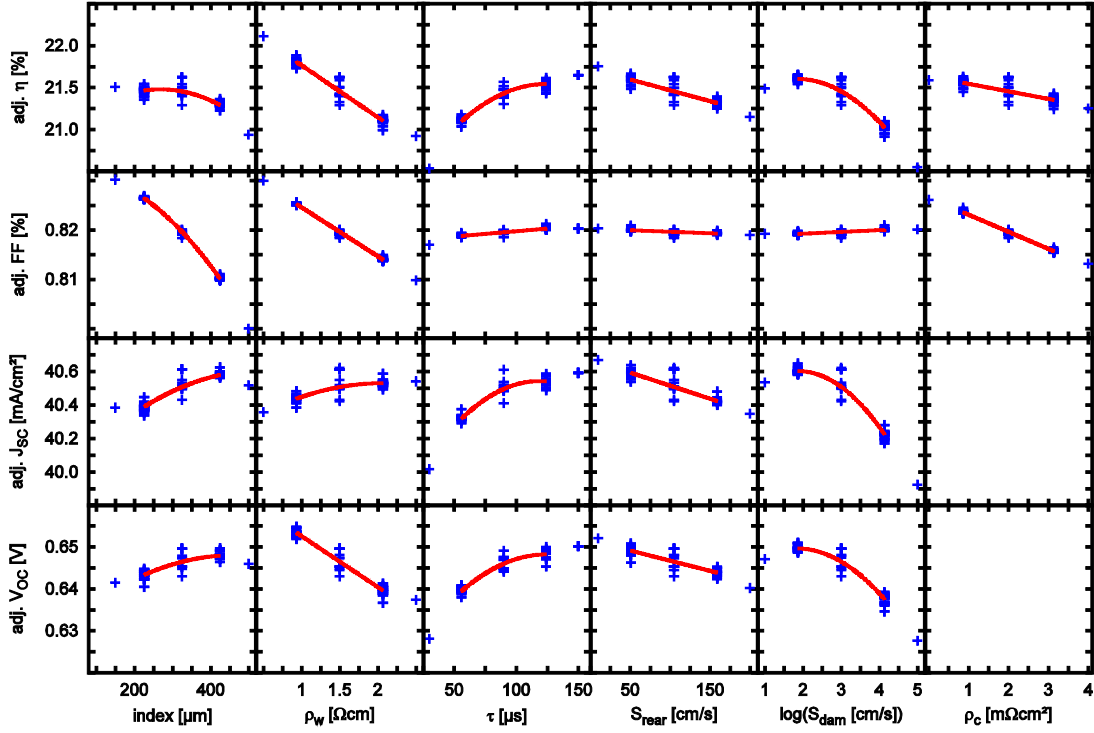


Figure 7: Adjusted response graph for the correlations between the influencing factors and the cell parameters. The metamodel is given as curves, and the crosses mark the 77 numerical simulations projected on the graphs. All curves and crosses are adjusted by setting all of the other factors to their central point according to Figure 5. The influencing factors are the index d_i (half the distance between the local rear contacts = half pitch), the wafer resistivity ρ_w , the wafer SRH lifetime τ , the rear metal contact resistivity ρ_c , the recombination velocity at the rear dielectric layer S_{rear} , and near the rear metal contacts S_{dam} .

Curves that fail the above-mentioned significance test are omitted (meaning that the contact resistivity does not significantly influence J_{SC} or V_{OC}). Note that each subgraph is a cross-section of a six-dimensional response surface which depends on all factors. The software JMP therefore provides an adjustable graph, whereby the user can freely adjust the input parameters; changing one input parameter then changes all 24 subgraphs at the same time. The correlations in Figure 7 are qualitatively as expected: for example, V_{OC} and J_{SC} both increase with increasing d_i and τ , while V_{OC} and J_{SC} react in opposite trends to the wafer resistivity ρ_w , S_{rear} and S_{dam} . FF depends strongly on d_i , ρ_c , and ρ_w . Consequently, the cell efficiency η does indeed depend on all six factors.

Figure 8 reveals the dynamics of cell efficiency in more detail. For each curve, the parameter labeled in the text panel of the same row is adjusted to its central, minimum and maximum value of variation (see Figure 5), respectively, while all other factors are set to their central point, as in Figure 7. If the three curves are non-parallel, an interaction term β_{ij} is important, as for example in the case of the index and the damaged dielectric layer S_{dam} (the subgraph in the first column, second-lowest row). Apparently, the optimal index depends strongly on S_{dam} .

The main advantage of the metamodel is the availability of a tool for finding a global maximum of cell efficiency and for conducting a sensitivity analysis with a very small numerical effort.

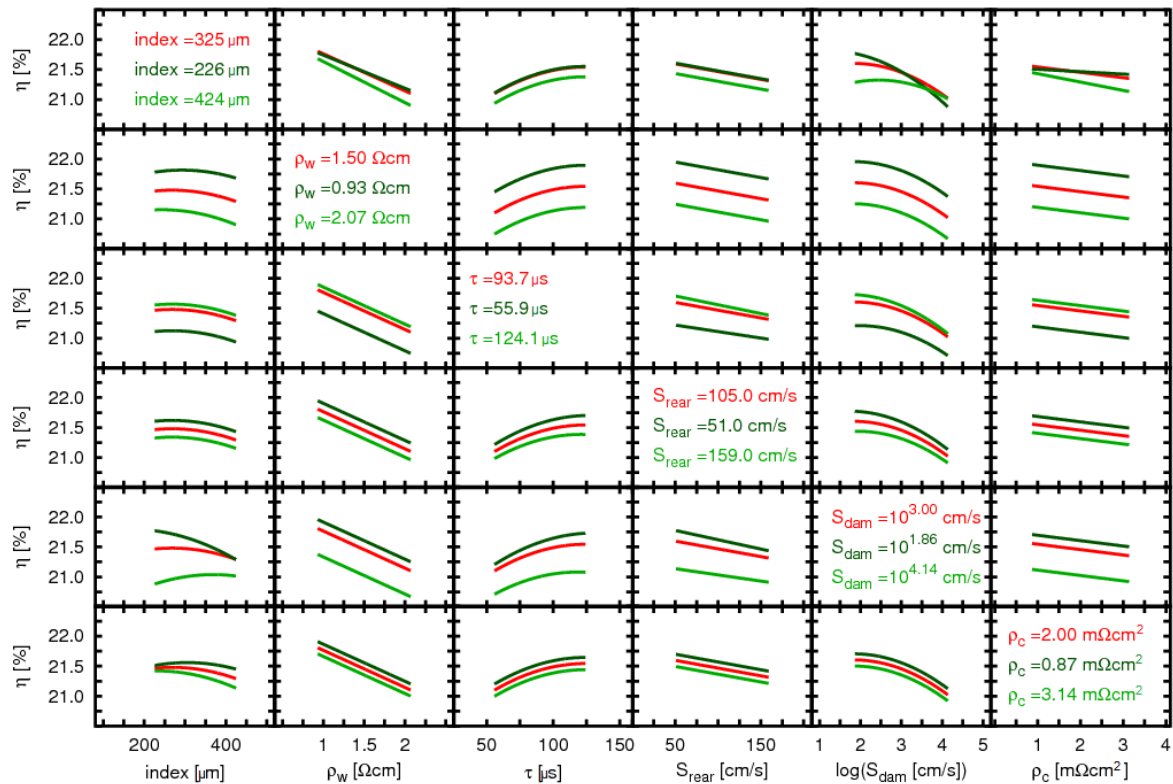


Figure 8: Interaction graphs for cell efficiency η . In each line, the influence of one factor on η is shown for the center, the lower cubic and the upper cubic point of another factor, which is given in the text panel in the same row. A strong interaction between the index and the laser damage (S_{dam}) can be seen in the subgraph in the first column, second-lowest row.

C. Additional linear terms for shading and series resistance

As noted in Section 2.2.1, not all dependencies are included in the device model, to keep it simple. In the following, it is shown that it is easier to include more dependencies as additional terms in the metamodel without a substantial loss of precision. For example, the shading of the front metallization is neglected. Now, J_{sc} is scaled by multiplying it with $(1 - f_{sh}A_{met}/A_{cell})$, where A_{cell} is the cell area, A_{met} the front metallization area, and f_{sh} is the optical shading factor, which in the case of screen-printing is 0.42 in the module [70]. The shading factor takes into account that a fraction of light impinging on the metal is deflected or scattered, and therefore contributes to J_{sc} . Because A_{met} is in the range between 5–10%, I do not need to re-evaluate the maximum power point, but can multiply η by the same factor and assume that FF and V_{OC} remain unaffected. A comparison with some test simulations shows that V_{OC} does not change significantly with varying metal finger width for typical industrial screen-printed fingers.

Another type of loss, which is not included in the device model in Section 2.2.1, is the resistive losses due to lateral electron flow in the emitter. These losses can be computed with a spice model, similar to Ref. [71], which also comprises the resistive losses due to the currents in the front metal fingers. In this case, the lumped resistance turns out to be $\Delta R = 0.6 \Omega\text{cm}^2$. The relative reduction of the FF and η is calculated by

$$E_{New}(x, \Delta R) = \left(1 + \Delta R \frac{J_{MPP}}{V_{MPP}} \right) E(x) \quad , \quad (7)$$

where the mean current density at maximum power point (MPP) is $J_{MPP} = -38.55 \text{ mA/cm}^2$ and the mean voltage at MPP is $V_{MPP} = 551.9 \text{ mV}$. This simple procedure is appropriate only if ΔR is small. Otherwise, all simulated I-V-curves would need to be corrected by replacing V with $V - \Delta R \times J$. The application of the correction procedure for $A_{sh} = 10\%$ and $\Delta R = 0.6 \Omega\text{cm}^2$ is shown in Figure 9.

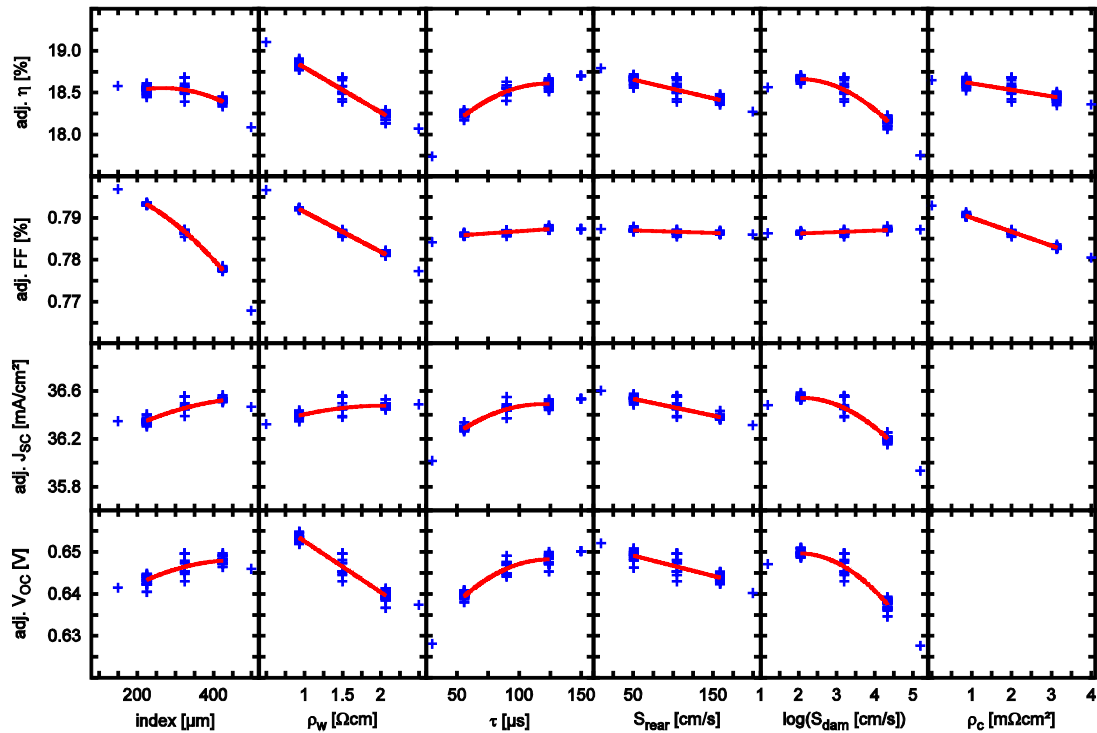


Figure 9: Adjusted response graph of the linearly shading and series resistance corrected metamodel for the correlations between the influencing factors and the cell parameters. The metamodel is given as curves, and the crosses mark the 77 numerical simulations projected on the graphs. All curves and crosses are adjusted by setting all of the other factors to their central point according to Figure 5. The influencing factors are the index d_i (half the distance between the local rear contacts = half pitch), the wafer resistivity ρ_w , the wafer SRH lifetime τ , the rear metal contact resistivity ρ_c , the recombination velocity at the rear dielectric layer S_{rear} , and near the rear metal contacts S_{dam} .

D. Additional non-linear terms

In the device model, the wafer SRH lifetime τ and the wafer resistivity ρ_w are treated as independent input parameters. This is valid for a multicrystalline solar cell, since all combinations of τ and ρ_w are observed (τ is mainly influenced by factors such as dislocation density and impurity concentrations). However, in Czochralski-grown material, it may be necessary to optimize the base resistivity ρ_w by taking into account the impact of

the boron–oxygen recombination center. In its fully degraded state, τ is described as follows [72] [73] [74]:

$$\tau(N_A, O_i) = 4.02024 \times 10^{45} (N_A)^{-0.824} [O_i]^{-1.748} m \quad , \quad (8)$$

where a common interstitial oxygen concentration $[O_i] = 7.5 \times 10^{17} \text{ cm}^{-3}$ is chosen, a common improvement factor $m = 3.0$ (considering that the thermal budget dissociated many O_i -dimers), and the dopant-resistivity relationship taken from Thurber [75]. Note that this term is not linear, and that it influences the response surfaces, as shown in Figure 10.

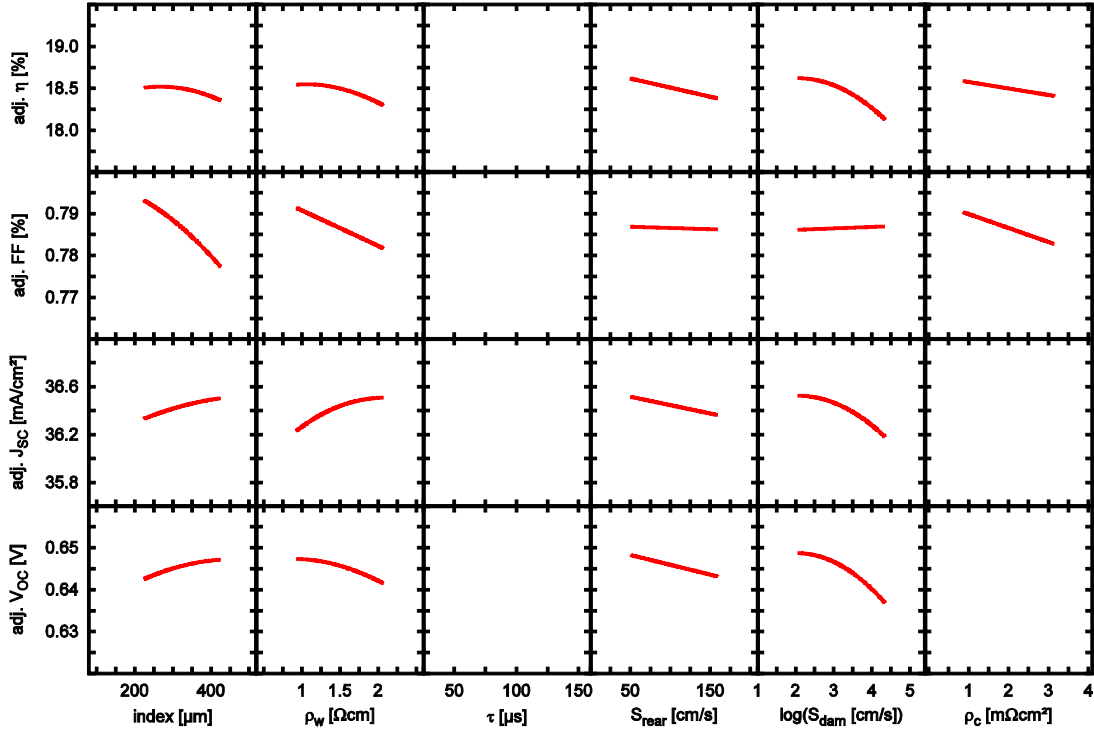


Figure 10: Adjusted response graph of the lifetime-resistivity relation corrected metamodel for the correlations between the influencing factors and the cell parameters. The metamodel is given as curves which are adjusted by setting all of the other factors to their central point according to Figure 5. The influencing factors are the index d_i (half the distance between the local rear contacts = half pitch), the wafer resistivity ρ_w , the wafer SRH lifetime τ , the rear metal contact resistivity ρ_c , the recombination velocity at the rear dielectric layer S_{rear} , and near the rear metal contacts S_{dam} . Note the changes in efficiency with the variation of ρ_w .

E. Overview about the corrected metamodels

The complete overview of the corrected metamodels is shown in Figure 11. The metamodels for η , FF , J_{SC} and V_{OC} obtained at first are given in light gray. The metamodels which consider optical shading and emitter/finger resistance are shown in blue. Optical shading of 10% mainly reduces J_{SC} , while the additional series resistance contributions lower mainly FF . The consideration of a lifetime-resistivity relation results in the metamodels shown in red. As τ decreases for lower ρ_w (see Eq. (8)), η saturates and lowers for lower ρ_w . The third column is missing, because τ is a function of ρ_w .

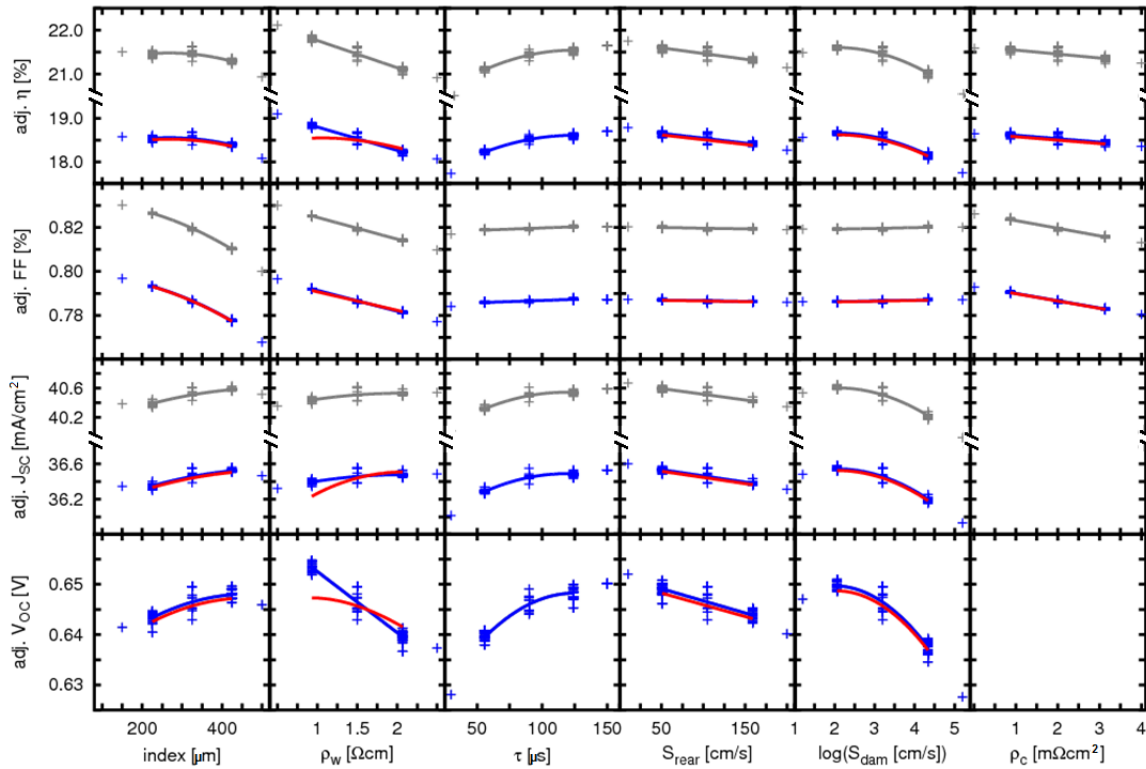


Figure 11: Adjusted response graph for the correlations between the influencing factors and the cell parameters. The metamodel is given as curves, and the crosses mark the 77 numerical simulations projected on the graphs. All curves and crosses are adjusted by setting all of the other factors to their central point of Figure 5. The influencing factors are the index d_i (half the distance between the local rear contacts = half pitch), the wafer resistivity ρ_w , the wafer SRH lifetime τ , the rear metal contact resistivity ρ_c , the recombination velocity at the rear dielectric layer S_{rear} , and near the rear metal contacts S_{dam} . The correlation obtained at first is given in light gray, with optical shading and emitter resistance included in blue, and with the coupling between τ and ρ_w in red.

2.2.3 Sensitivity analysis

A. Example of an optimization

Once a metamodel for an improved cell design is set up, it can be readily used for finding the global maximum of cell efficiency. I use the optimization function ‘sqp’ in GNU Octave [76] for several scenarios, with the results listed in Table V.

Table V: Scenarios for the optimization with the metamodel.

Scenario	d_i [μm]	ρ_w [Ωcm]	S_{rear} [cm/s]	$\log(S_{\text{dam}})$ [cm/s)]	ρ_c [$\text{m}\Omega\text{cm}^2$]	η_{max} [%]
1	225.6	1.31	51.0	1.86	0.87	18.95
2	321.6	1.12	51.0	3.00	0.87	18.74
3	282.9	1.16	51.0	3.00	2.01	18.67
4	268.1	1.50	51.0	3.00	2.01	18.64

In scenario 1, all input parameters are left free in the valid range of the metamodel, which is between the lower and upper cube points given in Table III. The efficiency can be maximized to 18.95%. For scenario 2, S_{dam} is fixed at its center value of 3.0 log(cm/s), taking into account the damaged dielectric layer around the contacts in industrial production. This reduces the maximum of η to 18.74%, with an increased index and a lower ρ_w . In scenario 3, the rear contact resistivity ρ_c is also fixed at 2 $\text{m}\Omega\text{cm}^2$; and in scenario 4, ρ_w is also set to 1.5 Ωcm , because multicrystalline wafers may be available within only a rather narrow resistivity specification.

I point out that the resistivity and the index of a PERC cell show nontrivial maximum of efficiency. Other solar cell designs might be more complex and benefit even more by metamodeling.

B. Local sensitivity analysis

The sensitivity analysis quantifies the strength of an influencing factor x_j on a responding cell parameter E_i . To measure that, the derivative $E_{ij}(x) = dE_i(x)/dx_j$ is calculated at a specific point x in the metamodel. For example, in Table VI the sensitivity analysis is carried out at the center point (defined in Table III) for η , FF , J_{SC} and V_{OC} .

Table VI: Comparison of the local absolute sensitivity at the center point.

	d_i	ρ_w	τ	S_{rear}	$\log(S_{\text{dam}})$	ρ_c
η	-7.5×10^{-4} %/μm	-0.54 %/Ωcm	5.0×10^{-3} %/μs	-2.2×10^{-3} %/(cm/s)	-0.22 %/log(cm/s)	-0.08 %/mΩcm ²
FF	-7.9×10^{-3} %/μm	-0.95 %/Ωcm	2.1×10^{-3} %/μs	-6.0×10^{-4} %/(cm/s)	0.03 %/log(cm/s)	-0.33 %/mΩcm ²
J_{SC}	8.5×10^{-4} (mA/cm ²)/μm	0.07 (mA/cm ²)/Ωcm	2.6×10^{-3} (mA/cm ²)/μs	-1.4×10^{-3} (mA/cm ²)/(cm/s)	-0.15 (mA/cm ²)/ log(cm/s)	0 (mA/cm ²)/ mΩcm ²
V_{OC}	2.3×10^{-5} mV/μm	-12.2 mV/Ωcm	0.12 mV/μs	-4.8×10^{-2} mV/(cm/s)	-5.3 mV/log(cm/s)	0 mV/mΩcm ²

To be able to compare the strength of one influencing factor on each cell parameter E , I calculate the sensitivity in relative terms by $E_{ij}(x)/E_i(x)$, as listed in Table VII. Then, the derivative – for example of η – is the sum of the derivatives of FF , J_{SC} and V_{OC} , which might balance out. The values in Table VII show that the index d_i has the strongest influence on FF , while ρ_w has the strongest influence on V_{OC} , etc. Another option for attaining an overview of the global sensitivity of a cell concept is the interaction graph shown in Figure 8. There, non-linear dependencies and interactions are included, so the slopes of the curves are a measure of the sensitivity.

Table VII: Comparison of the local relative sensitivity at the center point.

	d_i	ρ_w	τ	S_{rear}	$\log(S_{\text{dam}})$	ρ_c
η	-4.1×10^{-3} %/μm	-2.9 %/Ωcm	27.1×10^{-3} %/μs	-12.1×10^{-3} %/(cm/s)	-1.19 %/log(cm/s)	-0.42 %/mΩcm ²
FF	-10.0×10^{-3} %/μm	-1.2 %/Ωcm	2.6×10^{-3} %/μs	-0.8×10^{-3} %/(cm/s)	0.04 %/log(cm/s)	-0.42 %/mΩcm ²
J_{SC}	2.3×10^{-3} %/μm	0.2 %/Ωcm	7.0×10^{-3} %/μs	-3.9×10^{-3} %/(cm/s)	-0.41 %/log(cm/s)	0 %/mΩcm ²
V_{OC}	3.6×10^{-3} %/μm	-1.9 %/Ωcm	17.7×10^{-3} %/μs	-7.5×10^{-3} %/(cm/s)	-0.83 %/log(cm/s)	0 %/mΩcm ²

C. Calculation of cell parameter distributions

The cell–fabrication processes are not perfectly stable, which causes a distribution of cell parameters. To model this distribution, the sensitivity analysis in the previous paragraph is insufficient, because it is only a local study at a point x . It is necessary to describe each influencing factor x over an entire distribution.

The variation in a fabrication process may be characterized by its impact on an influencing factor x_j . One may use a measured distribution of x_j caused by the process tool. Alternatively, one may take a normal distribution of x_j from the process capability index C_{pk} , which describes the process variation relative to specification limits. Or one may derive the distribution of x_j via the Monte Carlo method [46]. I follow this path as shown in Figure 12, because the simplicity of the metamodel, Eq. (6), allows me to apply 20,000 Monte Carlo trials very quickly. By defining a normal distribution $N(\mu, \sigma)$, two standard deviations $\pm\sigma$ include approximately 68.3 percentiles, and the 10th/90th percentile is approximately $\pm 1.28 \times \sigma$.

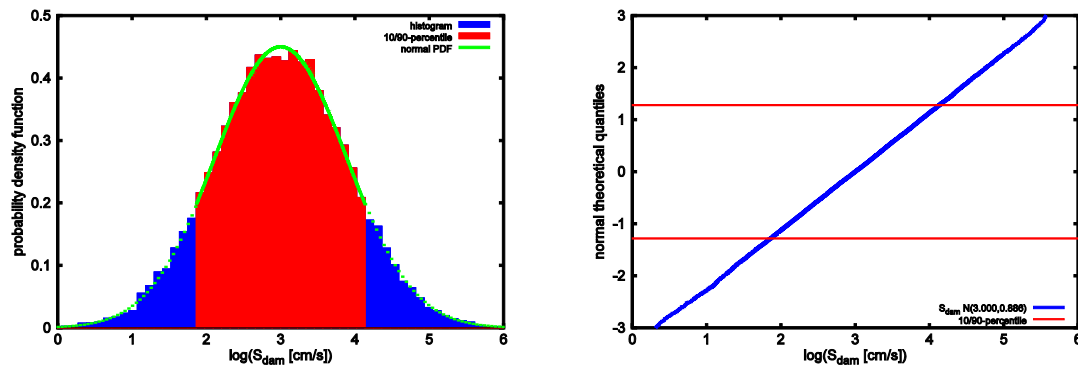


Figure 12: Left: Probability density function (PDF) and histogram generated by 20,000 random numbers of a normal distribution $N(3.0, 0.886)$ for the factor $\log(S_{dam})$, on a logarithmic scale; and right: Normal probability plot of the same distribution generated by random numbers. A line indicates a normal distribution, as expected. The mean value is defined by the central point of the DoE, i.e. $S_{dam} = 1 \times 10^3$ cm/s, and the standard deviation ($\sigma = 0.886 \log(\text{cm/s})$) is defined by the 10th and 90th percentile which is the upper and lower cube points, i.e. $S_{dam} = 73$ cm/s and $S_{dam} = 1.4 \times 10^4$ cm/s, respectively.

Here, the mean value μ is defined by the central point of the DoE, which is, e.g., $S_{\text{dam}} = 1000$ cm/s, while the 10th and 90th percentiles are the upper and lower cube points in Figure 5, i.e. $S_{\text{dam}} = 73$ cm/s and $S_{\text{dam}} = 1.4 \times 10^4$ cm/s, respectively. Note that the variation of S_{dam} may represent not only a specific fabrication process (such as laser damage), but also the influence of all the processes on rear contacting.

Such distributions of the influencing factors x_j can be used as an input for the metamodel for deriving the distributions of the cell parameters. Figure 13 shows the cell efficiency distribution caused solely by the distribution of S_{dam} , which is the assumed normal distribution $N(3.000, 0.886)$ for $\log(S_{\text{dam}})$.

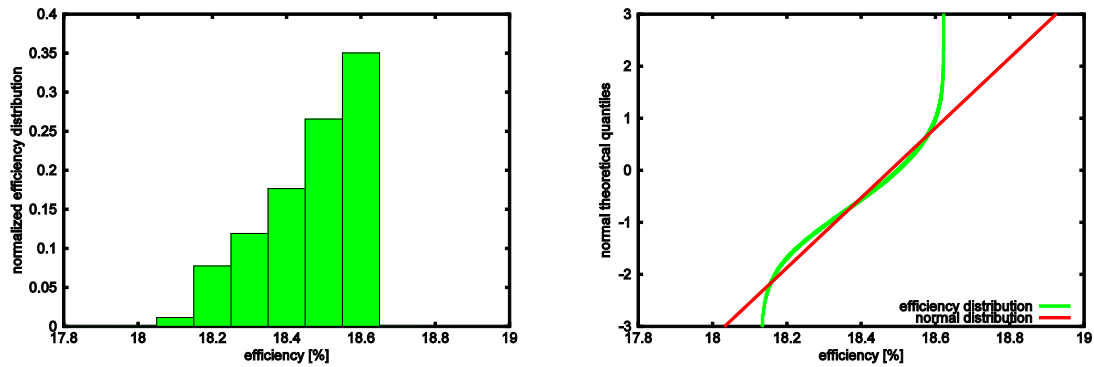


Figure 13: Left: Normalized efficiency distribution derived by the metamodel (see Figure 10) assuming a normally distributed S_{dam} (see Figure 12). The efficiency bins are similar to the sorting of solar cells after production; and right: Normal probability plot of the same efficiency distribution. The line is a guide to the eye to check normal probability as it is pinned to the 25th and 75th percentile of the distribution. Due to the non-linear dependence of the efficiency on S_{dam} , the resulting efficiency distribution is skewed towards higher efficiency.

Only the 10th to 90th percentile range is taken into account which is the valid range for the metamodel. Due to the non-linear dependence of the efficiency on S_{dam} , the resulting efficiency distribution is skewed towards higher efficiency.

The variation of cell efficiency caused by all input factors can be closely approximated by considering the most important influencing factors within the 10th to 90th percentile range, which are S_{dam} , ρ_w and ρ_c . For S_{dam} and ρ_c I use $N(3.000, 0.886)$ and $N(2.005, 0.884)$, respectively; for ρ_w I use a broad case, $\rho_w(1) - N(1.500, 0.443)$, or a narrow case $\rho_w(2) -$

$N(1.157, 0.044)$, which applies if similar wafers of one ingot with a similar ρ_w are used. The normal probability plot of their distributions is shown in Figure 14.

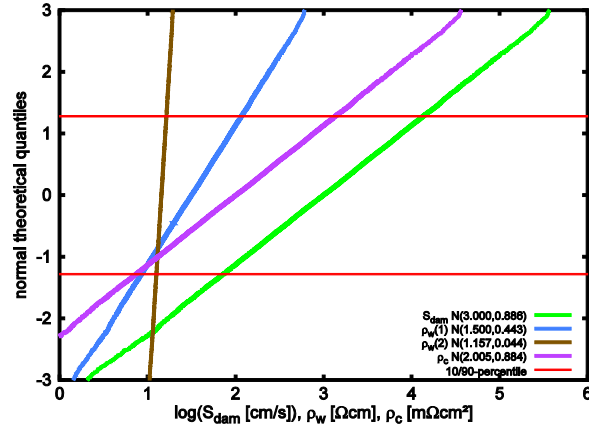


Figure 14: Normal probability plot of the variation of S_{dam} , ρ_w and ρ_c . All parameters are normally distributed $N(\mu, \sigma)$ with the mean value μ and the standard deviation σ , while only the 10th to 90th percentile range is taken into account. Two different distributed wafer resistivities are shown $\rho_w(1)$ and $\rho_w(2)$, which accounts for the fact that a wafer resistivity specification is broad in case of $\rho_w(1)$, but during experiments usually similar wafers of one ingot with similar ρ_w are used, as described by $\rho_w(2)$.

The variation of d_i and S_{rear} is typically small during solar cell fabrication, so these parameters are set to the optimal values of scenario 3 of the optimization (see Table V). The impact of the variation of S_{dam} , ρ_w and ρ_c on cell efficiency is shown as red bars and red dashed lines, respectively, in Figure 15. The hashed green bars and solid green line in Figure 15 is similar to Figure 13 and added for comparison.

Going from case 1, the variation of the sole input factor S_{dam} , to case 2 (blue), the combined variation of the input factors S_{dam} , ρ_w and ρ_c , it is apparent that the mean efficiency remains similar, but the efficiency distribution broadens and the skewness decreases. The reduction in skewness follows from the central limit theorem in probability theory. This implies that, if the efficiency distribution were very close to a normal distribution, one could assume that the several main influencing factors have only a linear influence and do not interact with each other. However, this is usually not the case in real-world fabrication. In the example, the shape of the efficiency distribution is skewed because it is predominantly influenced by S_{dam} .

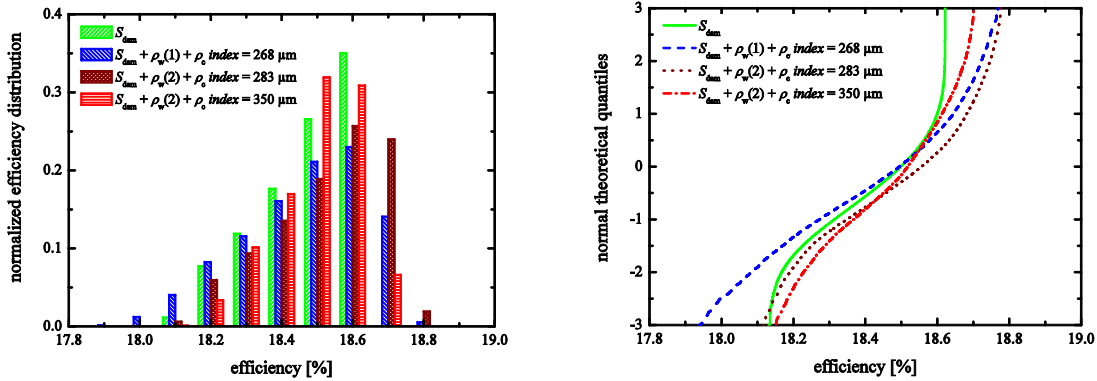


Figure 15: Left: normalized efficiency distributions, derived from the metamodel of Figure 10; and right: normal probability plot of the same efficiency distributions. Either only S_{dam} is distributed (case 1 in green), or the most important influencing factors (S_{dam} , ρ_w and ρ_c) with various index values (cases 2–4) are distributed.

With this kind of analysis, the efficiency distribution in a running cell production may be explained, and/or the efficiency variation of a future cell concept may be predicted. Additionally, this analysis may be used as a tool for manipulating the efficiency distribution. For example, the efficiency distribution may be made narrower by using a smaller wafer resistivity distribution and a higher index, as shown in Figure 15 as case 3 (brown). There are higher efficiencies at the lower end of the distribution because the metallized area at the rear side is reduced, as is its influence. The lower efficiencies at the higher end of the distribution are caused by the increased spreading resistance in the bulk and the reduced rear contact area. While the efficiency distribution is narrower, the mean efficiency decreases from 18.53 %_{abs} to 18.50 %_{abs}, although the narrower ρ_w -distribution is centered on $\rho_w = 1.157 \Omega\text{cm}$, where maximum efficiencies are reached (see Table V, scenario 3). This strategy may still be economically beneficial because a smaller number of cells with an efficiency lower than a defined minimum are fabricated, so defective goods are reduced.

Another purpose in adjusting the broadness of the efficiency distribution may be to increase the number of fabricated cells that have a very high efficiency level. This may be reached in case 4 by decreasing the index (see red bars and red dashed dotted line in Figure

15). While the efficiency distribution broadens, a larger number of very efficient cells may be sold for a higher price. This strategy may also serve to produce a record cell from a minimal number of specimens.

D. Planning of experiments

The strategy so far has been, firstly, to analyze an improved cell design with the metamodel; secondly, to predict the input parameters for the maximally attainable cell efficiency; and, thirdly, to calculate the expected cell efficiency distribution at this maximum. In a further step, the metamodel can now be used for planning the initial experiments. Knowing the optimum starting point speeds up the experimental development work.

To find the optimum starting point, it is crucial to know (i) the interaction between factors, and (ii) the variation of the cell output parameters that these factors are causing. For example, Figure 8 indicates that there is a strong interaction between the index d_i and the laser damage S_{dam} . This indicates that, to set up an experimental series to investigate the variation of the laser damage, the index should be minimized, as this increases the impact of the laser damage [77]. While this may seem trivial here, finding optimum starting points may be far from trivial for other experimental series.

2.3 Application and validation of metamodeling on mc Al-BSF solar cell production

In solar cell mass production, the mean cell efficiency is not the only important parameter, but also the variation of the cell efficiency [19]. It is shown how the cell efficiency variation of an Al-BSF cell production can be understood, predicted and reduced by changes to specific process steps. The main influencing cell parameters are identified from the *SolarWorld* quality management. Again, the variation is modeled in a combination of numerical device simulation and advanced statistical analysis and a metamodel is derived.

2.3.1 Production monitoring

The *SolarWorld* quality management of the mc solar cell production considers all available optical and electrical parameters. In particular, it is the parallel and lumped series resistances, the deviations from the ideal I-V-curve (J_{02}), the quantum efficiency at different wavelengths, emitter and base doping, the characteristics of the reflectance curve and metallization properties such as contact resistivity and finger line resistivity, etc. A subset of randomly chosen cells from production is created and in-depth characterized. From this data set, the in-depth production monitoring is carried out doing statistical modeling [19] to identify the main influencing factors for the I-V parameter variation, i.e. for the variation of η , FF , J_{SC} and V_{OC} .

These are (i) the wafer SRH lifetime τ , which is derived from wafer lifetime distributions measurements of Al_2O_3 passivated lifetime samples which are produced of former cells etching off metallization, emitter and BSF [66], (ii) the wafer resistivity ρ_w , which is measured at the mc ingot, (iii) the concentration of aluminum–oxygen complexes (Al–O complexes) in the back surface field (BSF), which is taken from the interstitial oxygen concentration O_i measured at mc ingots, (iv) the emitter saturation current density J_{0e} , which is measured applying the method of Kane and Swanson on textured J_{0e} samples [22], (v) the silicon-nitride ARC thickness w_{SiNx} , which is derived by ellipsometer measurements, (vi) the contact resistivity ρ_c , which is determined by TLM measurements, and (vii) the finger line resistivity $\rho_{f,line}$, which is measured with a h.a.l.m. I-V-tester.

The distribution of $\rho_{f,line}$ is shown in Figure 16 as an example. The I-V parameters are measured also with a flash I-V-tester from h.a.l.m. such as short-circuit current density J_{SC} , open-circuit voltage V_{OC} , fill factor FF and efficiency η .

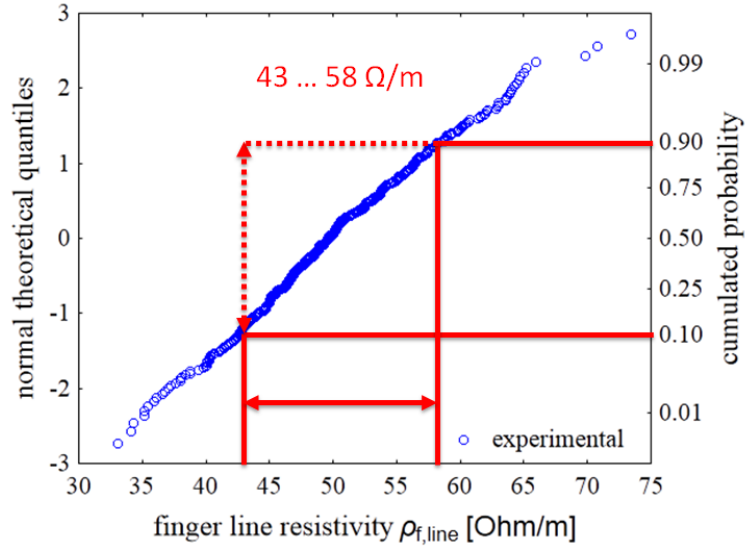


Figure 16: Variation of the finger line resistivity $\rho_{f,line}$ of a mc Al-BSF solar cell production.

2.3.2 Metamodeling

A. Device model

For the numerical solution of the semiconductor differential equations in the drift-diffusion approach, the software TCAD Sentaurus Device [39] and state-of-the-art physical models [36] [61] [62] are used. The photogeneration profile is obtained with the ray-tracing software SUNRAYS [41], and the front metallization is included with LTspice [63], as shown schematically in Figure 17.

The simulation model for a multicrystalline Si solar cell is set up, following the approach in Ref. [66], where the benefit of a lifetime averaging procedure is described. All dopant profiles are independently measured with the electrochemical capacitance-voltage technique (ECV) using the CVP21 profiler [78] and the procedure described in Ref. [79]. The front surface recombination velocity S_{front} is adjusted such that the saturation current density J_{0e} of the emitter is reproduced on independently fabricated J_{0e} samples.

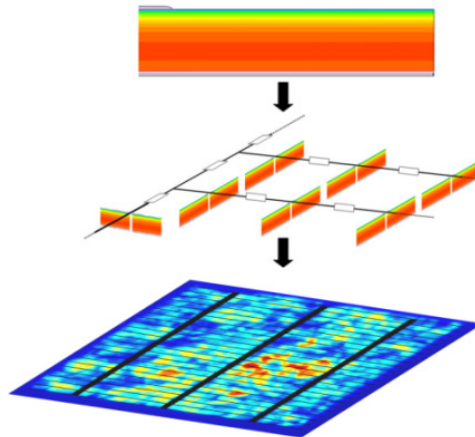


Figure 17: Simulation approach for a mc-Si cell: a 2D TCAD model (top) is combined with a circuit (SPICE) simulation (middle) to represent the entire solar cell (bottom).

The wafer SRH lifetime is derived from wafer lifetime distributions of Al_2O_3 -passivated lifetime samples which are produced of former cells etching off the metallization, the emitter, and the BSF (for details see Ref. [66]). The recombination losses of the Al-BSF are considered in a similar study to Ref. [62]. For the correct reproduction of the Fill Factor FF , additional influences are lumped, e.g. from the edge recombination, in a lumped series resistance ΔR_s . The simulated I-V-curve is finally corrected for this ΔR_s .

B. Variation of parameters in the device model

To incorporate the influence of variations into the device model, seven input parameters (factors) are varied in a systematic, Central Composite Faced Design of Experiments (DoE), as exemplified in Figure 18 for three dimensions. The Central Composite design is appropriate for a second order (quadratic) response model, where two-factor interactions are considered.

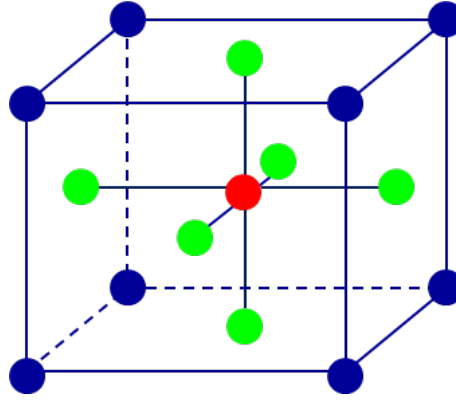


Figure 18: Central Composite Faced Design of Experiments (DoE) for three influencing factors: axial points are marked in green, cube points are marked in blue and the center point is marked in red. The DoE is used to apply variations into the TCAD model.

The variations of the seven identified parameters are taken from the *SolarWorld* quality management, i.e. (i) the wafer SRH lifetime τ variation, which is derived from wafer lifetime distributions of Al_2O_3 passivated lifetime samples of former cells, which are chosen by their V_{OC} and ingot position, (ii) the wafer resistivity ρ_w variation, which is derived from the resistivity measurements of the mc ingot production, (iii) the variation of the concentration of aluminum–oxygen complexes in the back surface field (BSF), which is derived from the variation of the interstitial oxygen concentration O_i measured over mc ingots, (iv) the variation of the J_{0e} , which is taken from the J_{0e} distribution over a POCl_3 diffusion boat, (v) the variation of the silicon-nitride ARC thickness w_{SiNx} , (vi) the contact resistivity ρ_c , which is determined by the print and firing process, (vii) the finger line resistivity $\rho_{f,\text{line}}$, which is determined by the print and firing process. In Figure 16, the variation of $\rho_{f,\text{line}}$ is shown as an example.

C. Evaluation of the DoE – response surface methodology (RSM)

Each influencing parameter is varied again within its measured 10th – 90th percentile range in the DoE and 144 numerical device simulations are carried out. The simulation results are analyzed with the response surface methodology (RSM) [45], which is applied to the simulated efficiencies to derive the metamodel [35]. For that, a least-square fit is carried out again using the software JMP from SAS [65] to determine the coefficients of the metamodel. The derived metamodel is based on the second-degree

polynomial equation (6) with linear, quadratic and two-factor interaction terms. The influencing factors x are τ , ρ_w , O_i , J_{0e} , w_{SiNx} , ρ_c and $\rho_{f, \text{line}}$ while the response E is η , J_{SC} , V_{OC} and FF , respectively.

Again, the significance of each term of the polynomial function is tested as a predictor for cell parameters by means of a multivariate regression analysis, applying a rather strict significance level of less than 0.01 as the criterion for inclusion. The normal probability assumption is tested for the residuals, and this ensures that the model is consistent. Finally the model with only the highest coefficient of determination (adjusted R-squared) is chosen.

For the study of the variation of the mc cell production a period of time of more than one month is considered, where the crystallization and cell processes are not changed.

2.3.3 Studentization

The influencing parameters x and the response E is studentized because the focus is on the variation of the parameters. The studentized quantity z_i of a variable y_i is derived subtracting the estimate of the mean \bar{y} of its distribution and dividing by its estimate of the standard deviation s_y :

$$z_i = \frac{y_i - \bar{y}}{s_y} \quad (9)$$

The studentized distribution of $\rho_{f, \text{line}}$ is exemplified in Figure 19.

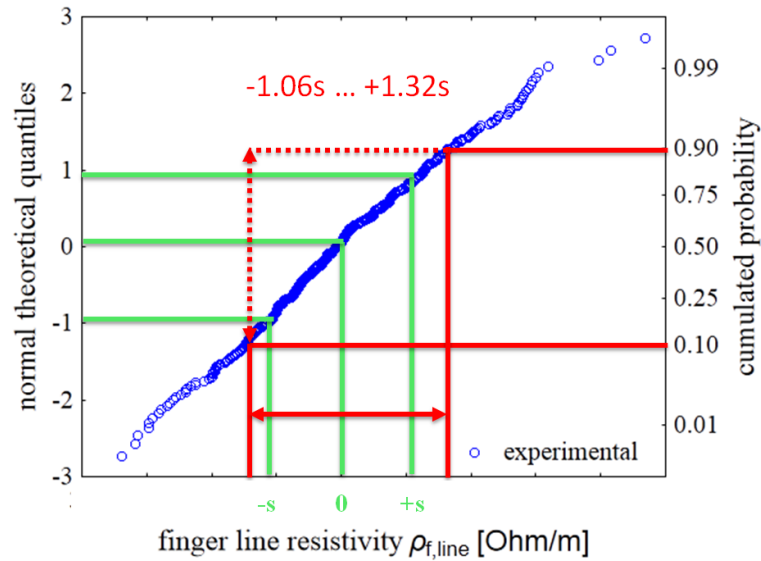


Figure 19: Studentized variation of the finger line resistivity $\rho_{f, \text{line}}$ of a mc Al-BSF solar cell production. For the not studentized distribution see Figure 16.

2.3.4 Response surface

The adjusted response graph in Figure 20 shows the 28 correlations between the individual factors x and the I–V parameters E such as cell efficiency. The red I–V parameter curves are the adjusted response of the metamodel setting the other factors to their mean (central) value, while the blue crosses are the adjusted simulated data. Each subgraph is a cross-section of the seven-dimensional response surface holding six dimensions at their mean value. Alternatively, one could have an interacting graph with adjustable input parameters changing the 28 subgraphs at the same time. The influencing parameters x and the response E are again studentized because the focus is on the variation of the parameters. The two-factor interaction terms have only a minor influence on cell parameters, i.e. within the metamodel the linear and quadratic dependencies are dominating. As the wafer lifetime is assumed and modeled to be independent of the wafer resistivity, the known interaction due to the boron–oxygen complex [72] [73] [74] is not considered. For better multicrystalline material quality, which might be limited by the B-O-complex, the interaction between wafer lifetime and wafer resistivity might be more significant.

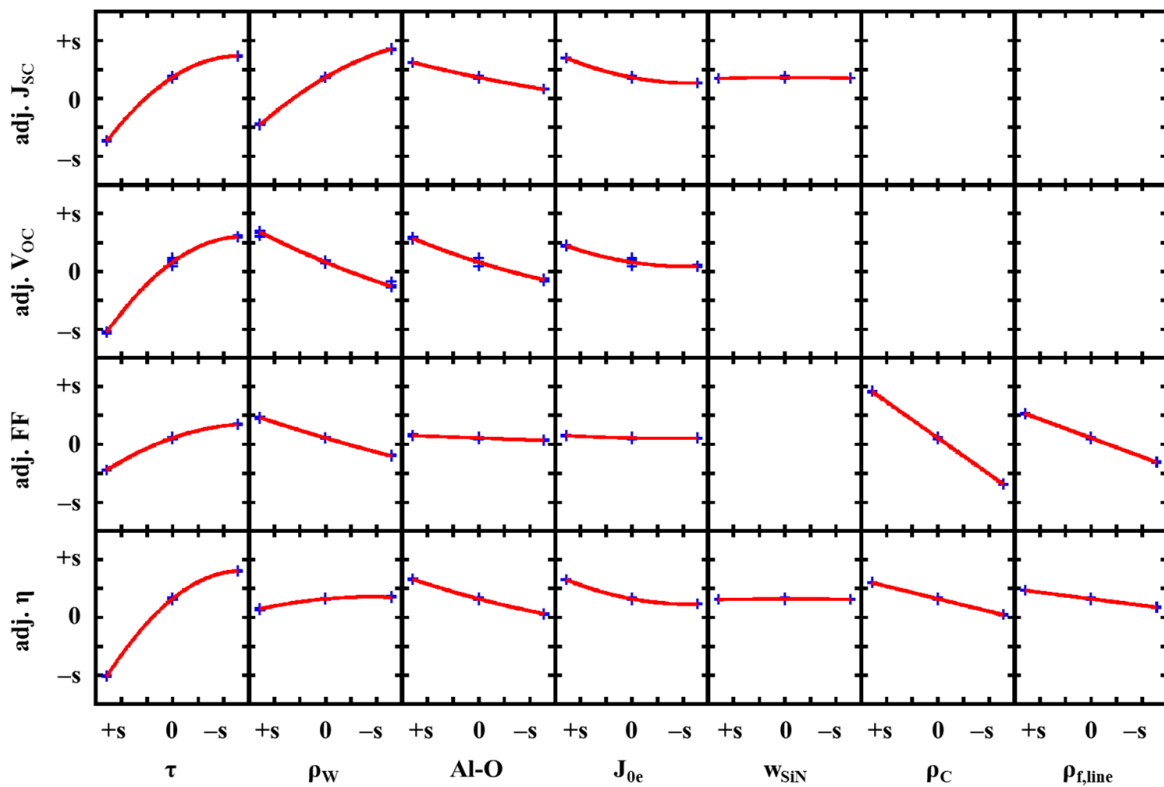


Figure 20: Adjusted response graphs for the response of the I–V parameters such as cell efficiency η influenced by the following factors: wafer SRH lifetime τ , wafer resistivity ρ_w , wafer oxygen concentration forming Al–O complexes in the Al–BSF, emitter saturation current density J_{0e} , thickness of the SiN ARC w_{SiN} , contact resistivity ρ_c and finger line resistivity $\rho_{f,\text{line}}$. Some subgraphs are empty because the influencing parameter is not significant within the metamodel (polynomial expression), which is derived by the RSM. All quantities are studentized according to Eq. (9). The red curves are the adjusted response of the metamodel (while the other factors are set to their mean value). The blue crosses show the adjusted studentized simulated data points.

2.3.5 Validation of the metamodeling strategy

From Figure 20, I derive how strongly each parameter influences the variation on cell efficiency (by the difference of their maximum and minimum efficiency). The resulting parameter pareto graph for the variation of efficiency is shown in Figure 21. Note that Figure 21 does not show a pareto of a loss analysis, but does show the main reasons (influences) for cell efficiency variations in production.

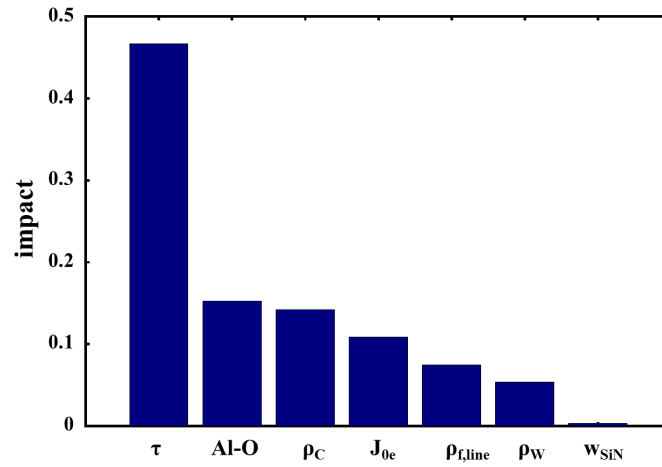


Figure 21: Pareto graph: normalized strength of each influencing parameter on the variation of the cell efficiency. The wafer lifetime currently influences the variation in the efficiency in a mc solar cell production the most.

In order to compare the simulated parameter distributions with the distributions observed in production, all input parameters are varied at the same time in the metamodel, i.e. I create again a normally distributed parameter by random number generation. By definition of a normal distribution $N(\mu, \sigma)$, two standard deviations $\pm\sigma$ include approximately 68.3 percentiles, and the 10th/90th percentile is approximately $\pm 1.28 \times \sigma$. Figure 22 exemplifies the variation of the finger line resistivity $\rho_{f,line}$ within the 10th and 90th percentile. I apply the normally distributed variation to all input parameters within the 10th to 90th percentile range and calculate an efficiency distribution from the metamodel, which is shown in Figure 23 (red line). The blue circles in Figure 23 show for comparison the studentized cell efficiency distribution from the *SolarWorld* quality management. Both distributions are studentized according to Eq. (9). The mean value as well as the shape of the distribution are reproduced very well with the model. This indicates that this model contains all the relevant variations in the cell fabrication and therefore points to the main causes for the cell output variations. This is expected, because the model does not contain other root causes for very bad cells such as shunting, strong firing problems, etc. Those defects are not considered within the model and/or in its 10th – 90th percentile range.

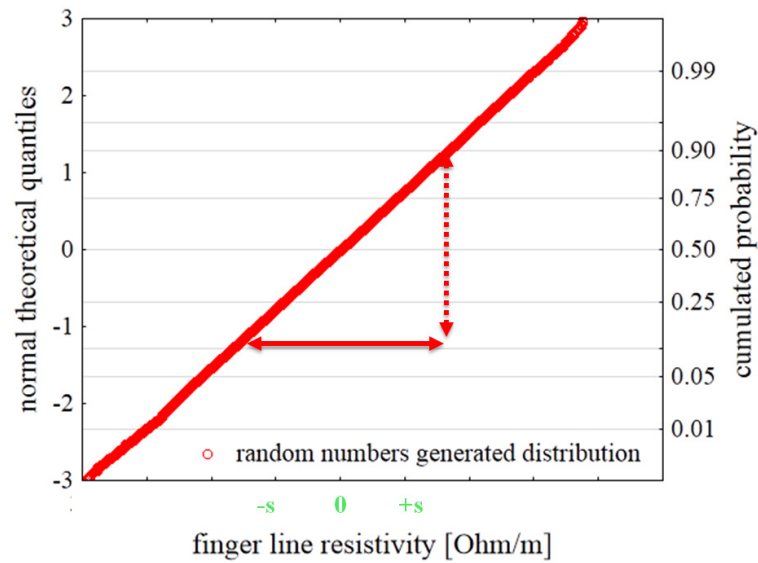


Figure 22: Random numbers generated distribution of the finger line resistivity $\rho_{f, \text{line}}$ by 20000 trails. The distribution exemplifies the variation for one input parameter, whereas the concurrent variation of all parameters as an input of the metamodel yields the efficiency distribution shown in Figure 23.

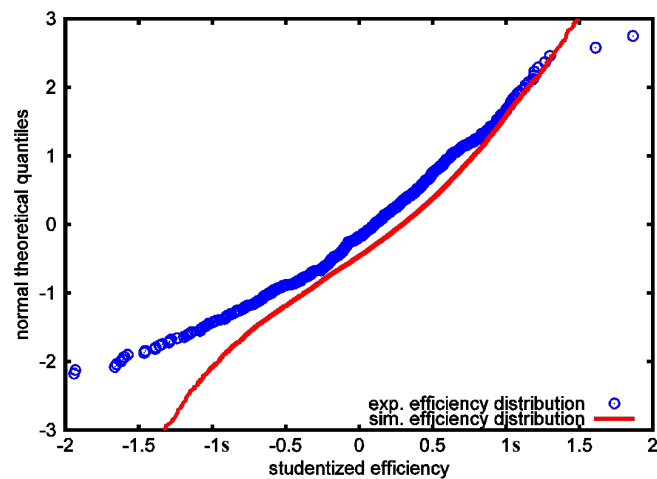


Figure 23: Comparison of the experimental and the simulated efficiency distribution in a normal probability plot. Both studentizations are carried out with Eq. (9), while the estimate of the mean and the estimate of the standard deviation are taken from the production cell efficiency distribution. The simulated distribution matches the observed distribution very well, except at efficiencies that are lower than about one standard deviation from the mean value.

2.4 Conclusion

A method is presented to quickly evaluate a significantly reduced set of time-consuming numerical simulations on the example of industrial multicrystalline PERC silicon solar cells. It is successfully applied to multicrystalline Al-BSF solar cells for validation. The method is based on a Design of Experiment approach, which is evaluated using the response surface methodology, deriving an analytical description of the response surface, called metamodel. The advantage of such a metamodel is that it includes the mutual non-linear interactions between device parameters. It is shown that the metamodel can be extended in hind-sight by linear and non-linear terms, e.g. to consider finger shading or lifetime degradation. Metamodeling allows for an accurate and comprehensive overview of the response surface and for a quick calculation of a modeled distribution, e.g. by the Monte Carlo method, which incorporates the influencing parameter variation into the metamodel.

For the multicrystalline PERC solar cell analysis, the metamodel is applied (i) to maximize cell efficiency; (ii) to perform a sensitivity analysis, where the local impact of each input parameter is quantified; (iii) to compute and manipulate the variation in cell efficiency due to variations in fabrication processes; and (iv) to plan experiments more strategically. It is inferred from the shape of the efficiency distribution that one important influencing factor is the damaged dielectric layer around the contacts. Additionally, I may deliberately adjust the broadness of the efficiency distribution by choosing certain device parameters. This may reduce the number of cells with low efficiency, and/or increase the number of cells with a high cell efficiency class and enable selling them at a higher price.

For the multicrystalline Al-BSF solar cell production, I could validate the metamodeling strategy by modeling successfully the observed production variations. The data analysis shows that the wafer lifetime τ is the biggest influence on the efficiency variation in a mc solar cell production.

In short, the metamodeling strategy offers a way to do optimization, e.g. efficiency maximization, to reduce the variations in I–V parameters, and to improve the production yield.

3. Methods and models for the front side characterization of solar cells with selective emitters

3.1 Front side contact resistance measurements on solar cells with selective emitter

3.1.1 Introduction

The transfer length method (TLM) [52] [80] is most successfully applied when measuring the resistances of metal-semiconductor contacts placed on a thin conductive sheet layer. It was originally proposed by Shockley in 1964. A typical example is the front contact fingers on the emitter layer of solar cells. The applied current is flowing through each contact and through the conductive sheet layer. The voltage drop between two contacts is measured varying the contact distance d (see Figure 24). It allows the separation of the contact resistance $R_{C,TLM}$ in Ω from the sheet resistance ρ_{SH} in Ω/\square .

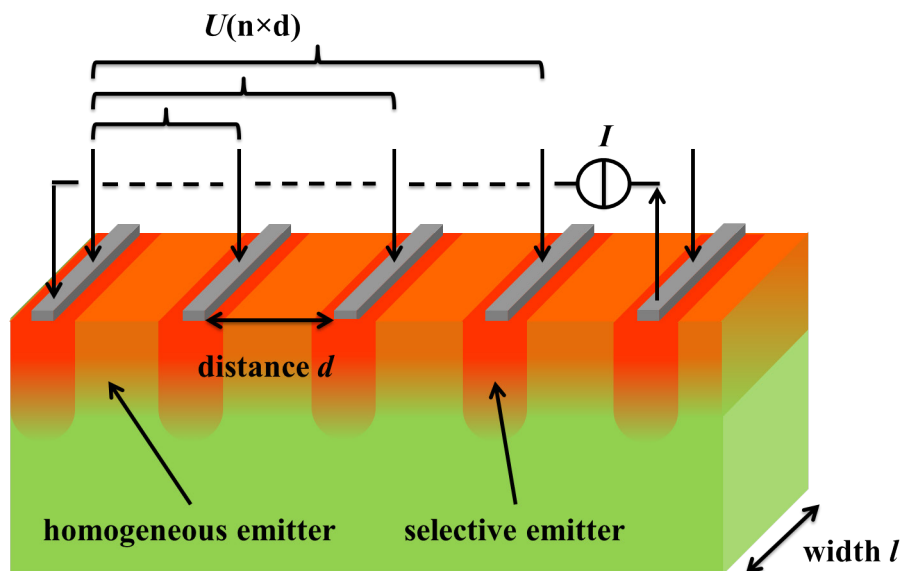


Figure 24: Schematic of a transfer length method (TLM) test stripe. The selective emitter is not obligatory but shown here as it is of interest for the investigated structures in chapter 3.1.

Unfortunately, the same abbreviation TLM is used for the term transmission line model [81]. The idea behind the word is that the current within the sheet layer entering the contact from one side partly transfers into the contact and proceeds flowing beneath the contact depending on the contact resistivity. The transmission line model accounts for current crowding [82] below the contact. But the same holds true for the transfer length method (TLM). The difference between the two notions turns out to be that the transfer length method (TLM) test structure has more than three contacts compared to the transmission line model test structure [83]. The TLM test structure is also called *ladder* structure (see Figure 24). The name of TLM is based on the transfer length L_T . L_T is the distance beneath the contact where the voltage drops to $1/e$ of the voltage at the edge of the contact due to the contact resistance. The transfer length could be described by the idea that all current travels the distance of L_T within the sheet layer and then enters the contact abruptly and completely [80]. For solar cells, the contact width w_C is typically in the same order of magnitude as the transfer length. A good introduction and overview about contact resistance and its measurement may be found in chapter three of Ref. [83].

As shown in Figure 24, solar cells may be fabricated with different emitters, i.e. different sheet resistances, underneath and between the contacts. The standard TLM theory does not take account of such structures called selective emitter. Within this chapter, I develop a test structure and its theory to separate homogenous emitter sheet resistance, selective emitter sheet resistance and contact resistivity within a TLM measurement. Additionally, I focus on the influence of intermediate, not contacted fingers on a TLM measurement of TLM test structures made of solar cells (see Figure 24), which is typically not accounted for.

3.1.2 Standard TLM measurement on solar cells

For transfer length method measurements, a special layout of the test structures is necessary. Standard TLM test structures are shown in Figure 25.

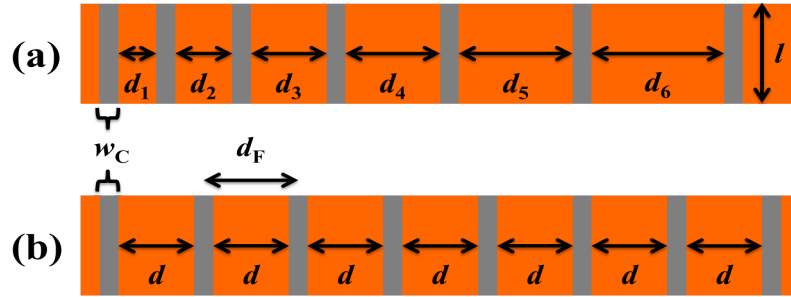


Figure 25: Schematics of the TLM test structures with contacts in grey and emitter area in orange. (a) Structure with varying contact distance d_i and (b) with constant contact distance d . The case (b) is often used for solar cells as it may be cut out of fabricated solar cells.

Two different types are distinguished here. One structure is with varying contact distance d_i , where only two neighboring contacts are contacted during a measurement. The other structure is with constant contact distance d . This TLM test structure is contacted and measured at all contact combinations. This case is often used for solar cells as it may be cut out of manufactured solar cells by e.g. laser processing and breaking. Below it is called solar cells TLM test structure. A major advantage of this solar cell TLM test structure is the identical firing conditions in the belt furnace.

The series resistance network of a TLM test structure describes

$$R_{TLM}(d) = 2R_{C,TLM} + R_{homEm}(d) = 2R_{C,TLM} + d \frac{\rho_{SH}}{l} \quad , \quad (10)$$

where l is the width of the structure. The distance independent contact resistance $R_{C,TLM}$ (in Ω) is separated from the emitter resistance R_{homEm} (in Ω), which depends on the distance d . The contact resistance $R_{C,TLM}$ (in Ω) depends on the sheet resistance under the contact (in Ω/\square) and the contact resistivity (in $m\Omega cm^2$). $R_{C,TLM}$ is defined by [52]

$$R_{C,TLM} = \rho_{SH,homEm} \frac{L_T}{l} \coth\left(\frac{w_C}{L_T}\right) \quad , \quad (11)$$

where $\rho_{SH, homEm}$ is the emitter sheet resistance of the homogeneous diffusion (in Ω/\square) and the transfer length L_T is defined by

$$L_T = \sqrt{\frac{\rho_C}{\rho_{SH, homEm}}} . \quad (12)$$

For the evaluation of TLM measurements the following assumptions are typically made.

1. The semiconductor sheet thickness is assumed to be zero, which is in general fulfilled as typical emitters are below 1 μm depth and industrial emitters even below 0.5 μm depths, compared to contact distances of about 2000 μm .
2. Fingers/contacts, typically containing mostly silver, are assumed to have an infinite conductivity, which allows the current and voltage probes to be at the same fingers (see Figure 24).
3. The assumption of constant electrical and geometrical contact parameters is made.
4. The sheet resistance under the contact is assumed to remain constant during contact formation.

The latter assumption is not necessarily fulfilled for solar cells with screen-printed contacts by industrial pastes, because an emitter etching may occur during contact firing. The sheet resistance under the contact may change and the TLM method has to be adjusted. The derivation of the contact resistivity in this case is not possible in general. A separation of the contact resistivity and the sheet resistance under the contact may be possible [80] [84]. A changing sheet resistance under the contact is not considered in this chapter.

Below I will show the TLM evaluation on the example of a solar cell TLM test structure, as shown in Figure 25 (b). An example of a TLM measurement with a finger distance $d_F = 1.94 \text{ mm}$ is shown in Figure 26.

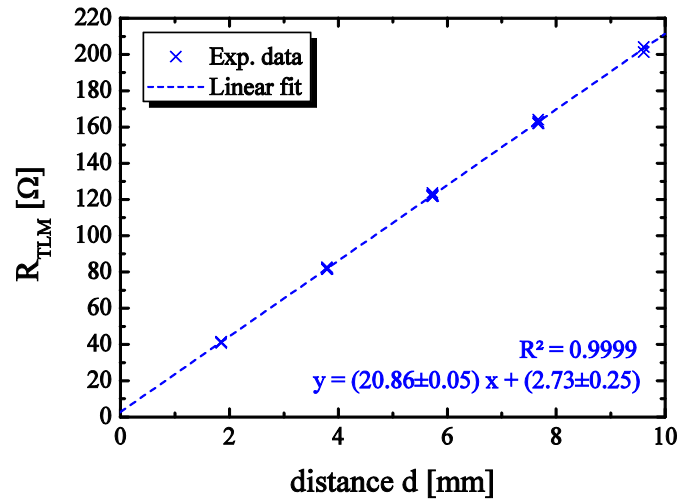


Figure 26: Example of a TLM measurement for a test structure as shown in Figure 25 (b). The results of a linear regression are shown in the lower right corner.

Carrying out the linear regression, i.e. applying Eq. (10), I derive $R_{C,TLM} = (1.37 \pm 0.13) \Omega$ and $\rho_{SH, homEm} = (208.6 \pm 0.5) \Omega/\square$. For a finger/contact width $w_C = 93 \mu\text{m}$, I determine $\rho_C = 7.46 \text{ m}\Omega\text{cm}^2$ applying Eq. (11) and $L_T = 59.8 \mu\text{m}$ applying Eq. (12).

3.1.3 TLM measurement on solar cells considering intermediate fingers

Unfortunately, the influence of the intermediate fingers between resistance measurements of not neighboring contacts is not considered in the previous section. Those fingers allow additionally a current flow through the contact into the metal at one side and back into the emitter at the other side of the contact. Thus the resistance beneath intermediate contacts is decreased compared to the resistance arising only from the emitter sheet resistance. An additional series resistance component below intermediate fingers R_{met} [85] is introduced into the series resistance network of the TLM measurement. This component depends on emitter sheet resistance beneath the contact and the contact resistivity. It is described by [85]

$$R_{met} = 2\rho_{SH,homEm} \frac{L_T}{l} \tanh\left(\frac{w_C}{2L_T}\right) . \quad (13)$$

Below I set up a new series resistance model depending on the number of fingers n_F involved in the measurement. E.g. four fingers involved in the measurement, mean probes at the first and the fourth fingers/contacts and $n_F = 4$. The model is described by

$$R_{TLM}(n_F) = 2R_C + (n_F - 1)R_{homEm} + (n_F - 2)R_{met} , \quad (14)$$

where the resistance contribution of the homogeneous emitter R_{homEm} changes from Eq. (10) to

$$R_{homEm} = \rho_{SH,homEm} \frac{d_F - w_C}{l} . \quad (15)$$

Note that the model is fitted by the least-square method to the experimental data. For a better understanding of the new TLM model, I carry out a parameter study for input values close to the shown TLM measurement example, i.e. $w_C = 93 \mu\text{m}$, $\rho_{SH,homEm} = 210 \Omega/\square$. The behaviors of the resistances relevant for the contact, i.e. Eqs. (11),(13),(15), are shown in Figure 27, varying the contact resistivity from 0.1 to 20 $\text{m}\Omega\text{cm}^2$. Note that Eq. (15) is only considered beneath the contacts with the contact width w_C , i.e. $R_{homEm} = \rho_{SH,homEm} \frac{w_C}{l}$.

R_{met} saturates towards R_{homEm} for increasing ρ_C , i.e. contact resistivity limits the conduction paths through the finger. R_{met} is in the same order of magnitude as $R_{C,TLM}$, i.e. well worth considering. The difference of $R_{homEm} - R_{met}$ for each intermediate finger is now incorporated into the emitter sheet resistance within a measurement. This results in an increased sheet resistance.

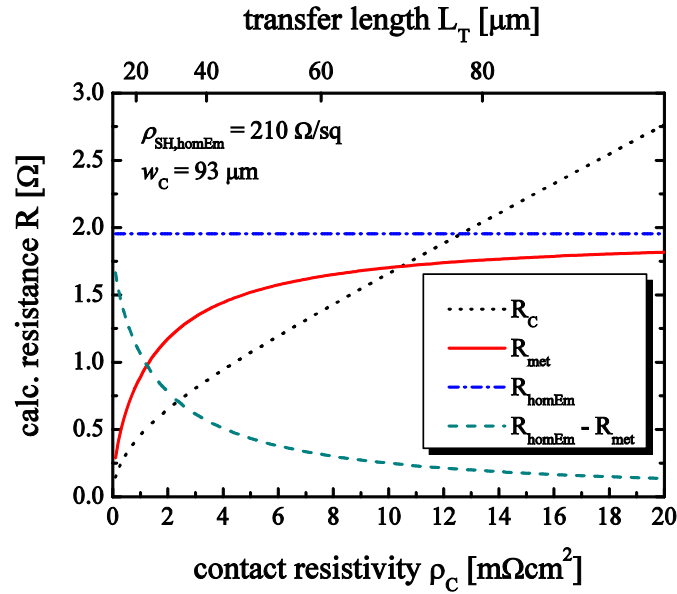


Figure 27: Comparison of the different resistances relevant for the contact in dependence of the contact resistivity ρ_C and L_T , respectively. The relation between ρ_C and L_T is described by Eq. (12).

The increased sheet resistance leads to a reduction in $R_{C,\text{TLM}} = R_{\text{TLM}}(d = 0 \text{ mm})$, i.e. decreased contact resistivity. Applying the model, given in Eq. (14), to the TLM measurement example, as shown in Figure 26, results in $R_{C,\text{TLM}} = 1.180 \text{ } \Omega$, $\rho_{\text{SH,homEm}} = 210.6 \text{ } \Omega/\square$, $\rho_C = 5.87 \text{ m}\Omega\text{cm}^2$ and $L_T = 52.8 \text{ } \mu\text{m}$. As expected, the emitter sheet resistance is slightly increased and the contact resistivity decreases considering intermediate contacts.

3.1.4 TLM measurements on solar cells with selective emitters

For the efficiency improvement of solar cells the concept of selective emitters (SE) is applied, i.e. the emitter is highly doped under the front metal contacts and rather lowly doped elsewhere (see Figure 24). The concept benefits from the decoupling of the emitter recombination properties from the contact resistance and contact recombination properties. The lowly doped emitter benefits from decreased recombination and the highly doped, selective emitter mitigates contact resistance. An option to fabricate a selective emitter is laser-doping [86] directly after the phosphorus diffusion from phosphor-silicate glass

(PSG) and before phosphorus glass removal (PGR). To obtain a laser-doped selective emitter, the phosphorus glass is heated by a laser, leading to additional local phosphorous diffusion with a selective emitter width w_{SE} which is typically wider than the contact width w_C (see Figure 24). For solar cells including a selective emitter the TLM model (Eq. (14)) needs to be adjusted for the TLM test structure shown in Figure 28.

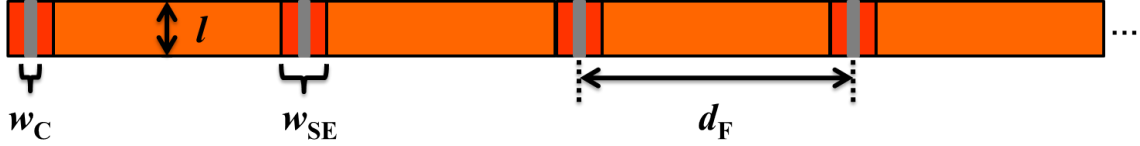


Figure 28: Schematic of a solar cell TLM test structure including a selective emitter beneath the contacts (dark orange) with the width w_{SE} which is wider than the contact width w_C .

The emitter resistance of a standard TLM test stripe (see Figure 25 (b)) is split for a selective emitter test stripe (Figure 28) into two resistances in series: the homogeneous emitter resistance and the selective emitter resistance. The selective emitter resistance R_{SE} (see red areas in Figure 28) is associated with (compare Eq. (10))

$$R_{SE} = \rho_{SH,SE} \frac{w_{SE} - w_C}{l} . \quad (16)$$

The homogeneous emitter resistance R_{homEm} changes from Eq. (15) to

$$R_{homEm} = \rho_{SH,homEm} \frac{d_F - w_{SE}}{l} . \quad (17)$$

Additionally, the contact resistance considers now the selective emitter sheet resistance $\rho_{SH,SE}$ and Eq. (11) is adjusted to

$$R_{C,TLM} = \rho_{SH,SE} \frac{L_T}{l} \coth\left(\frac{w_C}{L_T}\right) , \quad (18)$$

with

$$L_T = \sqrt{\frac{\rho_C}{\rho_{SH,SE}}} . \quad (19)$$

The series resistance driven voltage drop below intermediate fingers considers $\rho_{SH,SE}$ as well and Eq. (13) is adjusted to

$$R_{met} = 2\rho_{SH,SE} \frac{L_T}{l} \tanh\left(\frac{w_C}{2L_T}\right) . \quad (20)$$

The TLM model of Eq. (14) changes to

$$R_{TLM}(n_F) = 2R_C + (n_F - 1)(R_{homEm} + R_{SE}) + (n_F - 2)R_{met} , \quad (21)$$

considering a selective emitter. The model of Eq. (21) including a SE is applied to the example above mentioned by a least-square fit. I assume a contact width $w_C = 93 \mu\text{m}$ and a $\rho_{SH,SE} = 45.0 \Omega/\square$, which may be measured separately. I derive $R_{C,TLM} = 0.589 \Omega$ and $\rho_{SH,homEm} = 238.7 \Omega/\square$, $\rho_C = 4.25 \text{ m}\Omega\text{cm}^2$, and $L_T = 97.2 \mu\text{m}$. The shown example TLM measurement is derived from a passivated emitter and rear cell (PERC) [4] which has a selective emitter. To compare the results of the standard TLM evaluation with the improved TLM evaluation for selective emitters see Table VIII.

Table VIII: Comparison of the results of the TLM evaluation using three different models.

Case	Eq.	d_F [mm]	w_C [μm]	$\rho_{SH,SE}$ [Ω/\square]	$\rho_{SH,homEm}$ [Ω/\square]	R_C [Ω]	ρ_c [$\text{m}\Omega\text{cm}^2$]	L_T [%]
1	(10)	1.94	93	—	208.6	1.364	7.46	59.8
2	(14)	1.94	93	—	210.6	1.180	5.87	52.8
3	(21)	1.94	93	45	238.7	0.589	4.25	97.2
Rel. deviation between cases 1 & 3					14.4 %	-56.8 %	-43.0 %	62.5 %

The derived homogeneous emitter sheet resistance deviates about 14 % and the contact resistivity about -43 % comparing cases 1 and 3. The improved TLM evaluation scheme is recommended when evaluating solar cell TLM stripes with selective emitters.

Unfortunately, the selective emitter width w_{SE} and the selective emitter sheet resistance $\rho_{SH,SE}$ has to be determined separately. The selective emitter width w_{SE} may be concluded from the laser parameters or laser test structures, respectively. The selective emitter sheet resistance $\rho_{SH,SE}$ may be derived by four-point probe (4pp) measurements of the selective emitter created by laser stripes which are placed very close to each other. To partly overcome this disadvantage, I will present a test structure in the next section where both homogeneous and selective emitter sheet resistance may be derived at the same time.

For a better understanding of the series resistance model including a selective emitter (Eq. (21)), I calculate three measurements of the TLM resistance R_{TLM} where the first and the third contacts are probed with the current probes. The calculated resistance in dependence of the distance d is derived if the voltage could be probed at any distance d . The calculated resistances for the three cases are shown in Figure 29: (1) TLM series resistance network without selective emitter and intermediate finger resistance (Eqs. (10),(11),(12)), (2) TLM series resistance network with intermediate finger resistance, but without selective emitter (Eqs. (14),(11),(12),(15),(13)), and (3) TLM series resistance network with selective emitter and intermediate finger resistance (Eqs. (21),(16),(17),(18),(19),(20)).

For the calculation, the parameters of Table VIII are used. Comparing cases (1) and (2), one may conclude that the difference between both models is comparatively small. But I would like to note that only the comparatively high contact resistivity masks the effect of the intermediate finger (see Figure 27 where for high ρ_C , R_{met} saturates towards R_{homEm}). Comparing cases (1) and (3), the influence of the selective emitter sheet resistance next to the contacts leads to a weaker increase of the calculated resistance R and to a stronger increase in the range of the homogeneous emitter. It explains the derived values shown in Table VIII.

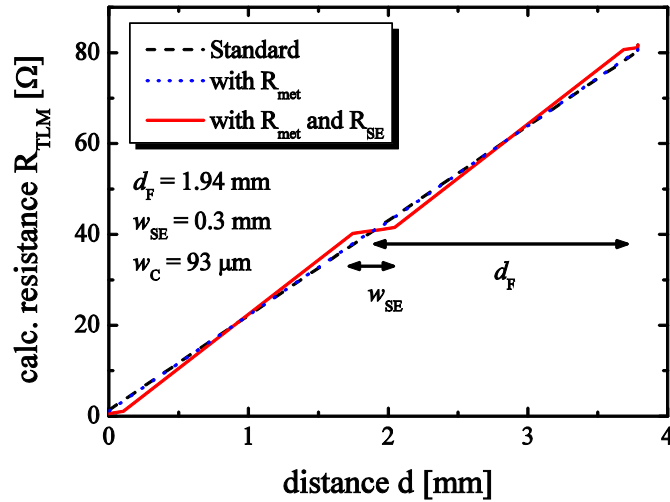


Figure 29: Comparison of the different TLM series resistance networks. The Standard TLM model is without the influence of the intermediate finger and without the selective emitter (Eq. (10)), the model ‘with R_{met} ’ includes the influence of the intermediate finger (Eq. (14)), and the model ‘with R_{met} and R_{SE} ’ includes both the influence of the intermediate finger and the selective emitter (Eq. (21)).

3.1.5 TLM structure separating homogeneous and selective emitter sheet resistance

The idea to separate homogeneous and selective emitter sheet resistance is to use the 2nd dimension of the width of the ‘stripe’. I propose to vary the stripe width within either just the homogeneous emitter area or the selective emitter area. The proposed TLM test structure is shown in Figure 30, which I call ‘dragon stripe’. It could be fabricated by laser cutting and mechanical breaking.

The variation of the stripe width is made only in the homogeneous emitter parts (orange). Thus the separation of homogeneous and selective emitter sheet resistance is now possible. For that a new model of the TLM series resistance network is built. The homogeneous emitter resistance R_{homEm} depends now on the stripe width l_i , i.e. the stripe width l_0 and the altitude of the added triangles.

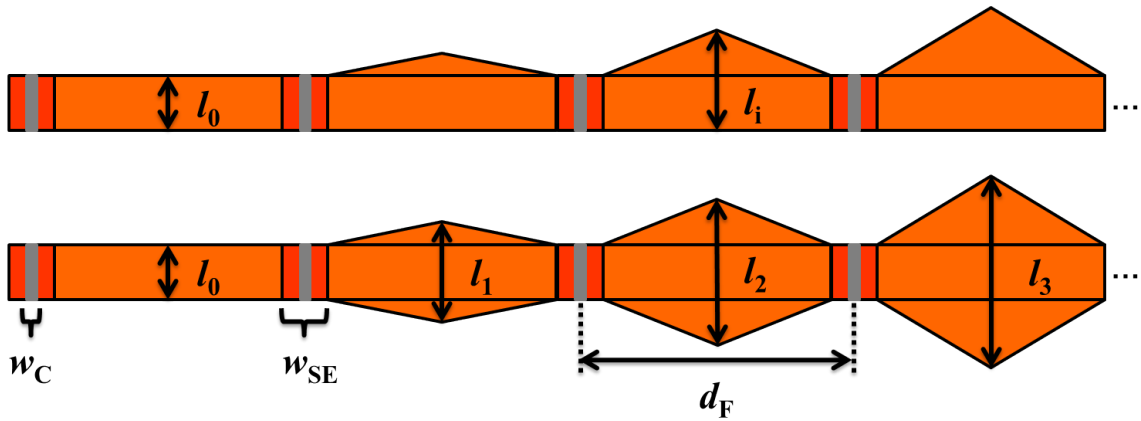


Figure 30: The solar cell TLM stripe with selective emitter (see Figure 28) is extended by triangles on one or both sides with increasing altitude.

R_{homEm} is derived solving the following problem assuming a constant current density at any distance d within the test structure:

$$dR = \rho_{SH} \frac{dx}{l(x)}, \quad (22)$$

where $l(x)$ is defined in Figure 31

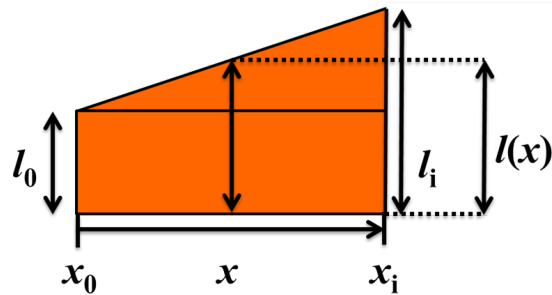


Figure 31: Schematic of a subsection of the solar cell TLM test structure as shown in Figure 30 for the resistance determination of the homogeneous diffusion $R_{\text{homEm},i}$. Note that x_i remains constant for constant contact distances.

and can be expressed by

$$l(x) = l_0 + \frac{(l_i - l_0)}{(x_i - x_0)} (x - x_0) \quad . \quad (23)$$

The resistance R in Eq. (22) can be obtained by solving the integral

$$\begin{aligned} \int_{x_0}^{x_i} dR = R_{0i} &= \rho_{SH, homEm} \int_{x_0}^{x_i} \frac{dx}{l(x)} = \rho_{SH} \int_{x_0}^{x_i} \frac{dx}{l_0 + \frac{(l_i - l_0)}{(x_i - x_0)} (x - x_0)} \\ &= \rho_{SH, homEm} \left[\frac{(x_i - x_0)}{(l_i - l_0)} \ln \left(l_0 + \frac{(l_i - l_0)}{(x_i - x_0)} (x - x_0) \right) \right]_{x_0}^{x_i} \\ &= \rho_{SH, homEm} \frac{\ln \left(\frac{l_i}{l_0} \right)}{(l_i - l_0)} (x_i - x_0) \quad . \quad (24) \end{aligned}$$

R_{homEm} is now

$$\begin{aligned} R_{homEm, i} = 2R_{0i} &= 2\rho_{SH, homEm} \frac{\ln \left(\frac{l_i}{l_0} \right)}{(l_i - l_0)} \left(\frac{d_F - w_{SE}}{2} \right) \\ &= \rho_{SH, homEm} \frac{\ln \left(\frac{l_i}{l_0} \right)}{(l_i - l_0)} (d_F - w_{SE}) \quad . \quad (25) \end{aligned}$$

For a better understanding of the impact of Eq. (25), it is compared with Eq. (17) in Figure

32 while $l_0 = 1$ cm, i.e. $R_{homEm}(l)/R_{homEm}(l_0) = \frac{\ln \left(\frac{l}{l_0} \right)}{(l - l_0)} l_0$.

For a TLM ‘dragon stripe’ in the section with maximum altitude, i.e. $l_i = 2$ cm ($l_0 = 1$ cm), a decrease in the resistance of the now wider homogeneous emitter resistance to 69 % is observed.

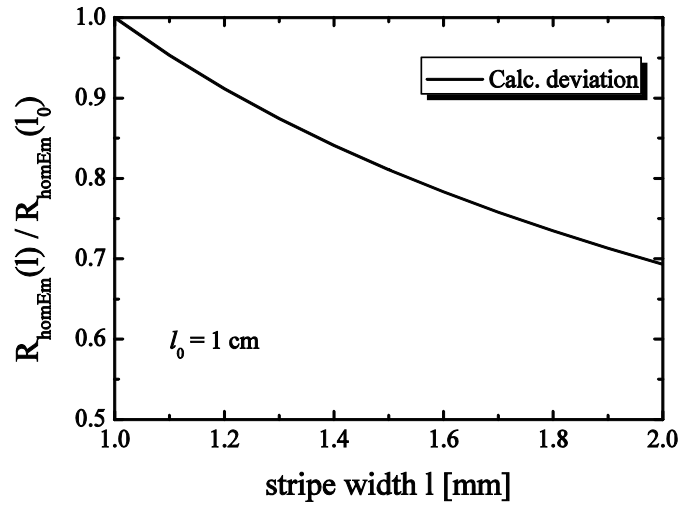


Figure 32: Comparison of the resistance of the homogeneous diffusion for a standard stripe ($l_0 = 1$ cm) and a ‘dragon stripe’ TLM test structure with increasing altitude of the triangles, where Eqs. (25) and (17) are applied.

The TLM series resistance network is described by

$$R_{TLM}(n_F) = 2R_C + (n_F - 1)R_{SE} + \sum_{i=1}^{n_F-1} R_{\text{homEm},i} + (n_F - 2)R_{\text{met}} \quad (26)$$

Note that the Eq. (26) needs the first contact to be always probed, but Eq. (26) could be adapted for all possible contact probe combinations. The model would be fitted again by the least-square method. The comparison between a calculated TLM measurement of the stripe test structure and the ‘dragon stripe’ test structure with $l_0 = 1$ cm and $l(d = 10 \text{ mm}) = 1.2$ cm is shown in Figure 33, whereas Eq. (21) and Eq. (26) are applied respectively.

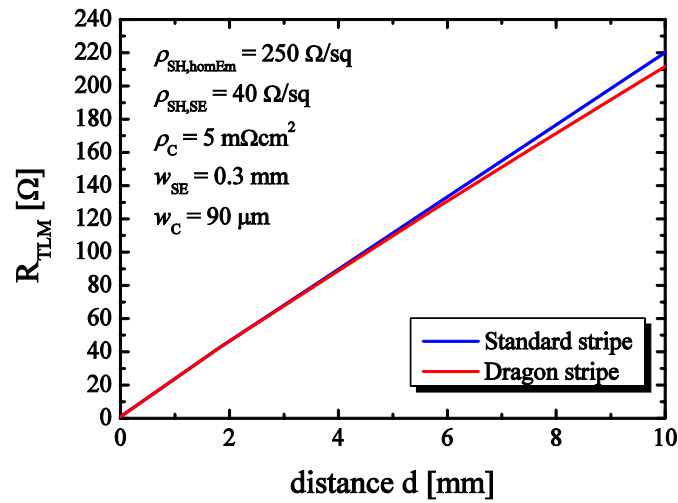


Figure 33: Comparison of calculated TLM measurements of a standard and ‘dragon’ stripe test structure for input parameters similar to the previously used example. The stripe width l is $l = 1 \text{ cm}$ for the standard test structure and varied from $l_0 = 1 \text{ cm}$ to $l(d = 10 \text{ mm}) = 1.2 \text{ cm}$ for the ‘dragon stripe’.

The highest deviations occur, as expected, for the section of the stripes with the highest stripe width l_i . Note that the linearity is no longer a measure for the quality of the measurement.

The main benefit of the ‘dragon stripe’ TLM test structure is the applicability to fabricated solar cells as the shape could be cut out of it, deriving ρ_C , $\rho_{SH,homEm}$ and $\rho_{SH,SE}$ with one single TLM measurement.

3.1.6 Conclusion

For solar cell TLM test structures, the consideration of the influence of intermediate, not contacted fingers is favorable. Especially it is recommended if the contact width is wide, the emitter sheet resistance beneath the contact is high and the contact resistivity is low. For solar cell TLM test structures with a selective emitter, the standard TLM evaluation is not sufficient. It shows deviations of about 14 % lower emitter sheet resistance and about 43 % higher contact resistivity in a typical example. An improved model which accounts for the sheet resistance of the selective emitter is presented, but the sheet resistance and the width of the selective emitter have to be known or to be determined separately. This disadvantage may be partly overcome by a new design of the TLM test structure, called 'dragon stripe', where the corresponding TLM model is presented. It allows the separation of the sheet resistance of the homogeneous emitter and the selective emitter, and the contact resistivity during a TLM measurement. The 'dragon stripe' test structure could be cut out of fabricated solar cells.

3.2 Method for imaging the emitter saturation current density with lateral resolution

3.2.1 Introduction

For the electrical characterization of silicon solar cells, it is very valuable to quantify the saturation current density of the emitter J_{0e} , or of other dopant-diffused regions. Presently, great effort is being put into the development of selective emitters for crystalline Si solar cells, meaning that the emitter is highly-doped at the front metal contacts and rather lowly doped elsewhere. So far, it has been possible to measure the J_{0e} of homogeneous samples only, most notably using the procedure of Kane and Swanson [22] in combination with the quasi-steady state photoconductance (QSSPC) method [48]. To determine the two J_{0e} -values associated with a selective emitter, it has therefore been necessary to fabricate two distinct homogeneous test samples: one sample rather lowly-doped, the other highly-doped. I developed an imaging method for measuring J_{0e} with lateral resolution, e.g. of inhomogeneous samples such as selective emitters. I use photoluminescence (PL) measurements combined with photoconductance measurements to derive calibrated images of the effective excess carrier lifetime. At least two images under two different high-injection conditions are taken. The J_{0e} image is then derived, applying the method of Kane and Swanson [22] for each pixel. Figure 34 shows a schematic of the measurement principle, which is similar to a simultaneously developed method proposed in Refs. [87] [88].

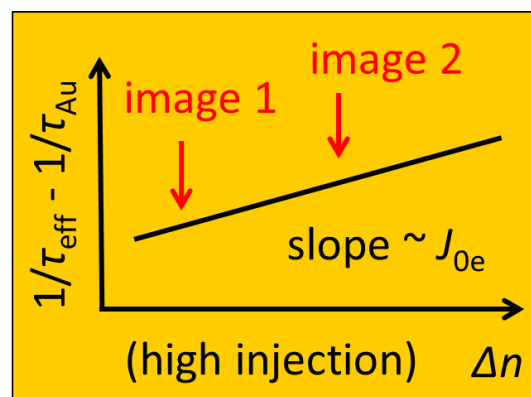


Figure 34: Measurement principle of the J_{0e} determination following the method of Kane and Swanson [22], applied for each pixel of at least two calibrated images of the effective excess carrier lifetime τ_{eff} .

As an application of the method, the J_{0e} dependence on laser-doping with different laser intensities is shown.

3.2.2 Experimental method

In the method of Kane and Swanson [22], the effective lifetime of excess carriers τ_{eff} is measured as a function of the injection density Δn on a lightly doped wafer (see Figure 34). A sample contains the highly-doped region on one surface at least (but optimally on both surfaces, to avoid any uncertainties in the recombination on the non-diffused surface). The wafer is optimally [89] [90] in high-level injection conditions because the recombination rate in the emitter is proportional to the square of Δn , and this recombination rate can then be separated from the linear recombination rate in the wafer (and from its other surface, if there is no highly-doped region). The inverse τ_{eff} can be expressed as [22]:

$$\frac{1}{\tau_{\text{eff}}} - \frac{1}{\tau_{\text{Au}}} = \frac{1}{\tau_{\text{SRH}}} + (J_{0e(\text{front})} + J_{0e(\text{rear})}) \frac{(N_{\text{dop}} + \Delta n)}{qn_i^2 W} \quad (27)$$

where N_{dop} is the wafer doping density, q is the elementary charge, W is the wafer thickness, and n_i is the intrinsic carrier density. The Auger lifetime τ_{Au} of the wafer needs to be accounted for only if the wafer is so highly injected that Auger recombination contributes significantly to its total recombination rate (this occurs often at $\Delta n > 2 \times 10^{16} \text{ cm}^{-3}$). τ_{Au} may be calculated from [91]. It is not necessary to know the Shockley-Read-Hall lifetime τ_{SRH} as long as it is not strongly injection-dependent, because to determine J_{0e} only the slope of $(1/\tau_{\text{eff}} - 1/\tau_{\text{Au}})$ versus Δn is of interest. Luckily, this slope is practically insensitive to the sample temperature, so no temperature stabilization is necessary during the measurements. However, a value for n_i needs to be decided for when converting the measured slope to J_{0e} , and this value should be stated when publicizing J_{0e} measurements. I use $n_i = 8.31 \times 10^9 \text{ cm}^{-3}$ according to Ref. [92], referring to 25°C, which is the reference temperature of the Standard Test Conditions (STC). Another possibility is to refer to 300

K, where n_i is $9.65 \times 10^9 \text{ cm}^{-3}$ [93], which is a standard for device simulation. The choice of n_i is not an issue as long as it is stated, because any J_{0e} value may be referred to another $n_{i,2}$ by using $J_{0e,2} = J_{0e} (n_i / n_{i,2})^2$.

The lateral determination of J_{0e} is based on photoconductance calibrated PL lifetime images, where two evaluation schemes to derive τ_{eff} are used: firstly [94] [95] [96] and secondly [97] [98]. PL images show the radiative recombination rate R_{rad} of the sample under illumination, i.e. the PL intensity I_{PL} can be expressed in general [98] by

$$I_{\text{PL}} \propto R_{\text{rad}} = B_{\text{rad}}(\Delta n)np \approx B_{\text{rad}}(\Delta n)\Delta n(N_{\text{dop}} + \Delta n), \quad (28)$$

where $B_{\text{rad}}(\Delta n)$ is the radiative recombination coefficient, which is injection-dependent [43]. The first scheme assumes [96]

$$I_{\text{PL}} = C_{\text{cal}} \cdot B(\Delta n) \cdot \Delta n \cdot (N_{\text{dop}} + \Delta n), \quad (29)$$

where C_{cal} is a calibration constant. The second method assumes a calibration function $I_{\text{PL}}(a,C)$ [98]

$$I_{\text{PL}}(\Delta n) = a\Delta n + C\Delta n^2, \quad (30)$$

which has to be found, where a and C are calibration constants. C_{cal} or a and C are derived by comparing the area averaged PL intensity with the QSSPC signal over the coil at the same injection level, for one or several Δn values, respectively. For calibration, a homogeneous part of the sample is used in order to reduce the uncertainty. The PL image is converted using Eqs. (29) or (30) to an image of Δn , and τ_{eff} is then derived from

$$\tau_{eff} = \frac{\Delta n}{G}, \quad (31)$$

where G is the average carrier-generation rate per volume. Under high injection conditions in the base, the PL signal is dominated by its quadratic dependence on Δn .

A J_{0e} image can be calculated using Eq. (27) if at least two τ_{eff} images are taken under two distinct high-injection conditions: the inverse lifetimes at each pixel of at least two lifetime images are linearly fitted, and J_{0e} is calculated using the slope (formulated here in differential terms):

$$J_{0e}(x, y) = \frac{1}{2} q n_i^2 W \frac{d \left(\frac{1}{\tau_{eff}(x, y)} - \frac{1}{\tau_{Au}(x, y)} \right)}{d(\Delta n(x, y))}. \quad (32)$$

The factor $\frac{1}{2}$ is due to the symmetrical sample preparation, where two identical emitters are diffused at the front and rear surfaces of the sample. If only two lifetime images are used, Eq. (32) reduces to

$$J_{0e}(x, y) = \frac{q n_i^2 W}{2} \left[\frac{\left(\frac{1}{\tau_{eff}(x, y)} - \frac{1}{\tau_{Au}(x, y)} \right)_{high}}{\Delta n_{high}(x, y) - \Delta n_{low}(x, y)} - \frac{\left(\frac{1}{\tau_{eff}(x, y)} - \frac{1}{\tau_{Au}(x, y)} \right)_{low}}{\Delta n_{high}(x, y) - \Delta n_{low}(x, y)} \right] \quad (33)$$

The uncertainty of the derived J_{0e} at each pixel depends on the uncertainties of τ_{eff} and Δn at each pixel, and may be calculated using the Gaussian propagation of uncertainty of Eq. (33). However, the uncertainty is significantly reduced because J_{0e} is not extracted at a single pixel from the image but as an average $\langle J_{0e} \rangle$ over an area of interest. Therefore, the random-error contribution $u(J_{0e})$ to $\langle J_{0e} \rangle$ is estimated using the standard deviation σ (assuming a normal distribution of the J_{0e} values within this area of interest).

As the Δn -calibration of the PL images is done with an area-averaged QSSPC signal, the uncertainty due to the QSSPC signal must also be considered. Experience shows that, in

homogeneous samples measured with QSSPC [48], $u(J_{0e})$ is about 10% of $\langle J_{0e} \rangle$ and is dominated by the uncertainty in W and G . It is shown below that, within the area of interest, σ is considerably smaller than 10%.

The calibrated lifetime images are derived using the LIS-R1 system from BT Imaging [99], which contains a Sinton Instruments photoconductance set-up [47]. The optics for the laser light allows for illumination levels of up to 10 suns. A schematic illustration of the set-up is shown in Figure 35.

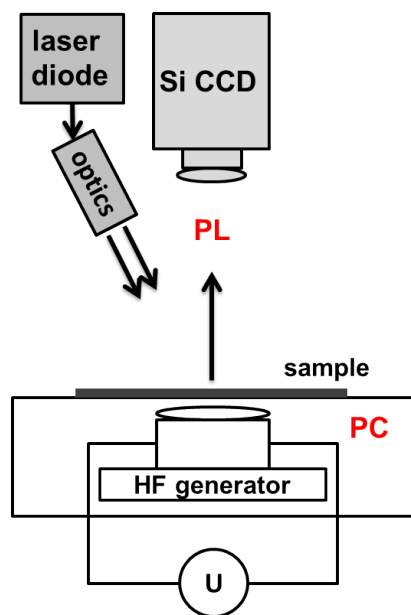


Figure 35: Schematic of the combined photoluminescence (PL) and photoconductance (PC) setup to derive calibrated lifetime images.

The optical reflectivity, required by the LIS-R1 system, is derived using a PerkinElmer UV/VIS spectrometer [100], while the wafer thickness is measured with a Käfer digital-dial gauge [101]. The emitter sheet resistance ρ_{SH} is measured after phosphorus glass removal (PGR) using a four-point probe (4pp) setup.

3.2.3 Example of an J_{0e} image derivation

The following example is shown to clarify the method. On the right side of the resulting J_{0e} image shown in Figure 36, rectangles due to different emitter formation are visible. Details of the content and artefacts are discussed later in Section 3.2.6.

For the determination, two PL intensity images under two different high-injection conditions are taken, which are shown in Figure 37. The PL images are calibrated by the QSSPC measurement and the excess carrier density images Δn are derived, applying Eqs. (29) or (30), which are shown in Figure 38. They are converted to calibrated images of the effective excess carrier lifetime τ_{eff} using Eq. (31), knowing the generation rate G , and are shown in Figure 39. An image of the emitter saturation current density J_{0e} is calculated from the two τ_{eff} and the two Δn images using Eq. (33), which is shown in Figure 36.

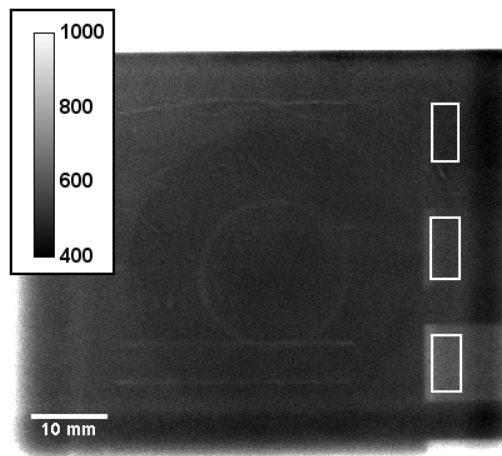


Figure 36: Example of a derived image of the emitter saturation current density J_{0e} [fA/cm^2].

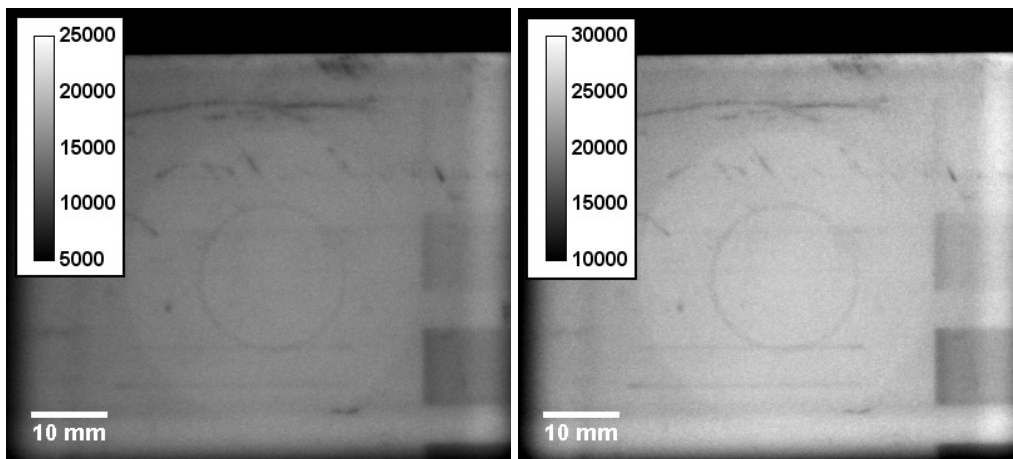


Figure 37: PL intensity images [a.u.] at 4 suns (left) and 8 suns (right) illumination.

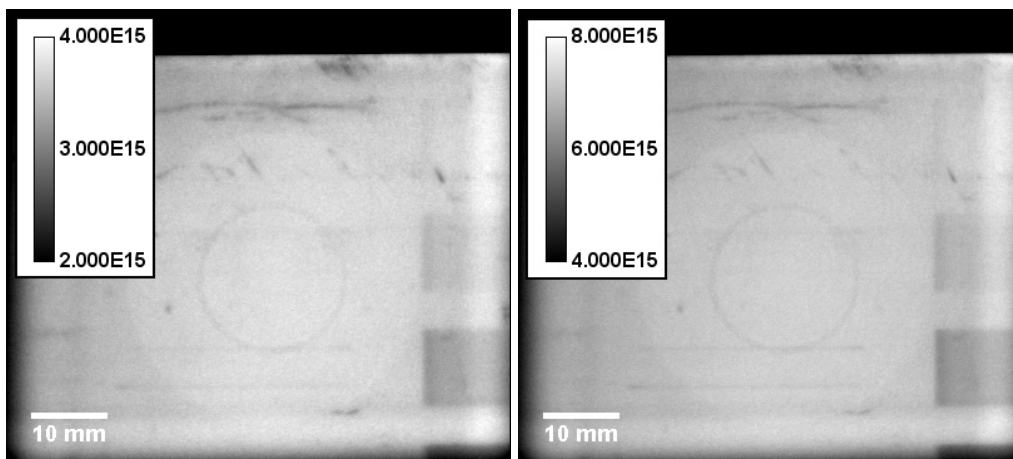


Figure 38: Excess carrier density images [cm^{-3}] at 4 suns (left) and 8 suns (right) illumination.

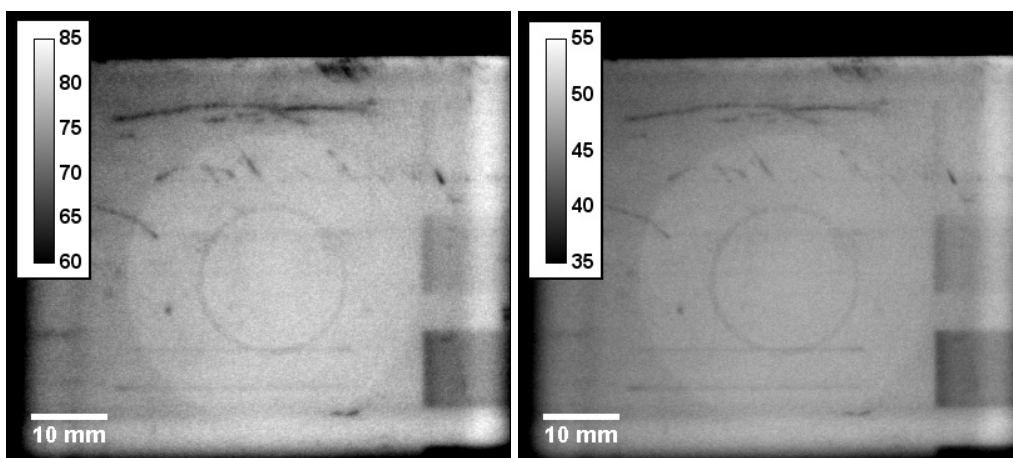


Figure 39: Calibrated images of the effective excess carrier lifetime [μs] at 4 suns (left) and 8 suns (right) illumination.

3.2.4 Simulation method

The lateral behavior of J_{0e} is analyzed by means of numerical device simulations in two dimensions. For this purpose, TCAD (Dessis) from Synopsys [39] is used to solve the fully coupled set of semiconductor equations, and the physical models and parameters described in Ref. [36] are applied. In device simulations, J_{0e} is not an input but a result from choosing a dopant profile, a surface recombination velocity S , and models such as Auger recombination, mobility etc. There are two main ways to extract J_{0e} from device simulations. One is to assume that all the current j that enters a dopant profile is caused to supply the recombination occurring within the dopant profile, i.e. j , p and n is probed at the base side of the space-charge region. Hence, there is

$$J_{0e} = \frac{j}{pn - n_i^2} n_i^2, \quad (34)$$

Please note that the local j is not accessible to experiment [102]. Thus a second simulation method is used, that reproduces Kane and Swansons's experiment [22], which means that the photo-generation density G is ramped while

$$\tau_{eff} = \frac{\Delta n}{R_{tot}} = \frac{\Delta n}{G} \quad (35)$$

is monitored, where the total recombination rate $R_{tot} = R_{SRH} + R_{Au} + R_{rad}$, i.e. the sum of all recombination included in the simulation. The lateral derivation of J_{0e} in the simulation is done by averaging all values over an array with widths of 50 μm . No optical simulation is carried out of rays according to the spatial distribution of R_{rad} . This implies that all rays are detected where they are generated.

3.2.5 Sample preparation

To determine J_{0e} , wafers which are diffused and passivated identically on both sides, have a high resistivity ρ and a high τ_{eff} , are used, so that high-injection condition can be achieved. I use saw-damage etched p-type 6" Cz material with a resistivity $\rho = 6 - 12 \Omega\text{cm}$. The wafers receive a HF-dip followed by POCl_3 diffusion for forming a homogeneous n^+ region. To obtain a laser-doped selective emitter (LD-SE), the phosphorus glass is heated by a laser, leading to additional local phosphorous diffusion and activation, and thus forming the n^{++} region. The processing is finished by applying phosphorus glass removal (PGR) and SiN deposition by PECVD on both sides of the wafers.

Two different test structures are produced, which are schematically shown in Figure 40.

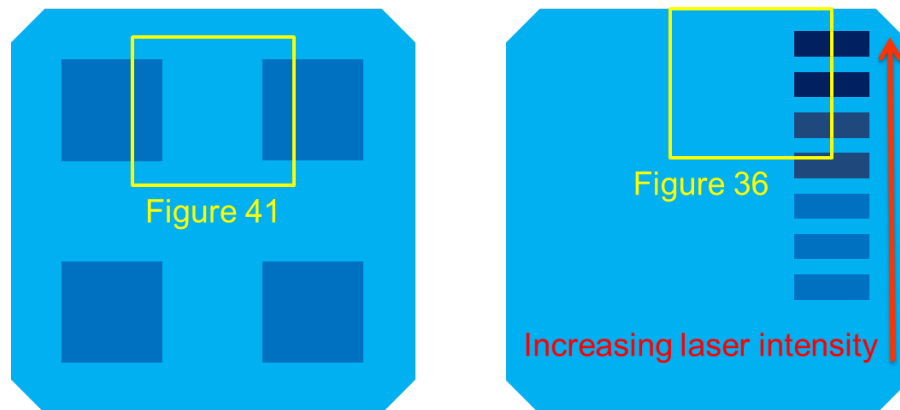


Figure 40: Test structures – left: symmetrical four square-shaped n^{++} regions with a size of 40 mm by 40 mm; and right: one-sided rectangular-shaped n^{++} regions with a size of 10 mm by 30 mm with different laser intensities.

The left structure has four square-shaped n^{++} regions with a size of 40 mm by 40 mm symmetrically on the front and back side. The size accounts for the possibility to calibrate on the n^{++} regions neglecting edge recombination effects [103]. The right structure investigates the J_{0e} dependence on the laser intensity for the laser-doping process. For that, rectangular-shaped n^{++} regions with a size of 10 mm by 30 mm are produced on one wafer with different laser intensities, but just on one side. The latter sample is investigated before

and after firing in a standard industrial belt furnace for screen printing. These structures are produced by laser-doping, where laser stripes are placed very close to each other, possibly with overlap due to positioning accuracy, causing double diffusions.

3.2.6 Validation and application of the method

To calculate experimental J_{0e} images, two calibrated lifetime images with a resolution of 403 pixels by 363 pixels are taken at approximately 4 and 8 suns. This corresponds to an injection level of about $4 \times 10^{15} \text{ cm}^{-3}$ and $8 \times 10^{15} \text{ cm}^{-3}$ in the n^+ region, denoted as “2” in Figure 41 (left).

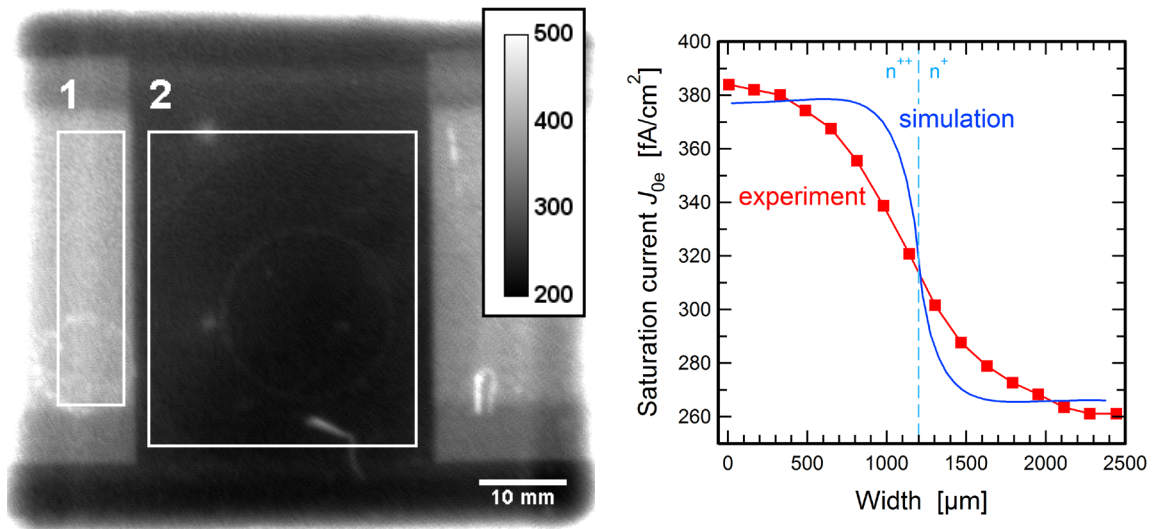


Figure 41: Left: Emitter saturation current density image where two selective emitter structures on the left and right side are visible (J_{0e} in fA/cm²). The round structures are artefacts. And right: Comparison of experimental (from area “1” to “2”) and simulated (τ_{eff} method) linescans of J_{0e} .

Also in Figure 41 (left), two small parts of square-shaped n^{++} structures with a size of 40 mm by 40 mm are partly visible on the left and right edges of the image as bright areas. In the area “2” of Figure 41 (left), an area-averaged J_{0e} of $238 \pm 15 \text{ fA/cm}^2$ is derived for the homogeneous n^+ emitter. For the area “1”, it is $419 \pm 19 \text{ fA/cm}^2$, which is the n^{++} region. The uncertainty is the standard deviation of the area-average and it is smaller than 10%, as discussed above. I deliberately made the n^{++} regions larger than the coil of the QSSPC in

order to directly compare a QSSPC measurement of a n^{++} region with the J_{0e} image. I observe a deviation in J_{0e} between the two measurement techniques that is smaller than 10% in relative terms.

Some artefacts are visible in Figure 36 and Figure 41 (left). The round structures in the center are due to the difference between the optical reflectivity of the QSSPC coil and the rest of the QSSPC stage. The brighter stripes at the edges of the images are due to effects in the optical system.

For validation of the derived J_{0e} image, I compare a linescan going from the area “1” to “2” in Figure 41 (left), with numerical simulations in Figure 41 (right). In experiment, a saturation of J_{0e} is achieved within 2 mm, while the simulation (τ_{eff} method) shows a saturation within 1mm under a generation rate of $G = 5 \times 10^{19} \text{ cm}^{-3}$ similar to the experiment. It is assumed that this is so because the detected rays are generated at various lateral positions due to different optical paths caused by reflection at the rear surface, sample stage and scattering at the front surface. The reason for the rather wide J_{0e} transition between the abrupt change from n^{++} to n^+ is mainly due to lateral currents in the base, causing a blurring of the electron and hole density n and p in the base, which is measured by PL. It is found that at G as high as $5 \times 10^{20} \text{ cm}^{-3}$, the simulations show a lateral resolution of about 0.5 mm for the abrupt transition from n^{++} to n^+ , which is due to the reduction of the diffusion length at higher injection levels.

By means of the J_{0e} imaging method, I analyze the J_{0e} dependence on laser-doping with different laser intensities. For that, J_{0e} of the rectangles of the second structure in Figure 40 (right) are determined with the described method on a single wafer as exemplified in Figure 36 for three rectangles. In Figure 42, the derived J_{0e} and the ρ_{SH} for each square is shown depending on the relative laser intensity before and after firing the sample in a belt furnace.

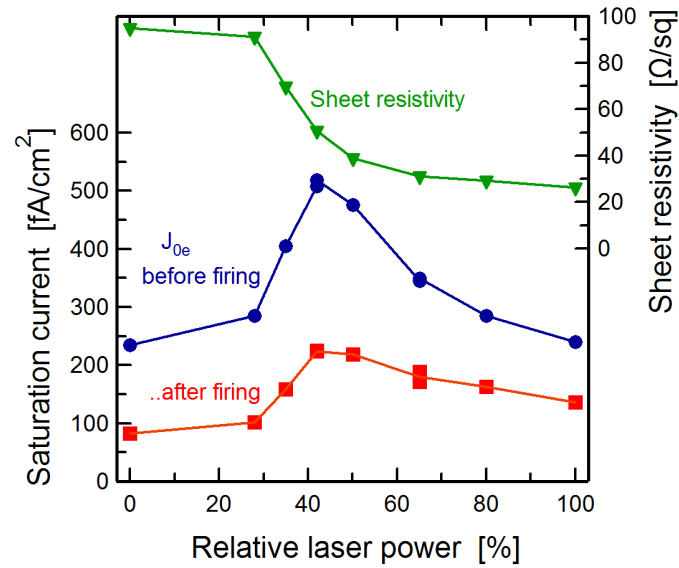


Figure 42: Measured dependence of J_{0e} and ρ_{SH} on the relative laser intensity of the laser-doping process. J_{0e} is shown before/after firing in a belt furnace.

For increasing laser intensities the J_{0e} first increases up to a relative laser intensity of 42% and then decreases, while the ρ_{SH} decreases from about 95 Ω/\square to 26 Ω/\square . Qualitatively similar results can be found in [104], which confirms the applicability of the method. Note that the benefit of the increased SiN passivation quality due to firing in the belt furnace is higher for the homogeneous emitter than for the laser-doped emitters with a high ρ_{SH} . E.g. the J_{0e} of the homogeneous emitter drops from 234 ± 14 fA/cm² to 83 ± 7 fA/cm², while J_{0e} of the selective emitter of $\rho_{SH} = 26$ Ω/\square drops from 240 ± 13 fA/cm² to 136 ± 6 fA/cm². The second structure is suitable for investigating the recombination activity of a laser-doped emitter, which can be used for the optimization of selective emitter solar cells. However, the influence of the metallization step is not considered, i.e. additionally introduced recombination and the contact resistance R_C of the contact formation are not taken account of.

3.2.7 Conclusion

A method is presented for measuring the emitter saturation current density J_{0e} with lateral resolution by using a combination of PL and QSSPC measurements. The method is successfully applied to selective emitters for crystalline Si solar cells. The measurement uncertainties due to the PL imaging are smaller than the uncertainties inferred from the QSSPC calibration. The method of imaging J_{0e} is investigated experimentally and by numerical simulations. By comparison, a limited resolution of a feature size of an inhomogeneous emitter is determined to be theoretically between 0.5 – 1.0 mm and experimentally about 2 mm. It is found that the reason for this is the lateral current in the base blurring the charge carrier densities n and p , which are experimentally observed by PL measurements. The successful application of the method used to investigate the influence of laser power to squared selective emitter structures shows that the ρ_{SH} decreases with increasing laser power, while the recombination activity of the emitter characterized by J_{0e} increases when increasing laser power from zero to a certain threshold level and then decreases as reported.

4. Determination of the rear side contact resistance of screen-printed PERC solar cells

4.1 Introduction

The passivated emitter and rear cell (PERC) [4] has been transferred from lab scale to mass production [105] and cell efficiencies exceed 20 % today [16]. This cell concept benefits strongly from improved optical properties and reduced recombination losses at the rear side. The local rear contacts may be produced by laser fired contacts (LFC) [106] or laser contact openings (LCO) [107] [108], i.e. local rear contacts are fabricated by laser processing and Al-sheet layer screen-printing. This produces an Al-Si alloy as rear local contact. During laser alloying (LFC) a local Al back surface field (BSF) is created [109], and during the high temperature firing step (LCO) silicon gets dissolved in the aluminum paste creating an Al-Si eutectic layer and an epitaxially grown BSF [29]. In this chapter, I exemplify my improved analysis for the determination of the local rear contact resistance on LCO line contacts (see Figure 43).

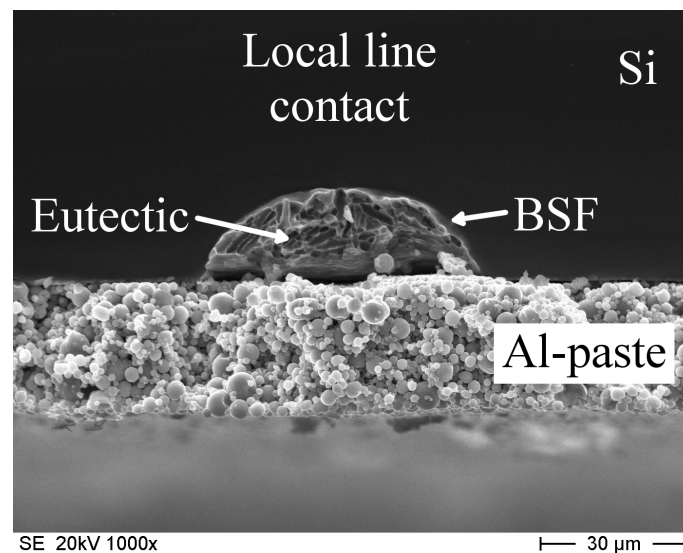


Figure 43: Scanning electron microscopy (SEM) image of the cross-section of a typical rear local line contact of a PERC solar cell where the contact forms an elliptically shaped Al-Si eutectic and a comparatively narrow local back surface field (BSF).

The determination of the rear contact resistance is an important parameter for further optimization of the cell concept. Especially, the route to lower the metallization fraction f_{met} is strongly affected by the contact resistance, which is one of the key optimization parameters, e.g. for producing segmented line contacts [110].

Typically series resistance losses at contacts are described by the specific contact resistance (contact resistivity) ρ_C in $\text{m}\Omega\text{cm}^2$, because then ρ_C only depends on material properties. Note that ρ_C is normalized to the contact area. However, ρ_C is difficult to derive for alloyed line contacts for two reasons. Firstly, the contact area is difficult to determine, even though it may be approximated by the circumference of an ellipse. Secondly, the BSF is difficult to describe in regards to depth and doping density (compare Figure 43 for the geometrical uncertainties). However, geometry strongly influences a ρ_C determination, e.g. by the transfer length method [80] (TLM), as the BSF distributes the current very evenly. I therefore propose that the series resistance per rear contact, R_{Contact} in Ω , as the most relevant and reliable measure of contact resistance. In case of a line contact, the series resistance per rear contact has units of Ωcm and is denoted R_C , because there is one ‘infinite’ lateral contact dimension. Their relation is:

$$\rho_C = R_{\text{Contact}} A_{\text{Contact}} = R_C a \quad , \quad (36)$$

where A_{Contact} is the contact area, which has a lateral dimension of 1 cm by definition for a line contact and a contact width a .

Both R_C or R_{Contact} may be deduced from current-voltage characteristics (I-V-curves). However, the following two features need to be taken into account. Firstly, cell current is typically stated as current density $J(V)$ normalized to the area of 1 cm^2 , so one extracts a (weighted) lumped series resistance r_S in units of Ωcm^2 . Secondly, r_S accounts for all series resistance contributions of the various cell regions, such as emitter, base, and rear contacts. Because these regions are distributed over large areas, it is generally impossible to separate clearly between contributions from series or parallel connection, so r_S is defined by the power loss P_{loss} caused by the series-resistance-driven voltage drop in the region of

interest, which is $r_S = P_{\text{loss}}/J^2$. However, the separation of the series and parallel contributions may be achieved by dividing the distributed J into symmetry elements of the cell, which are obtained by the condition that no currents flow through their borders of the semiconductor material. Then, one is able to connect the symmetry elements strictly in parallel (they are ‘laid out like tiles’). This corresponds in effect to an area weighting. In the case of the weighted rear contact resistance contribution r_C , it means that the generated current restricted to the symmetry element of the contact, needs to be considered, hence I have:

$$R_{\text{Contact}} = \frac{r_C}{A_{SE}} = \frac{\rho_C}{A_{\text{Contact}}} , \quad (37)$$

and for line contacts:

$$R_C = \frac{r_C}{p} = \frac{\rho_C}{a} , \quad (38)$$

where A_{SE} is the area of the symmetry element, with $A_{SE} = 1 \text{ cm} \times p$, and p is the distance between two rear line contacts, called pitch. For planar contacts, the metallization fraction is $f_{\text{met}} = a/p$. Note that $\rho_C/A_{\text{Contact}}$ and ρ_C/a requires that the current density is constant over the contact, which is in general not fulfilled for PERC solar cells.

Also note that ρ_C and r_C have the same unit Ωcm^2 , but different meaning. An overview of the used series resistances and their description is shown in Table IX.

Recently, a specific contact resistance (contact resistivity) ρ_C of 8 – 16 $\text{m}\Omega\text{cm}^2$ was derived in Ref. [111] using the transfer length method [80] (TLM). The samples contained rear local line contacts fabricated by rear finger screen-printing. A much higher specific contact resistance ρ_C of 40 – 55 $\text{m}\Omega\text{cm}^2$ was reported in Ref. [112], derived from a series resistance analysis of PERC solar cells with varying f_{met} . These two ranges of values for ρ_C differ more significantly than is expected.

Table IX: Overview of the series resistances used in chapter 4.

Parameter name	Symbol	Unit	Description
Lumped series resistance	r_S	Ωcm^2	Accounts for all series resistance contributions of the various regions of a solar cell
	$r_{S,DL}$	Ωcm^2	Measured by double light-level method
	$r_{S,TLL}$	Ωcm^2	Measured by triple light-level method
	$r_{S,nearBB}$	Ωcm^2	Measured by PL- R_S images, area averaged close to the busbars
	$r_{S,betweenBB}$	Ωcm^2	Measured by PL- R_S images, area averaged between the busbars
Weighted series resistance component	$r_{S,const}$	Ωcm^2	Contribution to r_S of the front busbars, front fingers, front contacts, emitter and the rear Al-sheet
	$r_{S,base}$	Ωcm^2	Contribution to r_S of the base
	r_C	Ωcm^2	Contribution to r_S of the rear contact
Rear (line) contact resistance	R_C	Ωcm	Absolute contact resistance per line contact
Specific rear contact resistance	ρ_c	$\text{m}\Omega\text{cm}^2$	Normalized to the contact area

Using Eq. (38), the weighted rear contact series resistance r_C has a value of $0.08 - 0.16 \Omega\text{cm}^2$ or $0.40 - 0.55 \Omega\text{cm}^2$, respectively, assuming a typical $f_{\text{met}} = 10 \%$; this corresponds to about 10% or 50% of the observed total, lumped series resistance r_S of a PERC solar cell. In this chapter, I will show that improved evaluation schemes of both proposed experiments explain and reduce the uncertainty of determining R_C significantly.

Looking at the rear local line contact geometry, shown in Figure 44, the contact resistance R_C is separated into four contributions: (1) the resistance of the Al-Si eutectic at the opening $R_{C,\text{opening}}$ with the width w_{opening} ; (2) the resistance of the elliptical shaped Al-Si eutectic layer $R_{C,\text{eutectic}}$ with the width a and the depth b ; (3) the Al-Si contact resistance $R_{C,\text{Al/Si}}$, where the half circumference of an ellipse $0.5 \times C \approx 0.5 \times \pi(2((a/2)^2 + b^2))^{1/2}$ is the contact cross-section, which may be associated with $f_{\text{met}} = C / (2 \times p)$; and (4) the resistance of the local BSF $R_{C,\text{BSF}}$ with depth w_{BSF} .

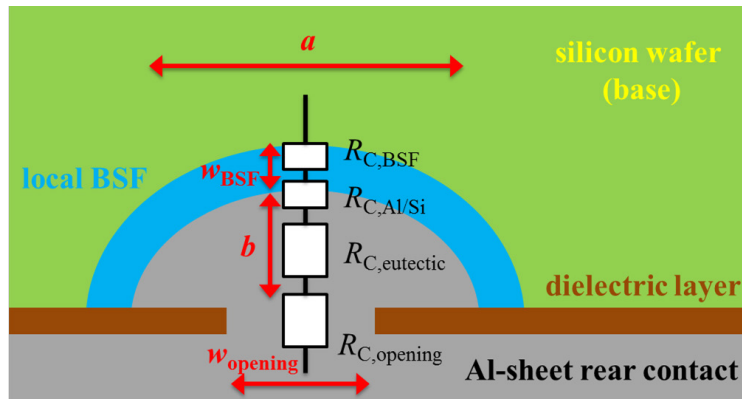


Figure 44: Schematic of the cross-section of the rear local line contact of a PERC solar cell. The rear contact resistance is thought to consist of four contributions: the Al-Si eutectic at the opening, the elliptical shaped Al-Si eutectic layer, the Al-Si contact resistance, and the local BSF.

Those resistance contributions may be summed in series to obtain the rear contact resistance R_C :

$$R_C = R_{C,opening} + R_{C,eutectic} + R_{C,Al/Si} + R_{C,BSF} \quad (39)$$

The contributions of $R_{C,opening}$ and $R_{C,eutectic}$ may become relevant if voids [113] are formed. $R_{C,BSF}$ can be neglected due to Al doping densities of typically higher than $1 \times 10^{18} \text{ cm}^{-3}$ within the shallow BSF. The contribution of $R_{C,Al/Si}$ is actually the resistance which is widely understood as the contact resistance. A separation of some of the contributions between void-affected contacts and non-voided contacts may be possible, but is not part of this chapter.

In this chapter, I show my results of a weighted series resistance analysis of PERC solar cells with varying f_{met} , while the weighted lumped series resistance r_S is derived by the triple-light-level method (TLL) [114] [115] from I-V-curves, and the weighted lumped series resistance is imaged and averaged by a PL technique [51]. The separation of the weighted series resistance components of the base $r_{S,base}$ and of the rear contact r_C from the weighted lumped series resistance r_S is carried out by

$$r_S(f_{met}) = r_{S,const} + r_{S,base}(f_{met}) + r_C(f_{met}) \quad , \quad (40)$$

where $r_{S,const}$ is the f_{met} -independent, weighted series resistance contribution of the front busbars, front fingers, front contacts, emitter and the rear Al-sheet. The analytical calculation of $r_{S,base}$ follows Gelmont et al. [116] and Saint-Cast [117]. Additionally, I quantify $r_{S,base}$ by numerical device simulations.

As a second method for the R_C derivation, the rear contacts of two PERC solar cells are investigated by TLM. In this chapter, I show that, for the evaluation of the TLM measurement, the perpendicular current flow above the rear contact must definitely be taken into account. I model the TLM setup by numerical device simulation to derive the lower limit of the series resistance contributions to the measured TLM resistance R_{TLM} considering additionally the contact geometry.

All improved evaluations lead to lower R_C than previously reported with a reduced uncertainty. The TLM method is suggested to be favorable.

4.2 Sample preparation

The $156 \times 156 \text{ mm}^2$ industrial PERC-type solar cells for this experiment are fabricated with a PERC process sequence [105] pseudo-square $180 \text{ }\mu\text{m}$ thick p-type boron doped Czochralski (Cz) silicon wafer material with a base resistivity variation ρ_{base} of $1 - 3 \text{ }\Omega\text{cm}$ in the *SolarWorld Innovations* pilot production line. The cells feature an alkaline texture, a lightly doped homogeneous and a heavily doped selective emitter. The local back contacting on the passivated rear side was achieved by laser processes and Al-sheet layer screen-printing. The contact line distance, called pitch p , is varied from 0.3 mm to 5.0 mm in 6 groups, i.e. $p = 0.3, 0.6, 1.0, 2.0, 3.0, 5.0 \text{ mm}$, so that the weighted series resistance contribution of the local rear contacts can be investigated. Each group started with 50 wafers. Furthermore, those groups are divided into five subgroups with varying firing peak

temperatures to ensure optimal contact firing conditions for each line pitch in the used conventional belt furnace. The optimal firing temperature for highest median efficiencies for each group is chosen for the evaluations, which is within a range of 30 K.

The solar cell base resistivity ρ_{base} is determined by capacitance-voltage (CV) measurements [118] with the pv-tools LOANA solar cell analysis system [119]. For the determination of the weighted lumped series resistance r_s of the PERC solar cells, current-voltage characteristics (I-V-curves) are measured in the dark and under three different illumination levels (0.8 suns, 1.0 sun and 1.2 suns) with a h.a.l.m. I-V-tester [120]. Additionally, PL- R_s images [51] are taken with the LIS-R1 BT Imaging tool [99].

The TLM sample preparation of these PERC solar cells requires a separation of the rear side line contacts, which can be done by rear finger screen-print or by mechanical Al-sheet structuring after cell processing. The mechanical ablation of the Al-sheet is chosen. The TLM stripes are prepared by laser cutting and mechanical breaking.

4.3 Modeling

The PERC solar cells and TLM test structures are analyzed by numerical device simulation. The focus is on series resistance losses. For the numerical solution of the semiconductor differential equations in the drift-diffusion approach, I use the software TCAD Sentaurus Device [39] and state-of-the-art physical models described in Ref. [36] [61] [62].

The geometrically irreducible *standard domain* for the device simulation of the PERC cell is two-dimensional (2D), assuming front and rear contacts are in line shape. The PERC domain is as high as the cell thickness, and I choose its width to be half of the rear local contact distance, i.e. half pitch $p/2$. At first sight, this may contradict the emitter geometry, because the front metal finger distance is generally unequal to half pitch. However, I choose the front surface to be fully covered with a metal contact, and I adjust the contact recombination velocity to be so low that the measured [22] emitter saturation current J_{0e} is reproduced in the model [64] (by using a measured doping profile). In this way, I can

freely vary the pitch, irrespective of the front finger distance. This choice of the PERC domain causes a homogeneous electron current flow across the p-n junction into the front metal and therefore neglects the resistive losses in the emitter arising, in reality, due to lateral currents flowing towards the front contact fingers. These resistive losses are neglected in my evaluations, because I only compare differences of the determined series resistances arising from the base and rear contact series resistance. The Shockley-Read-Hall (SRH) recombination in the bulk is included with a single defect energy at midgap having equal SRH lifetime parameters for electrons and holes, $\tau_p = \tau_n$. The SRH surface recombination at the passivating dielectric layer at the rear is also included, again with a single defect energy at midgap and equal surface recombination parameters for electrons and holes, $S_{n,rear} = S_{p,rear}$. The rear contact has a shallow BSF, which I include in the model via a Gaussian BSF doping profile. The used device parameters are listed in Table X.

Table X. List of device input parameters for numerical simulations.

Parameter	Symbol	Value	Unit
Cell thickness	W	150	μm
Rear contact width	a	60	μm
Front contact resistivity	$\rho_{c,front}$	1×10^{-3}	Ωcm^2
Rear contact resistivity	ρ_c	1×10^{-6}	Ωcm^2
Base resistivity	ρ_{base}	2.0	Ωcm
Measured emitter doping profile:			
Peak doping density	$c(P)_{Peak}$	6×10^{20}	cm^{-3}
Junction depth		0.3	μm
Gaussian BSF doping profile:			
Peak doping density	$c(Al)_{Peak}$	3×10^{18}	cm^{-3}
Junction depth		0.3	μm
Lateral depth		0.3	μm
SRH recombination parameters:			
Bulk electron	τ_n	2×10^{-3}	s
Bulk hole	τ_p	2×10^{-3}	s
Surface electron	$S_{n,rear}$	25	cm/s
Surface hole	$S_{p,rear}$	25	cm/s

The domain for the rear side TLM structure is schematically shown in Figure 45. It contains similar rear side contacts, but the emitter is omitted and not contacted. The potential is applied to the two rear contacts and the pitch p is varied.

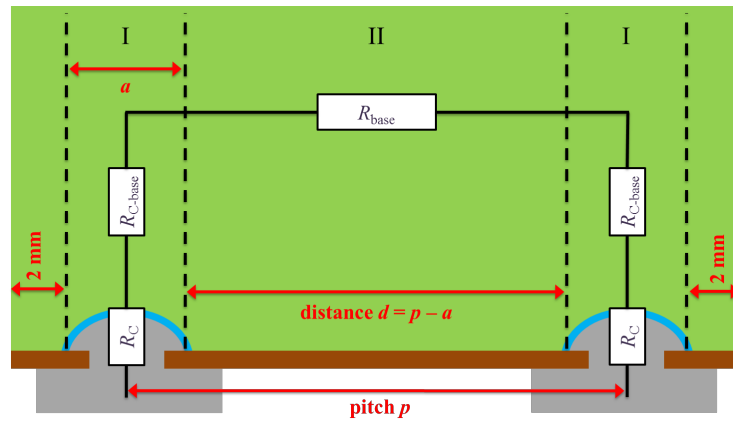


Figure 45: A schematic of the standard domain of a rear side TLM structure used for the simulations.

4.4 Derivation of the lumped series resistance

Four methods are used and compared for the determination of the (weighted) lumped series resistance r_S of the PERC solar cells. These are (1) the double light-level method [114] [121] applied to a dark and a 1 sun I-V-curve, (2) the triple light-level method [115] applied to the 0.8 suns, 1.0 sun and 1.2 suns I-V-curve, (3) and (4) the area averaged weighted series resistance of a PL- R_S image [51] close to and between the busbars, respectively. Figure 46 shows a PL- R_S image and exemplifies the regions which are analyzed within the images to determine the (weighted) lumped series resistance close to the busbars $r_{S,\text{nearBB}}$ and between the busbars $r_{S,\text{betweenBB}}$.

The derived lumped series resistance from a dark and a 1 sun I-V-curve $r_{S,\text{DL}}$ is a standard parameter of a h.a.l.m. I-V-tester and it is named ‘SserLfDfIEC’ in the software, which refers to a **light-forward** and a **dark-forward** I-V-curve evaluated by the double light-level method also described in the standard IEC 60891 [121]. The described method allows a voltage dependent $r_{S,\text{DL}}(V)$ determination, while I choose for my evaluations the voltage at MPP V_{MPP} which is most relevant for a solar cell. The (weighted) lumped series resistance from three different illuminated I-V-curves $r_{S,\text{TLL}}(V)$ is voltage dependent as well.

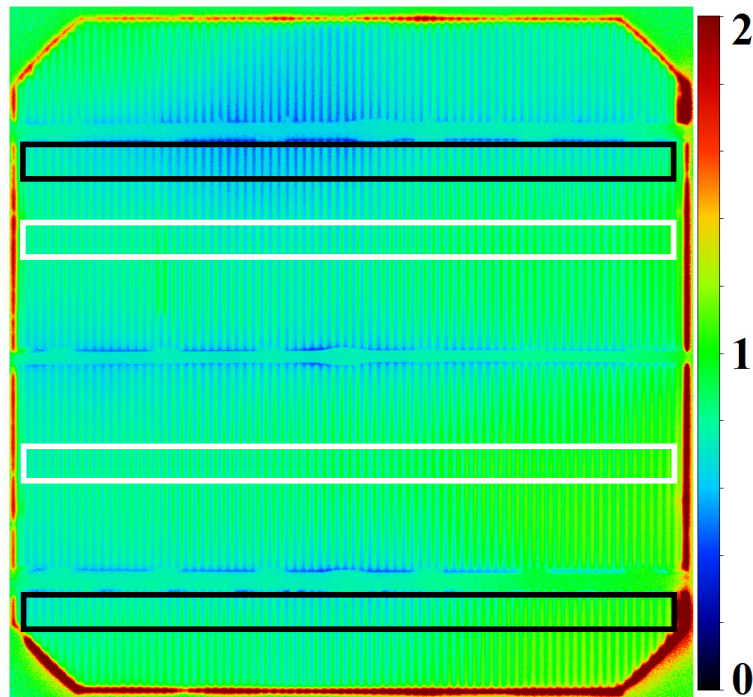


Figure 46: Example of a PL- R_s image [51] of a PERC solar cell where the lateral (weighted) lumped series resistance r_s in Ωcm^2 is shown. The regions close to the busbars and between the busbars are marked as black and white rectangles, respectively. For an introduction to the concept of (weighted) lumped series resistances r_s see chapter 4.1 and Table IX.

An example of $r_{s,\text{TLL}}(V)$ of a PERC solar cell with $p = 2$ mm is shown in Figure 47. Additionally, I plot the $r_{s,\text{TLL}}$ evaluation of numerically simulated I-V-curves of a PERC cell for plausibility. In the simulations, it is assumed that $r_{s,\text{TLL}}(V) = r_{s,\text{base}}(V)$ and a r_s offset of $0.5 \Omega\text{cm}^2$ is added to account for other resistance contributions, such as within the emitter or metallization. The experimental and simulated lumped series resistance decreases from MPP to open-circuit voltage V_{OC} . This originates from changes in the current-paths [122]. The wider the pitch the stronger the effect is. The deviations between experiment and simulation arise experimentally from the uncertainties of the I-V-curve measurements with the h.a.l.m. system and the simulations deviate due to the fact that the front side geometry of the simulation domain differs from the real PERC cell. Again, I choose MPP for the extraction of $r_{s,\text{TLL}}(V_{\text{MPP}})$.

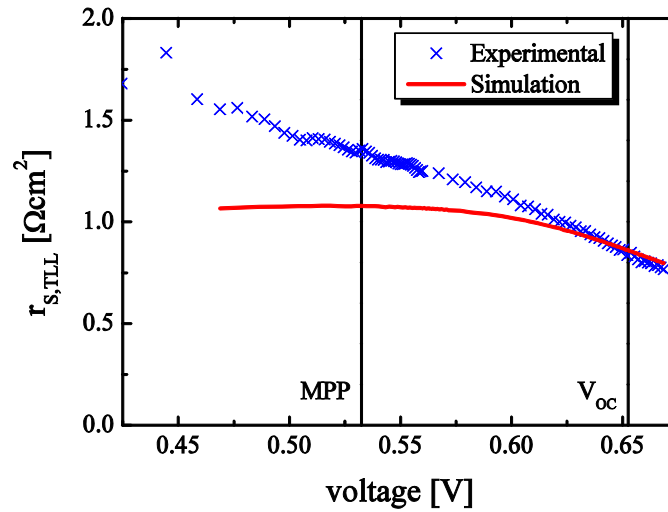


Figure 47: Example of voltage dependent (weighted) lumped series resistance $r_{S,TLL}(V)$ determined by the triple light-level method [115] (TLL) for a PERC solar cell with 2 mm pitch. The simulation is added for plausibility. Deviations between experiment and simulation arise experimentally from uncertainties of the r_S determination from I-V-curves and the simulations deviate due to the fact that the front side geometry of the simulation domain differs from the real PERC cell.

The four different (weighted) lumped series resistances $r_{S,DL}(V_{MPP})$, $r_{S,TLL}(V_{MPP})$, $r_{S,nearBB}$ and $r_{S,betweenBB}$ are determined for all PERC cells. The cell groups contain finally 6 – 15 cells. The box-plot in Figure 48 shows their comparison.

As expected, the weighted lumped series resistance r_S increases with increasing pitch of the PERC cells for all series resistance determination methods. In general, the variation of r_S is similar for all methods and can be tracked down for small pitch to an inhomogeneous front contact resistivity, due to the firing process, and for large pitch to the base resistivity variation. $r_{S,DL}(V_{MPP})$ is lower than $r_{S,TLL}(V_{MPP})$ for all pitch, but from analytical calculations (not shown here) I expect r_S values closer to $r_{S,TLL}(V_{MPP})$. The difference can be explained by the different solar cell operation conditions in the dark and under illumination. Again, those differences originate from the changes in the current paths [122]. $r_{S,nearBB}$ is lower than $r_{S,betweenBB}$ for all pitch. This is due to the fact that the current generated between the busbars flows along the fingers and suffers from finger resistance, whereas close to the busbars it almost does not. For high pitch, the PL- R_S imaging method shows a high noise and the fingers shade the signal significantly.

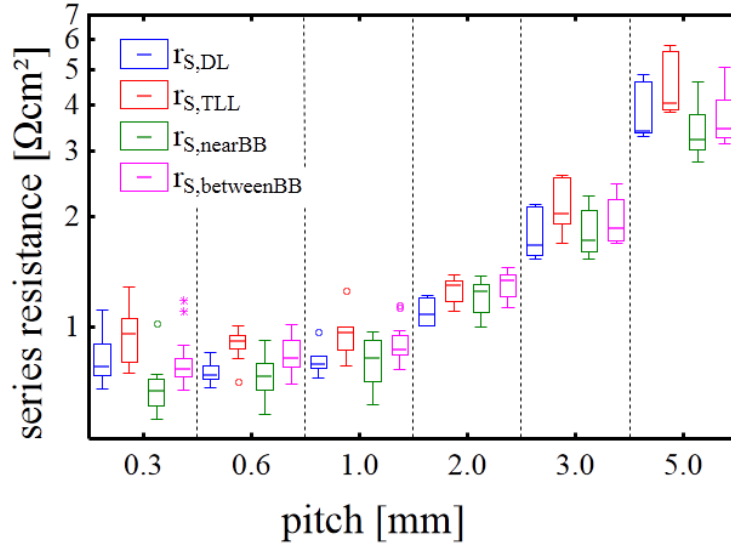


Figure 48: Box-plot of the (weighted) lumped series resistance measured with four different methods: $r_{S,DL}(V_{MPP})$ with the double light-level method applied to a dark and a 1 sun I-V-curve, $r_{S,TLL}(V_{MPP})$ with the triple light-level method applied to the 0.8, 1.0, and 1.2 suns I-V-curve, $r_{S,nearBB}$ and $r_{S,betweenBB}$ with the area averaged series resistance of PL- R_s images close to and between the busbars, respectively.

I therefore decide to use the weighted series resistance determined by the triple light-level method $r_{S,TLL}(V_{MPP})$ for our further analysis, i.e. in the following $r_S = r_{S,TLL}(V_{MPP})$.

4.5 Evaluation of the rear contact resistance R_C

4.5.1 Evaluation of R_C of PERC cells with varying metallization fraction

It is better to determine solar cell parameters such as the rear contact resistance R_C on finished solar cells rather than on test structures, if possible. The benefit of such determination is that the derived cell parameters are as close as possible to the real solar cell fabrication process.

For the determination of metallization fraction f_{met} -independent rear contact resistance R_C , I separate the f_{met} -dependent weighted series resistance of the base $r_{S,base}$ and the f_{met} -dependent weighted series resistance of the rear contact from the (weighted) lumped series resistance r_S (see Eqs. (40) and (38)). The weighted series resistance of the base

$r_{S,base}$ is calculated for varying f_{met} , i.e. p , following Eq. (41) of Gelmont et al. [116], which was adapted to solar cells by Plagwitz [123] [56],

$$r_{S,base}(\rho, W, p, a) = \frac{p\rho}{2\pi} \ln \left(\frac{2(\sqrt{\cosh(\pi a/4W)+1})}{\sqrt{\cosh(\pi a/4W)-1}} \right) + \rho W \left(1 - \exp(-W/p) \right) , \quad (41)$$

which applies if $\tanh(\pi a/4W) \leq 1/\sqrt{2}$, which is fulfilled for all investigated cases of this chapter. Secondly, $r_{S,base}$ is calculated by Eq. (42) of Saint-Cast [117] (pp. 56 – 61),

$$r_{S,base}(\rho, W, p, a) = \frac{a}{2} \rho \left(37f_{met} - 2 - \frac{0.3}{f_{met}} \right) + \frac{2.82(2W/a)^{0.88} f_{met}^{0.64}}{\tanh(2.82(2W/a)^{0.88} f_{met}^{0.64})} \frac{a^2 \rho}{12W} \left(\frac{1}{f_{met}} - 1 \right)^2 + W\rho . \quad (42)$$

The maximal error of Eq. (42) is smaller than 5 % in a range of $W/a \leq 30$ and $0.5 \% \leq f_{met} \leq 10$. The Eqs. (41) and (42) consider planar contacts, so that $f_{met} = a/p$. Additionally, I carry out device simulations of PERC cells with varying f_{met} , i.e. varying p , and extract the lumped series resistance by the triple-light-level method (TLL) [115] evaluated at maximum power point (MPP). For the simulations, the emitter resistance is neglected by inserting a the full-area front contact; R_C at the rear contacts is neglected by setting ρ_C to $1 \times 10^{-6} \Omega\text{cm}^2$ and by applying a shallow BSF. For all calculations and simulations, I assumed a wafer resistivity of $\rho_{base} = 2 \Omega\text{cm}$, a wafer thickness $W = 150 \mu\text{m}$ and a contact width $a = 60 \mu\text{m}$ of a planar contact geometry. A comparison of the determined $r_S = r_{S,base}$ is shown in Figure 49.

The calculation of $r_{S,base}$, following Gelmont et al., shows high deviations compared to Saint-Cast and the numerical simulation when the cell has a high pitch, which was found in Ref. [124] too. This is due to the assumption of Gelmont et al. that there is an equipotential at the base side of the space-charge region (SCR). Whereas Saint-Cast assumed that there is a laterally homogeneous minority carrier density and a laterally homogeneous net current at the base side of the space-charge region (SCR). From my simulations, it turns out that the assumptions of Saint-Cast are more relevant for illuminated solar cells, when comparing the results.

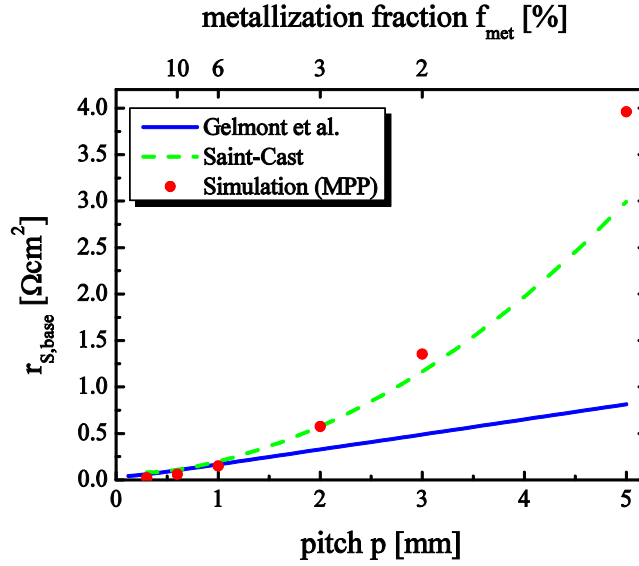


Figure 49: Comparison between the weighted series resistance of the base, determined by the method of Gelmont et al., Saint-Cast, and numerical simulations. A contact width of $60 \mu\text{m}$, a wafer thickness of $150 \mu\text{m}$, and $2 \Omega\text{cm}$ base resistivity are used for the calculations and the simulations.

The Eq. (41) by Gelmont et al., used in Ref. [112], underestimates the weighted series resistance contribution of the base $r_{S,base}$, which leads to an overestimation of r_C (see Eq. (40)). It results and explains the comparatively high, derived ρ_C of $40 - 55 \text{ m}\Omega\text{cm}^2$.

For the determination of the weighted lumped series resistance r_S , I choose the triple light-level method (TLL) applied to the 0.8 suns, 1.0 sun and 1.2 suns I-V-curve [115] for following evaluation. The TLL method allows a voltage dependent $r_S(V)$ determination, while I choose for my evaluations the voltage at MPP V_{MPP} which is most relevant for a solar cell. The determined (weighted) lumped series resistance $r_S = r_{S,TLL}(V_{MPP})$ derived by the TLL method is shown in Figure 50. As expected, the weighted lumped series resistance r_S increases with increasing pitch of the PERC cells. The variation of r_S can be tracked down for small pitch to an inhomogeneous front contact resistivity, due to the firing process, and for large pitch to the base resistivity variation.

For the derivation of the rear contact resistance R_C , I separate the f_{met} -dependent $r_{S,base}$ and $r_{S,const} = 0.5 \Omega\text{cm}^2$ from $r_S(V_{MPP})$ using Eq. (40).

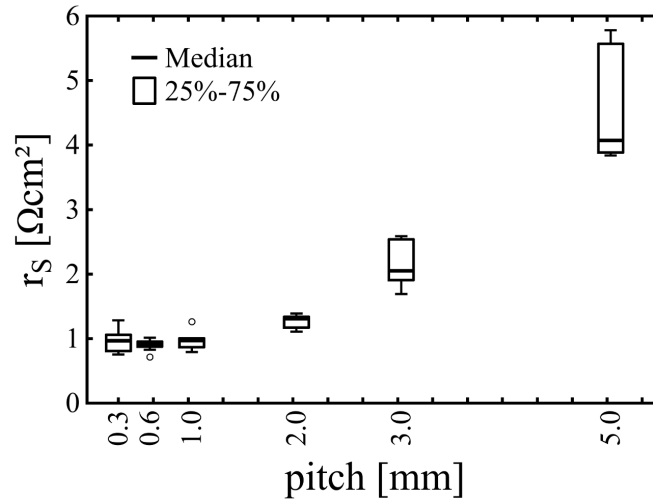


Figure 50: Box-plot (whiskers extend to the largest value within ± 1.5 interquartile range) of the (weighted) lumped series resistance $r_S(V_{MPP})$ measured with the triple light-level method [115] (TLL) applied to the 0.8, 1.0, and 1.2 suns I-V-curve.

Note that $r_{S,\text{base}}$ strongly depends on ρ_{base} , so ρ_{base} is measured with capacitance-voltage (CV) method [118] for each sample to reduce uncertainties and apply Eq. (42) (Saint-Cast) to derive $r_{S,\text{base}}$. Figure 51 shows the resulting weighted rear contact series resistance r_C in dependence of p .

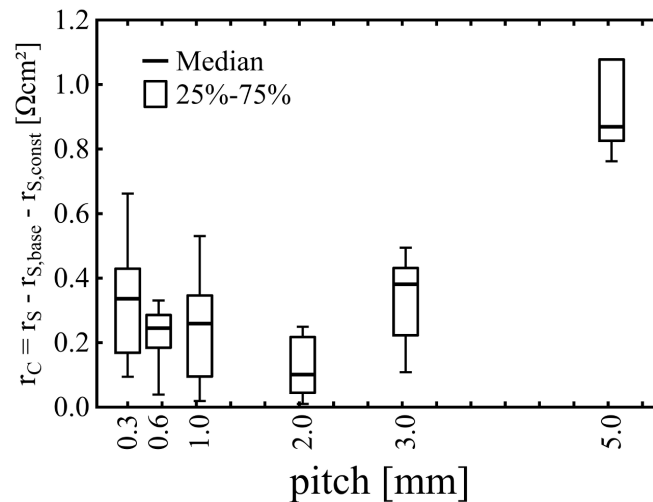


Figure 51: Box-plot (whiskers extend to the largest value within ± 1.5 interquartile range) of the weighted rear contact series resistance r_C after subtracting $r_{S,\text{base}}$ and $r_{S,\text{const}} = 0.5 \Omega\text{cm}^2$, using Eqs. (40) and (42). r_C still includes all variations of r_S occurring e.g. due to firing issues, process variations during emitter diffusion, etc.

The weighted rear contact series resistance r_C increases with increasing p . Only for high pitch, the influence of r_C may be dominant. For small pitch, variations of r_S are visible, which possibly occur due to firing issues, process variations during emitter diffusion, etc. I apply Eq. (38) to derive the rear contact resistance R_C per line contact which is theoretically constant after separating all f_{met} -dependent influences. R_C is shown in Figure 52.

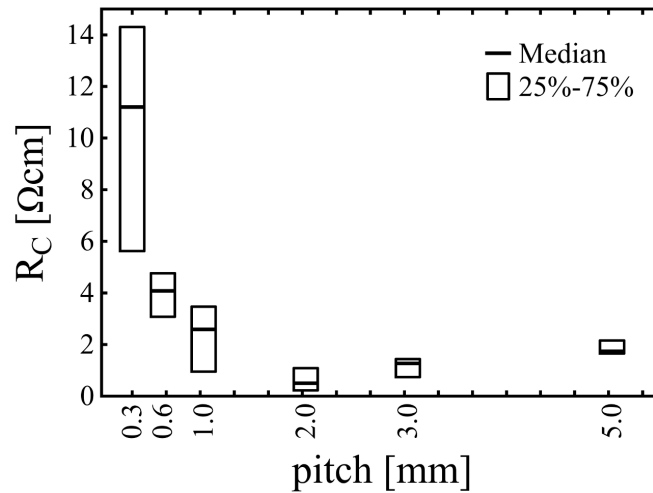


Figure 52: Box-plot of the rear contact resistance R_C per line contact. For small pitch, a high uncertainty is dominant, which is due to firing issues, process variations during emitter diffusion, etc. For high pitch, a maximal resistance per contact $R_C = 2 \Omega\text{cm}$ is determined.

I could not derive a constant R_C . For small pitch, the high r_C uncertainty results in a high R_C value with a high variation. In the pitch range from 2 mm to 5 mm, the rear contact resistance R_C is more accurate due to the lower metallization fractions. From the highest pitch of 5 mm, a maximal resistance per contact of $R_C = 2 \Omega\text{cm}$ is estimated.

Figure 52 includes all uncertainties for the evaluation method of the series resistance analysis of PERC solar cells with varying metallization fraction f_{met} . I summarize that uncertainties arise from: (1) the choice of the series resistance determination method which determines the overall r_S level, where I prefer TLL, (2) the voltage at which r_S is evaluated for double or triple light-level methods, (3) the r_S correction procedure while calculating $r_{S,\text{base}}$ which introduces uncertainties especially for a higher pitch, where I observe deviations between state-of-the-art analytical solutions and between numerical simulations,

and (4) the derived R_C value may be most accurate for a high pitch, but those PERC cells suffer from non-optimized production processes and extreme cell working conditions. Based on the experimental results and my evaluation, I do not recommend the evaluation method of the series resistance analysis of PERC solar cells with varying f_{met} .

4.5.2 Evaluation of R_C using the TLM method

The transfer length method (TLM) [80] is most successfully applied measuring the resistances of metal-semiconductor contacts placed on a thin conductive sheet layer. For an introduction to the transfer length method see Chapter 3.1. A typical example is the front contact fingers on the emitter layer of solar cells (see Section 3.1.2). At the rear of PERC cells, however, the contacts are placed directly on the base, so no conductive sheet layer is present, and the current flows during the measurement in a rather curved pattern between two contacts. The idea to separate the contact resistance $R_{C,\text{TLM}}$ from the sheet resistance ρ_{SH} by measuring the voltage drop between two contacts is to vary the contact distance d . The current is flowing through each contact and through the conductive sheet layer. The series resistance network describes Eq. (10). The TLM method is applied for the determination of the rear contact resistance R_C of PERC solar cells as proposed in Ref. [111]. Examples of a TLM measurement are shown in Figure 53.

For the derivation of the resistance R_C of the rear line contacts of PERC solar cells, the assumption of a very thin, of optimally zero thickness, conductive sheet layer is violated. The thickness W of typical solar cells is about 150 – 180 μm , i.e. the perpendicular current flow above the rear contacts has to be considered for the R_C derivation.

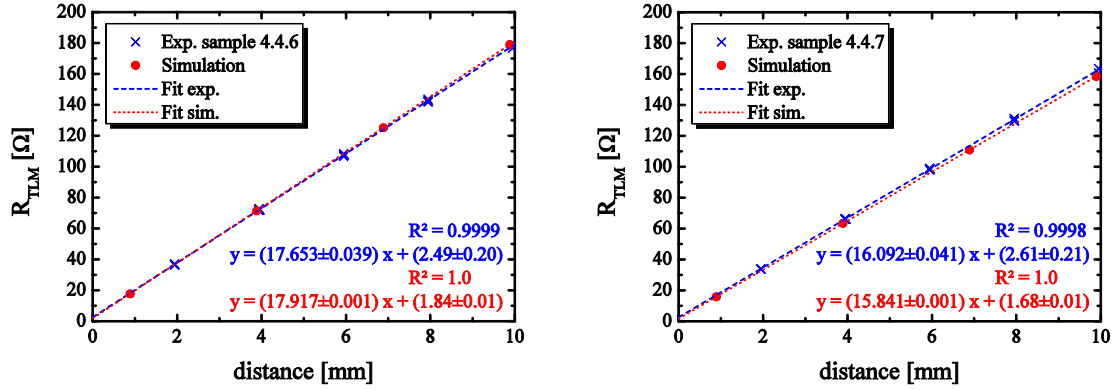


Figure 53: Two examples of a TLM measurement of a PERC solar cell with a pitch of 2mm (blue crosses), compared with numerical device simulations (red circles). The results of a linear regression are listed, applying Eq. (10).

The additional series resistance component R_{C-base} is exemplified in Figure 45 and should be considered when carrying out TLM measurement of the rear contact of PERC solar cells. An adapted series resistance network is described by

$$R_{TLM}(d) = 2 \left(\frac{R_C}{l} + R_{C-base} \right) + R_{base}(d) \quad (43)$$

Besides R_C per line contact, there is a kind of an ‘intrinsic’ R_C component R_{C-base} which cannot be separated by the TLM method, as it does not depend on d . R_{C-base} is a function of the base resistivity ρ_{base} , the base thickness W and the geometry of the contact, i.e. the penetration of the contact into the base (see Figure 43). For a maximum impact estimation of R_{C-base} , I may assume that the current flows only perpendicularly in the sections ‘I’ in the series resistance network of Figure 45, while the lateral current flow is only in the section ‘II’ and the current density is constant there. Assuming a planar contact, R_{C-base} may be estimated by

$$R_{C-base}(\rho_{base}, W, a) = \frac{1}{3} \frac{\rho_{base} \times W}{a \times 1cm} \quad (44)$$

while the prefactor $1/3$ accounts for the decreasing current density going away from the contact, which is a similar problem as the analytical determination of the series resistances of the emitter or finger [125], respectively. $R_{C\text{-base}}$ is $2\ \Omega$ assuming $\rho_{\text{base}} = 2\ \Omega\text{cm}$, $W = 150\ \mu\text{m}$ and $a = 50\ \mu\text{m}$.

This idealized model does not hold for the real case. A TLM evaluation method was recently proposed, considering a thick sample [126]. The second dimension of the thickness is accounted for in an analytical solution to derive $R_{C,\text{TLM2D}}$ for planar contacts. $R_{C,\text{TLM2D}} \approx R_{C\text{-base}}$ is $1.16\ \Omega$ assuming $\rho_{\text{base}} = 2\ \Omega\text{cm}$, $W = 150\ \mu\text{m}$, $a = 50\ \mu\text{m}$ and $\rho_C = 1 \times 10^{-3}\ \text{m}\Omega\text{cm}^2$.

I propose to determine $R_{C\text{-base}}$ by numerical device simulation to account for inhomogeneous current densities in the base, current crowding close to contacts/BSF and additionally to Ref. [126], the elliptical contact geometry. For two PERC solar cells with a pitch of $2\ \text{mm}$ from the same experiment as discussed before, TLM measurements and device simulations are carried out. The full-area rear Al-sheet contact is structured in lines by mechanical ablation. The results of the measurements are shown for the samples 4.4.6 and 4.4.7 in Figure 53.

Additionally, I carry out simulations of the TLM test structures where the rear contact geometry (see Figure 43) is accounted for, i.e. the elliptical shape is measured by optical microscopy and transferred, in order to model the elliptical shaped contact in the simulation (see Figure 44 and Figure 45). A shallow BSF of $1\ \mu\text{m}$ depth is assumed. The results of the simulations assuming $\rho_{C,\text{Sim}} = 1 \times 10^{-3}\ \text{m}\Omega\text{cm}^2$ as well as the results of the linear regression of the experimental and simulated TLM measurement are shown in Figure 53 applying Eq. (10). A comparison of the input and the resulting parameters is shown in Table XI.

The comparison of ρ_{base} between experimental four-point probe (4pp) measurements and TLM measurements are in good agreement. The deviations are below $0.1\ \Omega\text{cm}$, which are due to the small temperature differences between the measurements, or measurements uncertainties of 4pp or the thickness.

Table XI. Comparison of the input and the resulting parameters of the TLM measurements and simulations.

	Parameter	Unit	Sample 4.4.6			Sample 4.4.7		
input	$\rho_{\text{base}}^{\text{a}}$	Ωcm	2.73			2.46		
	W	μm	151			154		
	a	μm	57			54		
	b	μm	24			24		
Results calc.	$R_{\text{C-base}}^{\text{b}}$	Ω	2.41			2.34		
	$R_{\text{C,TLM2D}}$ [71]	Ω	1.52			1.40		
Results TLM	$2 \times R_{\text{C,TLM}}^{\text{c}}$	Ω	exp.	sim.	Δ	exp.	sim.	Δ
		Ω	2.49	1.84	0.65	2.61	1.68	0.93
		Ω	1.25	0.92	0.33	1.30	0.84	0.46
		Ωcm^2	0.25	0.17	0.07	0.26	0.17	0.09
		Ω/mm	17.65	17.92	-0.26	16.09	15.84	0.25
	ρ_{base}	Ωcm	2.67	2.71	-0.04	2.48	2.44	0.04

^a Determined by four-point probe (4pp) measurements on the back-etched wafers,

^b see Eq. (44),

^c see Figure 53.

For the derivation of R_{C} , I calculate $R_{\text{C}} / l = R_{\text{C,TLM}}(\text{exp.}) - R_{\text{C,TLM}}(\text{sim.})$ (see Eqs. (10) and (43)), as I assume that $R_{\text{C,TLM}}(\text{sim.})$ equals the ‘intrinsic’, distance independent, component $R_{\text{C-base}}$ of R_{TLM} . The derived $R_{\text{C,TLM}}$ per contact of the TLM measurements are $(0.33 \pm 0.12) \Omega$ and $(0.46 \pm 0.12) \Omega$ higher than the values from the simulations, which is expected, as I just simulate the ‘intrinsic’ R_{C} . Note that the ‘intrinsic’ component of R_{C} in TLM measurements is about 2 – 3 times higher than the derived R_{C} . For the investigated two PERC solar cells with $p = 2 \text{ mm}$, only a weighted series resistance contribution of the rear contacts r_{C} of $0.07 - 0.09 \Omega\text{cm}^2$ is determined, which is below 10 % relative to the (weighted) lumped series resistance r_{S} , considering Figure 50. Note that the analytical solution of the 2D TLM evaluation [126] shows higher R_{C} values than experimentally determined. This is due to the perpendicular extension of the Al-Si eutectic layer, i.e. the elliptical shape of the contact.

The TLM determination method of R_{C} leads to much lower uncertainties than the evaluation method of the weighted series resistance analysis of PERC solar cells with varying f_{met} . The most challenging aspect of the TLM determination method is the description of the contact geometry, i.e. lateral and perpendicular extent of the Al-Si eutectic layer during firing and the formation of the BSF in doping density and depth. For

an estimation of the impact, I perform device simulations of TLM measurements with the parameters of sample 4.4.7, varying the contact depth of an elliptical shaped contact with and without BSF. The results are shown in Figure 54 and are compared to the experimental, simulated and analytical values of Table XI.

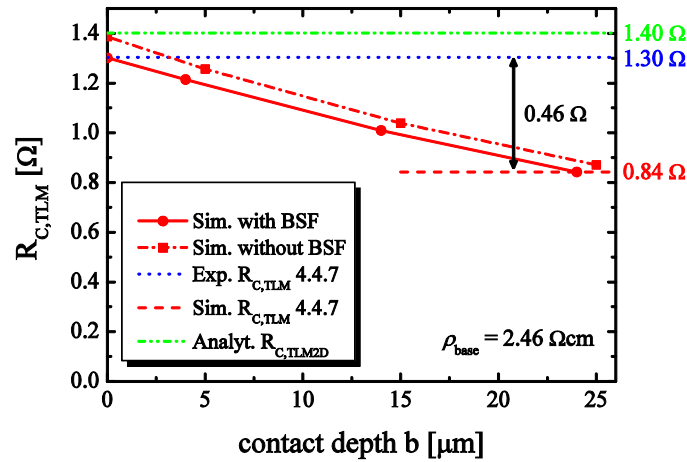


Figure 54: Simulation study of the TLM experiment with a PERC-like test structure with an elliptical contact as shown in Figure 43 varying the contact depth b . The experimental and simulated values of $R_{C,TLM}$ and $R_{C,TLM2D}$ of sample 4.4.7 are added from Table XI as horizontal lines for comparison.

Firstly, I can confirm the derived analytical solution from Ref. [126] for planar contacts ($b = 0 \mu\text{m}$) without BSF to be valid with an uncertainty below 2%. Secondly, the ‘intrinsic’ R_C component of the TLM measurement decreases comparatively strongly with the contact depth b , as expected. The small differences between the simulations with and without BSF can be explained by broadening of the effective contact in depth and width due to the highly conductive BSF. It is concluded that the impact and the knowledge of the contact geometry is important for evaluating TLM measurements and for the derivation of an accurate R_{C-base} . In comparison to the evaluation method of the series resistance analysis of PERC solar cells with varying f_{met} , the uncertainty of R_C is reduced significantly. I recommend deriving R_C of PERC solar cells from TLM measurements, optical microscopy or scanning electron microscopy (SEM) of the contact geometry, and numerical device simulation.

I can confirm the observation of Urrejola et al. [111] that the contact resistance R_C remained constant in their experiments. However, the calculation of the contact resistivity ρ_C , which was found by Urrejola to be apparently decreasing due to a decreasing contact width, is misleading as the ‘intrinsic’ R_C component and the local BSF was not considered in their evaluation. In the Ph.D. thesis of Urrejola [28] (pp. 63), I find the experimental confirmation of my numerical simulations shown in Figure 54 above. In Urrejolas Ph.D. thesis in Figure 6.2 on page 64, a decreasing R_C with increasing Al finger width is shown. However, I propose a new interpretation. As shown in the SEM images of the same figure, the increasing Al finger width increases the contact depth, which accounts for the decreasing R_C as shown in Figure 54.

4.6 Impact of the rear contact resistance on the solar cell performance

For the estimation of the impact of the rear contact resistance on the performance of PERC solar cells, I show on the example of sample 4.4.7 the validity of $R_C = \frac{\rho_C}{a} = \frac{\rho_C}{\frac{1}{2}C}$ (compare Eq. (38)) by comparison of simulated TLM experiments varying the rear contact resistivity ρ_C . For the elliptical shaped contacts the contact cross-section is assumed to be half the circumference of an ellipse $C(a,b) / 2 = 80 \mu\text{m}$. The comparison is shown in Figure 55, where $\rho_{C,calc} = \frac{1}{2}CR_C = \frac{1}{2}Cl \left(R_{C,TLM}(\rho_{C,sim}) - R_{C,TLM}(1\mu\Omega\text{cm}^2) \right)$. For the example of sample 4.4.7, a good agreement between simulated and calculated contact resistivity is derived. Small deviations occur due to the geometrical influence of the shallow BSF. I conclude for typical PERC solar cells that the assumption that the current density is almost constant over the contact is justified for Eq. (38). The assumption may become uncertain for contacts without BSF and/or much lower base resistivity ρ_{base} .

The determined $R_C = (0.46 \pm 0.22) \Omega\text{cm}$ per line contact is used now to carry out a simple estimation on its influence on the weighted rear contact series resistance r_C , the change of the fill factor ΔFF and the change of the cell efficiency $\Delta\eta$. For that, I vary the metallization fraction f_{met} from 1 % to 10 % and determine r_C by Eq. (38) assuming a contact width of $60 \mu\text{m}$. ΔFF , $\Delta\eta$ are determined by $\Delta FF = (r_C \times J_{MPP^2}) / (J_{SC} \times V_{OC})$ and $\Delta\eta = (r_C \times J_{MPP^2}) / E$, respectively.

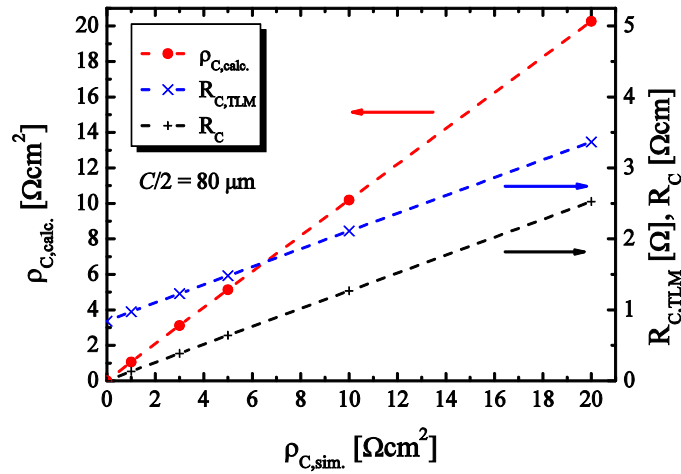


Figure 55: Comparison of the derived rear contact resistivity $\rho_{C,calc.}$ from TLM simulations varying the input rear contact resistivity $\rho_{C,sim.}$. The input parameters equal the TLM simulations of sample 4.4.7 (see Table XI).

I assume a current density at MPP $J_{MPP} = -36 \text{ mA/cm}^2$, $J_{SC} = -39 \text{ mA/cm}^2$, $V_{OC} = 660 \text{ mV}$ and the irradiance under standard test conditions (STC) at $E = 0.1 \text{ W/cm}^2$, which are typical values for PERC solar cells [105] [108]. The results of the estimations are shown in Figure 56.

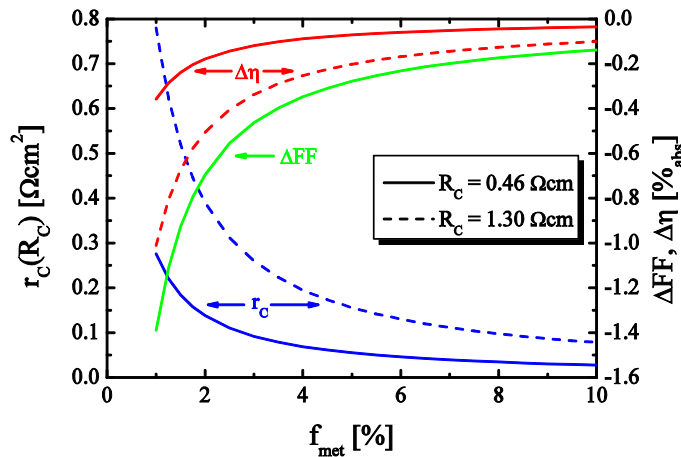


Figure 56: Impact of a variation of f_{met} on the weighted rear contact series resistance $r_C(R_C)$, $\Delta FF(R_C)$ and $\Delta\eta(R_C)$ assuming a contact resistance of $R_C = (0.46 \pm 0.22) \text{ } \Omega\text{cm}$ (proposed TLM evaluation) and $1.30 \text{ } \Omega\text{cm}$ (standard TLM evaluation) per line contact (see Table XI), a contact width of $60 \text{ } \mu\text{m}$, $J_{MPP} = -36 \text{ mA/cm}^2$, $J_{SC} = -39 \text{ mA/cm}^2$ and $V_{OC} = 660 \text{ mV}$.

For a metallization fraction below 3.5 % the rear contact resistance becomes important and results in a FF drop higher than -0.3% _{abs} and a η drop higher than -0.1% _{abs}. Using the standard TLM evaluation, a drop in efficiency of -0.3% _{abs} would be estimated for $f_{\text{met}} = 3.5 \%$.

4.7 Conclusion

For the determination of the rear contact resistance of PERC solar cells, two experimental determination methods are carried out, analyzed and improved. The evaluation schemes may be applied to LFC and LCO contacts, while here LCO line contacts are investigated as an example. The method proposed in Ref. [112] for the series resistance analysis of PERC solar cells with varying metallization fraction f_{met} shows a high uncertainty due to: (1) the choice of the series resistance determination method which determines the overall lumped series resistance r_S level, (2) the voltage at which r_S is evaluated for double or triple light-level methods, (3) the r_S correction procedure while calculating the weighted base series resistance $r_{S,\text{base}}$ which introduces uncertainties especially for a higher pitch where I observe deviations between state-of-the-art analytical solutions and between numerical simulations, and (4) non-optimized production processes and extreme cell working conditions for PERC solar cells with high pitch, even though the derived rear line contact resistance R_C value may be most accurate for a high pitch. For my evaluations, I used the TLL method of three illuminated I-V-curves for the r_S determination at MPP, the analytical base series resistance model of local line contacts proposed by Saint-Cast. An upper limit of R_C is determined to be about $2 \Omega\text{cm}$, but I do not recommend this determination method. In Ref. [112], the weighted series resistance contribution of the base $r_{S,\text{base}}$ is underestimated, which leads to an overestimation of r_C (see Eq. (40)). It results and explains the comparatively high, derived ρ_C of $40 - 55 \text{ m}\Omega\text{cm}^2$.

The second method to determine R_C is to carry out TLM measurements of the electrical separated rear line contacts [111]. For the determination of R_C , the series resistance loss in the thick base has to be considered due to perpendicular current flow above the contacts. It introduces an ‘intrinsic’ series resistance component $R_{C\text{-base}}$ to the contact resistance $R_{C,\text{TLM}}$

determined by TLM. $R_{C\text{-base}}$ may be well determined by numerical simulations considering the base resistivity, the thickness of the base, and additionally the rear line contact geometry. Accounting for $R_{C\text{-base}}$, the R_C determination from TLM measurements is significantly improved. R_C is determined to be below $(0.46 \pm 0.22) \Omega\text{cm}$, which is half of $R_{C\text{-base}}$. The impact on series resistance losses on PERC solar cells is an efficiency drop below 0.1 % for metallization fractions higher than 3.5 %, i.e. the rear contact resistance is currently no significant loss mechanism in *SolarWorld* PERC solar cells.

5. References

- [1] P. Verlinden, Z. YingBin and F. ZhiQiang, "Cost analysis of current PV production and strategy for future silicon PV modules," in *Proc. 28th EU PVSEC*, Paris, France, 2013.
- [2] Kost, C.; Mayer, J.N.; Thomsen, J.; Hartmann, N.; Senkpiel, C.; Philipps, S.; Nold, S.; Lude, S.; Schlegl, T., Fraunhofer - Institut für Solare Energiesysteme (ISE), November 2013. [Online]. Available: <http://www.ise.fraunhofer.de/de/veroeffentlichungen/veroeffentlichungen-pdf-dateien/studien-und-konzeptpapiere/studie-stromgestehungskosten-erneuerbare-energien.pdf>. [Accessed 04. 03. 2014].
- [3] J. Mandelkorn and J. Lamneck, "Simplified fabrication of back surface electric field silicon cell and novel characteristics of such cells," in *Proc. 9th IEEE Photovoltaic Spec. Conf.*, Silver Springs, USA, 1972.
- [4] A. Blakers, A. Wang, A. Milne, J. Zhao and M. Green, "22.8% efficient silicon solar cell," *Appl. Phys. Lett.* vol. 55, p. 1363–1365, 1989.
- [5] M. Lammert and R. Schwartz, "The interdigitated back contact solar cell: A silicon solar cell for use in concentrated sunlight," *IEEE Trans. on Electron Devices* vol. 24(4), p. 337–342, 1977.
- [6] M. Tanaka, M. Taguchi, T. Matsuyama, T. Sawada, S. Tsuda, S. Nakano, H. Hanafusa and Y. Kuwano, "Development of new a-Si/c-Si heterojunction solar cells: ACJ-HIT (Artificially Constructed Junction-Heterojunction with Intrinsic Thin-layer)," *Jpn. J. Appl. Phys.* vol. 31, p. 3518–3522, 1992.

- [7] P. Engelhart, G. Zimmermann, C. Klenke, J. Wendt, T. Kaden, M. Junghänel, K. Suva, B. Barkenfelt, K. Petter, S. Hermann, S. Schmidt, D. Rychtarik, M. Fischer, J. Müller and P. Wawer, "R&D pilot line production of multi-crystalline Si solar cells with top efficiencies exceeding 19%," in *Proc. 37th IEEE Photovoltaic Spec. Conf.*, Seattle, WA, USA, 2011.
- [8] P. Engelhart, D. Manger, B. Klöter, S. Hermann, A. Stekolnikov, S. Peters, H.-C. Ploigt, A. Eifler, C. Klenke, A. Mohr, G. Zimmermann, B. Barkenfelt, K. Suva, J. Wendt, T. Kaden, S. Rupp, D. Rychtarik, M. Fischer, J. Müller and P. Wawer, "Q.ANTUM - Q-Cells next generation high-power silicon cell & module concept," in *Proc. 26th EU PVSEC*, Hamburg, Germany, 2011.
- [9] V. Mertens, T. Ballmann, J. Cieslak, M. Kauert, A. Mohr, F. Stenzel, M. Junghänel, K. Suva, C. Klenke, G. Zimmermann and J. Müller, "Large Area N-type Cz double side contact back junction solar cell with 21.3% conversion efficiency," in *Proc. 28th EU PVSEC*, Paris, France, 2013.
- [10] A. Metz, D. Adler, S. Bagus, H. Blanke, M. Bothar, E. Brouwer, S. Dauwe, K. Dressler, R. Droessler, T. Droste, M. Fiedler, Y. Gassenbauer, T. Grahl, N. Hermert, W. Kuzminski, A. Lachowicz, T. Lauinger, N. Lenck, M. Manole, M. Martini, R. Messmer, C. Meyer, J. Moschner, K. Ramspeck, P. Roth, R. Schönfelder, B. Schum, J. Sticksel, K. Vaas, M. Volk and K. Wangemann, "Industrial high performance crystalline silicon solar cells and modules based on rear surface passivation technology," *Sol. Energ. Mat. Sol. Cells vol. 120*, p. 417–425, 2014.
- [11] A. Lachowicz, K. Ramspeck, P. Roth, M. Manole, H. Blanke, W. Hefner, E. Brouwer, B. Schum and A. Metz, "NO_x-Free solution for emitter etch-back," in *Proc. 27th EU PVSEC*, Frankfurt, Germany, 2012.

-
- [12] Bosch Solar Energy, press release April 2011, [Online]. Available: http://www.bosch-solarenergy.de/media/bosch_se_online/presse/archiv/2011/pdf_3/18_04_11/180411_PERCZelle_engl.pdf. [Accessed 16. 04. 2014].
- [13] D. Kania, T. Böske, M. Braun, P. Sadler, C. Schöllhorn, M. Dupke, D. Stichtenoth, A. Helbig, R. Carl, K. Meyer, A. Grohe, J. Lossen and H.-J. Krokoszinski, "Pilot line production of industrial high-efficient bifacial n-type silicon solar cells with efficiencies exceeding 20.6%," in *Proc. 28th EU PVSEC*, Paris, France, 2013.
- [14] SolarServer, Heindl Server GmbH, Reutlingen, Germany, [Online]. Available: <http://www.solarserver.de/solar-magazin/nachrichten/aktuelles/2013/kw33/photovoltaik-weltrekord-bosch-solar-und-isfh-erreichen-532-watt-spitzenleistung-mit-grossflaechigen-ionenimplantierten-ibc-solarzellen.html>. [Accessed 01. 03. 2014].
- [15] Institut für Solarenergieforschung Hameln (ISFH), Emmerthal, Germany, [Online]. Available: http://www.isfh.de/institut_solarforschung/si-waferzellen.php?_l=1. [Accessed 01. 03. 2014].
- [16] G. Fischer, K. Strauch, T. Weber, M. Müller, R. Schiepe, F. Lottspeich, A. Fülle, F. Wolny, E. Schneiderlöchner, K. Stegemann and H. Neuhaus, "Simulation based development of industrial PERC cell production beyond 20.5% efficiency," in *Proc. 4th SiliconPV*, 's-Hertogenbosch, Netherlands, 2014, in press.
- [17] K. Münzer, J. Schöne, M. Hanke, M. Hein, A. Teppe, J. Maier, R. Schlosser, A. Yodyunyong, K. Varner, H. Habenicht, T. Friess, P. Winter, S. Keller and P. Fath, "Centaurus solar cell technology production," in *Proc. 27th EU PVSEC*, Frankfurt, Germany, 2012.

- [18] J. Zhao, G. Citarella, F. Wunsch, B. Gruber, M. Schorch, M. Richter, S. Pieper, D. Decker, M. Weinke, J. Hausmann, D. Landgraf, D. Sontag, J. Kowalewski, J. Krause and E. Vetter, "Silicon Heterojunction solar cells in Roth & Rau's pilot line: Process performance improvement on mass production tools," in *Proc. 28th EU PVSEC*, Paris, France, 2013.
- [19] G. Fischer, M. Müller, H. Wagner, S. Steingrube and P. Altermatt, "A combined Statistical and TCAD Model as a method for understanding and reducing variations in multicrystalline Si solar cell production," *Energy Procedia vol. 27*, p. 203–207, 2012.
- [20] M. Müller, P. Altermatt, H. Wagner and G. Fischer, "Sensitivity analysis of industrial multicrystalline PERC silicon solar cells by means of 3-D device simulation and metamodeling," *IEEE J. Photovolt. vol. 4(1)*, p. 107–113, 2014.
- [21] M. Müller, G. Fischer, H. Wagner and P. Altermatt, "Understanding and reducing the variations in multicrystalline Si solar cell production," in *Proc. 28th EU PVSEC*, Paris, France, 2013.
- [22] D. Kane and R. Swanson, "Measurement of the emitter saturation current by a contactless photoconductivity method," in *Proc. 18th IEEE Photovoltaic Spec. Conf.*, Las Vegas, NV, USA, 1985.
- [23] M. Müller, P. Altermatt, K. Schlegel and G. Fischer, "A method for imaging the emitter saturation current with lateral resolution," *IEEE J. Photovolt. vol. 2(4)*, p. 586–588, 2012.
- [24] M. Müller, P. Altermatt, K. Schlegel and G. Fischer, "Evaluating the quality of selective emitter structures by imaging the emitter saturation current density," *Energy Procedia vol. 27*, p. 293–299, 2012.

-
- [25] J. Schmidt, N. Thiemann, R. Bock and R. Brendel, "Recombination lifetimes in highly aluminum-doped silicon," *J. Appl. Phys. vol. 106*, pp. 093707-1–093707-4, 2009.
- [26] S. Hermann, Laserstrahlablation von SiO₂-Passivierschichten mit Anwendung auf die RISE-EWT Solarzelle, Hannover, Germany: Ph.D. thesis, Dept. Solar Energy Res., University of Hannover, 2011.
- [27] J.-F. Nekarda, LASER FIRED CONTACTS (LFC) - Charakterisierung, Optimierung und Modellierung eines Verfahrens zur lokalen Rückseitenkontaktierung dielektrisch passivierter Silizium-Solarzellen, Konstanz: Ph.D. thesis, University of Konstanz, Department of Physics, 2012.
- [28] E. Urrejola, Aluminum-silicon contact formation through narrow dielectric openings, Konstanz: Ph.D. thesis, University of Konstanz, Department of Physics, 2012.
- [29] S. Gatz, Analysis and optimisation of industrial type rear-passivated silicon solar cells, Hannover: Ph.D. thesis, University of Hannover, Faculty of Mathematics and Physics, 2013.
- [30] M. Müller and F. Lottspeich, "Evaluation of determination methods of the Si/Al contact resistance of screen-printed passivated emitter and rear solar cells," *J. Appl. Phys. vol. 115*, pp. 084505-1–084505-9, 2014.
- [31] A. Goetzberger, J. Knobloch and B. Voß, Crystalline silicon solar cells, Chichester, West Sussex, England: John Wiley & Sons Ltd., 1998.
- [32] P. Würfel, Physics of solar cells, Weinheim, Germany: WILEY-VCH Verlag GmbH & Co. KGaA, 2005.
- [33] M. Green, Solar cells: operating principles, technology, and system applications., Englewood Cliffs, NJ, USA: Prentice-Hall, Inc., 1982.

- [34] NIST/SEMATECH, "e-Handbook of Statistical Methods," [Online]. Available: <http://www.itl.nist.gov/div898/handbook>. [Accessed 27. 08. 2013].
- [35] J. Kleijnen, Design and Analysis of Simulation Experiments, New York: Springer Science+Business Media, 2012.
- [36] P. Altermatt, "Models for numerical device simulations of crystalline silicon solar cells - a review," *J. Comput. Electron. vol. 10*, p. 314–330, 2010.
- [37] D. Klaassen, "A unified mobility model for device simulation – I. Model equations and concentration dependence," *Solid-State Electron. vol. 35(7)*, p. 953–959, 1992.
- [38] D. Klaassen, "A unified mobility model for device simulation – II. Temperature dependence of carrier mobility and lifetime," *Solid-State Electron. vol. 35(7)*, p. 961–967, 1992.
- [39] TCAD Sentaurus Device version 2011.09. Synopsys, Mountain View, CA, USA, [Online]. Available: <http://www.synopsys.com>. [Accessed 01. 01. 2014].
- [40] A. Schenk, "Finite-temperature full random-phase approximation model of band gap narrowing for silicon device simulation," *J. Appl. Phys. vol. 84(7)*, p. 3684–3695, 1998.
- [41] R. Brendel, "Sunrays: a versatile ray tracing program for the photovoltaic community," in *Proc. 12th EU PVSEC*, Amsterdam, Netherlands, 1994.
- [42] T. Trupke, M. Green, P. Würfel, P. Altermatt, A. Wang, J. Zhao and R. Corkish, "Temperature dependence of the radiative recombination coefficient of intrinsic crystalline silicon," *J. Appl. Phys. vol. 94(8)*, p. 4930–4937, 2003.

-
- [43] P. Altermatt, F. Geelhaar, T. Trupke, X. Dai, A. Neisser and E. Daub, "Injection dependence of spontaneous radiative recombination in crystalline silicon: Experimental verification and theoretical analysis," *Appl. Phys. Lett.* vol. 88, pp. 261901-1–261901-3, 2006.
- [44] A. Richter, S. Glunz, F. Werner, J. Schmidt and A. Cuevas, "Improved quantitative description of Auger recombination in crystalline silicon," *Phys. Rev. B* vol. 86, pp. 165202-1–165202-14, 2012.
- [45] G. Box and K. Wilson, "On the experimental attainment of optimum conditions (with discussion)," *J. Roy. Stat. Soc. B* vol. 13, p. 1–45, 1951.
- [46] N. Metropolis and S. Ulam, "The monte carlo method," *J. Amer. Statist. Assoc.* vol. 44(247), p. 335–341, 1949.
- [47] Sinton Consulting, Boulder, CO, USA, [Online]. Available: <http://www.sintoninstruments.com/>. [Accessed 01. 01. 2014].
- [48] R. Sinton and A. Cuevas, "Contactless determination of current–voltage characteristics and minority carrier lifetimes in semiconductors from quasi-steady-state photoconductance data," *Appl. Phys. Lett.* vol. 69, p. 2510–2512, 1996.
- [49] K. McIntosh and R. Sinton, "Uncertainty in photoconductance lifetime measurements that use an inductive-coil detector," in *Proc. 23rd EU PVSEC*, Valencia, Spain, 2008.
- [50] D. Pysch, A. Mette and S. Glunz, "A review and comparison of different methods to determine the series resistance of solar cells," *Sol. Energ. Mat. Sol. Cells* vol. 91, p. 1698–1706, 2007.
- [51] H. Kampwerth, T. Trupke, J. Weber and Y. Augarten, "Advanced luminescence based effective series resistance imaging of silicon solar cells," *Appl. Phys. Lett.* vol. 98, p. 202102, 2008.

- [52] D. Schroder and D. Meier, "Solar cell contact resistance – a review," *IEEE Trans. on Electron Devices* vol. 31(5), p. 637–647, 1984.
- [53] A. Wolf, D. Biro, J.-F. Nékarda, S. Stump, A. Kimmerle, S. Mack and R. Preu, "Comprehensive analytical model for locally contacted rear surface," *J. Appl. Phys.* vol. 108, pp. 124510-1–124510-13, 2010.
- [54] T. Fellmeth, F. Clement and D. Biro, "Analytical modeling of industrial-related silicon solar cells," *IEEE J. Photovolt.* vol. 4(1), p. 504–513, 2014.
- [55] A. Kimmerle, M. Rüdiger, A. Wolf, M. Hermle and D. Biro, "Validation of analytical modelling of locally contacted solar cells by numerical simulations," *Energy Procedia* vol. 27, p. 219–226, 2012.
- [56] H. Plagwitz and R. Brendel, "Analytical model for the diode saturation current of point-contacted solar cells," *Prog. Photovolt: Res. Appl.* vol. 14, p. 1–12, 2006.
- [57] P. Saint-Cast, M. Rüdiger, A. Wolf, M. Hofmann, J. Rentsch and R. Preu, "Advanced analytical model for the effective recombination velocity of locally contacted surfaces," *J. Appl. Phys.* vol. 108, pp. 013705-1–013705-7, 2010.
- [58] A. Cuevas, "Physical model of back line-contact front-junction solar cells," *J. Appl. Phys.* vol. 113, p. 164502, 2013.
- [59] R. Brendel, "Modeling solar cells with the dopant-diffused layers treated as conductive boundaries," *Prog. Photovolt: Res. Appl.* vol. 20, p. 31–43, 2012.
- [60] A. Fell., "A free and fast 3D/2D solar cell simulator featuring conductive boundary and quasi-neutrality approximations," *IEEE Trans. on Electron Devices* vol. 60(2), p. 733–738, 2013.

-
- [61] M. Rüdiger, M. Rauer, C. Schmiga and M. Hermle, "Effect of incomplete ionization for the description of highly aluminum-doped silicon," *J. Appl. Phys.* vol. 110, pp. 024508-1–024508-7, 2011.
- [62] A. Kimmerle, A. Wolf, U. Belledin and D. Biro, "Modelling carrier recombination in highly phosphorus-doped industrial emitters," *Energy Procedia* vol. 8, p. 275–281, 2011.
- [63] LTspice IV, v. 4.11r, Linear Technology, Milpitas, CA, USA, [Online]. Available: <http://www.linear.com/designtools/software/>. [Accessed 01. 01. 2014].
- [64] P. Altermatt, J. Schumacher, A. Cuevas, M. Kerr, S. Glunz, R. King, G. Heiser and A. Schenk, "Numerical modeling of highly doped Si:P emitters based on Fermi-Dirac statistics and self-consistent material parameters," *J. Appl. Phys.* vol. 92, p. 3187–3197, 2002.
- [65] JMP, Version 9.0, SAS Institute Inc., Cary, NC, USA, 1989-2007. [Online]. Available: <http://www.jmp.com/>. [Accessed 01. 01. 2014].
- [66] H. Wagner, M. Müller, G. Fischer and P. Altermatt, "A simple criterion for predicting multicrystalline Si solar cell performance from lifetime images of wafers prior to cell production," *J. Appl. Phys.* vol. 114(5), pp. 054501-1–054501-8, 2013.
- [67] G. Dingemans and W. Kessels, "Status and prospects of Al₂O₃-based surface passivation schemes," *J. Vac. Sci. Technol. A* vol. 30(4), pp. 040802-1–040802-24, 2012.
- [68] J. Schmidt, J. Moschner, J. Henze, S. Dauwe and R. Hezel, "Recent Progress in the surface passivation of silicon solar cells using silicon nitride," in *Proc. 19th EU PVSEC*, Paris, France, 2004.

- [69] P. Ortega, A. Orpella, I. Martin, M. Colina, G. Lopez, C. Voz, M. Sanchez, C. Molpeceres and R. Alcubilla, "Laser-fired contact optimization in c-Si solar cells," *Prog. Photovolt: Res. Appl.* vol. 20, p. 173–180, 2012.
- [70] R. Woehl, M. Hörteis and S. Glunz, "Determination of the effective optical width of screen-printed and aerosol-printed and plated fingers," in *Proc. 23rd EU PVSEC*, Valencia, Spain, 2008.
- [71] S. Eidelloth, F. Haase and R. Brendel, "Simulation tool for equivalent circuit modeling of photovoltaic devices," *IEEE J. Photovolt.* vol. 2(4), p. 572–579, 2012.
- [72] J. Schmidt and A. Cuevas, "Electronic properties of light-induced recombination centers in boron-doped Czochralski silicon," *J. Appl. Phys.* vol. 86, p. 3175–3180, 1999.
- [73] S. Rein and S. Glunz, "Electronic properties of the metastable defect in boron-doped Czochralski silicon: Unambiguous determination by advanced lifetime spectroscopy," *Appl. Phys. Lett.* vol. 82, p. 1054–1056, 2003.
- [74] K. Bothe, R. Sinton and J. Schmidt, "Fundamental boron-oxygen-related carrier lifetime limit in mono- and multicrystalline silicon," *Prog. Photovolt: Res. Appl.* vol. 13, p. 287–296, 2005.
- [75] W. Thurber, R. Mattis, Y. Liu and J. Filiben, "Resistivity dopant relationship for boron-doped silicon," *J. Electrochem. Soc.* vol. 127, p. 2291–2294, 1980.
- [76] GNU/Octave, Version 3.2.4, Octave community, [Online]. Available: <http://www.gnu.org/software/octave/>. [Accessed 01. 01. 2014].
- [77] J. Müller, K. Bothe, S. Gatz, F. Haase, C. Mader and R. Brendel, "Recombination at laser-processed local base contacts by dynamic infrared lifetime mapping," *J. Appl. Phys.* vol. 108, pp. 124513-1–124513-6, 2010.

-
- [78] WEP (Ingenieurbüro Wolff für Elektronik- und Programmentwicklungen), Furtwangen, Germany, [Online]. Available: <http://www.wepcontrol.com/>. [Accessed 01. 01. 2014].
- [79] R. Bock, P. Altermatt and J. Schmidt, "Accurate extraction of doping profiles from electrochemical capacitance voltage measurements," in *Proc. 23rd EUPVSEC*, Valencia, Spain, 2008.
- [80] D. Meier and D. Schroder, "Contact resistance: its measurement and relative importance to power loss in a solar cell," *IEEE Trans. on Electron Devices vol. 31(5)*, p. 647–653, 1984.
- [81] H. Berger, "Models for contacts to planar devices," *Solid-State Electron. vol. 15*, p. 145–158, 1972.
- [82] H. Murrmann and D. Widmann, "Current crowding on metal contacts to planar devices," *IEEE Trans. Electron Devices vol. 16(12)*, p. 1022–1024, 1969.
- [83] D. Schroder, *Semiconductor material and device characterization*, New York: John Wiley & Sons, Inc., 1998.
- [84] A. Mette, *New concepts for front side metallization of industrial silicon solar cells*, Freiburg: Ph.D. thesis, University of Freiburg, Faculty of Applied Sciences, 2007.
- [85] L. Mak, C. Rogers and D. Northrop, "Specific contact resistance measurements on semiconductors," *J. Phys. E: Sci. Instrum. vol. 22*, p. 317–321, 1989.
- [86] T. Röder, S. Eisele, P. Grabitz, C. Wagner, G. Kulushich, J. Köhler and J. Werner, "Add-on laser tailored selective emitter solar cells," *Prog. Photovolt: Res. Appl. vol. 18*, p. 505–510, 2010.

- [87] J. Müller, K. Bothe, S. Herlufsen, H. Hannebauer, R. Ferré and R. Brendel, "Reverse saturation current density imaging of highly doped regions in silicon: A photoluminescence approach," *Sol. Energ. Mat. Sol. Cells* vol. 106, p. 76–79, 2012.
- [88] J. Müller, K. Bothe, S. Herlufsen, T. Ohrdes and R. Brendel, "Reverse saturation current density imaging of highly doped regions in silicon employing photoluminescence measurements," *IEEE J. Photovolt.* vol 2(4), p. 473–478, 2012.
- [89] A. Cuevas, "The effect of emitter recombination on the effective lifetime of silicon wafers," *Sol. Energ. Mat. Sol. Cells* vol. 57, p. 277–290, 1999.
- [90] C. Reichel, F. Granek, J. Benick, O. Schultz-Wittmann and S. Glunz, "Comparison of emitter saturation current densities determined by injection-dependent lifetime spectroscopy in high and low injection regimes," *Prog. Photovolt: Res. Appl.* vol. 20, p. 21–30, 2012.
- [91] M. Kerr and A. Cuevas, "General parameterization of Auger recombination in crystalline silicon," *J. Appl. Phys.* vol. 91, p. 2473–2480, 2008.
- [92] K. Misiakos and D. Tsamakis, "Accurate measurements of the silicon intrinsic carrier density from 78 to 340 K," *J. Appl. Phys.* vol. 74, p. 3293–3297, 1993.
- [93] P. Altermatt, A. Schenk, F. Geelhaar and G. Heiser, "Reassessment of the intrinsic carrier density in crystalline silicon in view of band-gap narrowing," *J. Appl. Phys.* vol. 93, p. 1598–1604, 2003.
- [94] T. Trupke, R. Bardos, M. Schubert and W. Warta, "Photoluminescence imaging of silicon wafers," *Appl. Phys. Lett.* vol. 89, pp. 044107-1–044107-3, 2006.
- [95] M. Abbott, J. Cotter, F. Chen, T. Trupke, R. Bardos and K. Fisher, "Application of photoluminescence characterization to the development and manufacturing of high-efficiency silicon solar cells," *J. Appl. Phys.* vol. 100, pp. 114514-1–114514-10, 2006.

-
- [96] T. Trupke, R. Bardos and M. Abbott, "Self-consistent calibration of photoluminescence and photoconductance lifetime measurements," *Appl. Phys. Lett.* vol. 87, pp. 184102-1–184102-3, 2005.
- [97] S. Herlufsen, J. Schmidt, D. Hinken, K. Bothe and R. Brendel, "Photoconductance-calibrated photoluminescence lifetime imaging of crystalline silicon," *Phys. Stat. Sol. (RRL)* vol. 2, p. 245–247, 2008.
- [98] S. Herlufsen, J. Schmidt, D. Hinken, K. Bothe and R. Brendel, "Camera-based photoluminescence lifetime imaging of crystalline silicon wafers," in *Proc. 24th EU PVSEC*, Hamburg, Germany, 2009.
- [99] BT Imaging, Sydney, Australia, [Online]. Available: <http://www.btimaging.com>. [Accessed 01. 01. 2014].
- [100] PerkinElmer, Waltham, MA, USA, [Online]. Available: <http://www.perkinelmer.com/>. [Accessed 01. 01. 2014].
- [101] Käfer Messuhrenfabrik, Villingen-Schwenningen, Germany, [Online]. Available: <http://www.kaefer-messuhren.de/>. [Accessed 01. 01. 2014].
- [102] H. Mäckel and K. Varner, "On the determination of the emitter saturation current density from lifetime measurements of silicon devices," *Prog. Photovolt: Res. Appl.* vol. 21, p. 850–866, 2013.
- [103] M. Kessler, T. Ohrdes, P. Altermatt and R. Brendel, "The effect of sample edge recombination on the averaged injection-dependent carrier lifetime in silicon," *J. Appl. Phys.* vol. 111, p. 054508, 2012.
- [104] B. Paviet-Salomon, S. Gall, R. Monna, S. Manuel and A. Slaoui, "Experimental and analytical study of saturation current density of laser-doped phosphorus emitters for silicon solar cells," *Sol. Energ. Mat. Sol. Cells* vol. 95, p. 2536–2539, 2011.

- [105] T. Weber, G. Fischer, A. Oehlke, C. Kusterer, K. Strauch, R. Schiepe, M. Mühlbauer, M. Müller, F. Wolny, R. Köhler, G. Grupp-Mueller, E. Schneiderlöchner, K. Stegemann and H. Neuhaus, "High volume pilot production of high efficiency PERC solar cells - Analysis based on device simulation," *Energy Procedia vol. 38*, p. 474–481, 2013.
- [106] E. Schneiderlöchner, R. Preu, R. Lüdemann, S. Glunz and G. Willeke, in *Proc. 17th EU PVSEC*, Munich, Germany, 2001.
- [107] R. Preu, S. Glunz, S. Schaefer, R. Lüdemann, W. Wettling and W. Pfleging, "Laser ablation - a new low-cost approach for passivated rear contact formation in crystalline silicon solar cells," in *Proc. 16th EC PVSEC*, Glasgow, UK, 2000.
- [108] S. Gatz, J. Müller, T. Dullweber and R. Brendel, "Analysis and optimization of the bulk and rear recombination of screen-printed PERC solar cells," *Energy Procedia vol. 27*, p. 95–102, 2012.
- [109] S. Glunz, A. Grohe, M. Hermle, E. Schneiderlöchner, J. Dicker, R. Preu, H. Mäckel, D. MacDonald and A. Cuevas, "Analysis of laser-fired local back surface fields using n+np+ cell structures," in *Proc. 3rd World Conference on Photovoltaic Energy Conversion*, Osaka, Japan, 2003.
- [110] B. Tjahjono, M. Yang, V. Wu, J. Ting, J. Shen, O. Tan, T. Sziptalak, B. Liu, H.-P. Sperlich, T. Hengst, B. Beilby and K.-C. Hsu, "Optimizing CELCO cell technology in one year of mass production," in *Proc. 28th EU PVSEC*, Paris, France, 2013.
- [111] E. Urrejola, K. Peter, H. Plagwitz and G. Schubert, "Al–Si alloy formation in narrow p-type Si contact areas for rear passivated solar cells," *J. Appl. Phys. vol. 107*, pp. 124516-1–124516-5, 2010.

-
- [112] S. Gatz, T. Dullweber and R. Brendel, "Evaluation of series resistance losses in screen-printed solar cells with local rear contacts," *IEEE J. Photovolt.* vol. 1(1), p. 37–42, 2011.
- [113] E. Urrejola, K. Peter, H. Plagwitz and G. Schubert, "Silicon diffusion in aluminum for rear passivated solar cells," *Appl. Phys. Lett.* vol. 98, pp. 153508-1–153508-3, 2011.
- [114] M. Wolf and H. Rauschenbach, "Series resistance effects on solar cell measurements," *Advanced Energy Conversion* vol. 3, p. 455–479, 1963.
- [115] K. Fong, K. McIntosh and A. Blakers, "Accurate series resistance measurement of solar cells," *Prog. Photovolt: Res. Appl.* vol. 21, p. 490–499, 2013.
- [116] B. Gelmont, M. Shur and R. Mattauch, "Disk and stripe capacitances," *Solid-State Electron.* vol. 38(3), p. 731–734, 1995.
- [117] P. Saint-Cast, Passivation of Si surfaces by PECVD aluminum oxide, Konstanz: Ph.D. thesis, University of Konstanz, Department of Physics, 2012.
- [118] D. Hinken, A. Milsted, R. Bock, B. Fischer, K. Bothe, M. Schütze, J. Isenberg, A. Schulze and M. Wagner, "Determination of the base-dopant concentration of large-area crystalline silicon solar cells," *IEEE Trans. on Electron Devices* vol. 57(11), p. 2831–2837, 2010.
- [119] pv-tools GmbH, Hamelin, Germany, [Online]. Available: <http://www.pv-tools.de>. [Accessed 01. 01. 2014].
- [120] h.a.l.m. elektronik GmbH, Frankfurt am Main, Germany, [Online]. Available: <http://www.halm.de>. [Accessed 01. 01. 2014].
- [121] *IEC 60891*, International Electrotechnical Commission, 1987.

- [122] P. Altermatt, G. Heiser, A. Aberle, A. Wang, J. Zhao, S. Robinson, S. Bowden and M. Green, "Spatially resolved analysis and minimization of resistive losses in high-efficiency Si solar cells," *Prog. Photovolt: Res. Appl.* vol. 4, p. 399–414, 1996.
- [123] H. Plagwitz, Surface passivation of crystalline silicon solar cells by amorphous silicon films, Hannover: Ph.D. thesis, University of Hannover, Faculty of Mathematics and Physics, 2007.
- [124] K. Catchpole and A. Blakers, "Modelling the PERC structure for industrial quality silicon," *Sol. Energ. Mat. Sol. Cells.* vol. 73, p. 189–202, 2002.
- [125] R. Handy, "Theoretical analysis of the series resistance of a solar cell," *Solid-State Electron.* vol. 10, p. 765–775, 1967.
- [126] S. Eidelloth and R. Brendel, "Analytical theory for extracting specific contact resistances of thick samples from the transmission line model," *IEEE Electron Device Lett.* vol. 35(1), p. 9–11, 2014.

6. List of publications

Journals:

- (1) M. Müller, P. P. Altermatt, K. Schlegel, G. Fischer, „A Method for Imaging the Emitter Saturation Current With Lateral Resolution,” *IEEE J. Photovolt.* vol. 2(4), p. 586–588, 2012.
- (2) H. Wagner, M. Müller, G. Fischer, P.P. Altermatt, „A simple criterion for predicting multicrystalline Si solar cell performance from lifetime images of wafers prior to cell production,” *J. Appl. Phys.* vol. 114, p. 054501-1–054501-8, 2013.
- (3) M. Müller, P. P. Altermatt, H. Wagner, G. Fischer, „Sensitivity analysis of industrial multicrystalline PERC silicon solar cells by means of 3D device simulation and metamodeling,” *IEEE J. Photovolt.* vol. 4(1), p. 107–113, 2014.
- (4) M. Müller and F. Lottspeich, „Evaluation of determination methods of the Si/Al contact resistance of screen-printed passivated emitter and rear solar cells,” *J. Appl. Phys.* vol. 115, p. 084505-1–084505-9, 2014.

Conferences:

- (5) M. Müller, J. Isenberg, B. Hund, H. G. Beyer, M. Sedlacek, „Influence of shunt resistance, series resistance and recombination-current on weak light performance of industrial silicon solar cells,” in *Proc. 25th EU PVSEC*, Valencia, Spain, 2010. (Poster)
- (6) M. Müller, A. Schulze, J. Isenberg, B. Hund, H. G. Beyer, „Influence of the wafer resistivity on the temperature coefficients of industrial silicon solar cells and on the expected performance behaviour,” in *Proc. 25th EU PVSEC*, Valencia, Spain, 2010. (Poster)
- (7) S. Malik, M. Sedlacek, M. Müller, M. B. Strobel, A. Krtschil, M. Huchel, L. Seliger, R. Broscheit, H. G. Beyer, „Outddor performance test of different crystalline silicon and thin film PV modules and systems,” in *Proc. 25th EU PVSEC*, Valencia, Spain, 2010.

-
- (8) M. Sedlacek, H. G. Beyer, M. Müller, S. Malik, M. B. Strobel, „Das Projekt Modulertrag im Rahmen des Spitzenclusters Solarvalley Mitteldeutschland - Zwischenstand und erste Ergebnisse,“ *26. Symposium Photovoltaische Solarenergie*, Bad Staffelstein, Germany, 2011.
 - (9) M. Dietrich, G. Fischer, B. Freudenberg, M. Hollatz, M. Müller, M. Reinecke, M. Ramsey, B. Seipel, J. Stenzenberger, „Silicon Crystallization in PV - the Race between Different Techniques Continues,“ *DGKK Jahrestagung*, Freiberg, Germany 2012.
 - (10) M. Müller, P. P. Altermatt, K. Schlegel, G. Fischer, „Evaluating The Quality Of Selective Emitter Structures By Imaging The Emitter Saturation Current Density,“ *Energy Procedia vol. 27*, p. 293–299, 2012. (Poster)
 - (11) G. Fischer, M. Müller, H. Wagner, S. Steingrube, P. P. Altermatt, „A combined Statistical and TCAD Model as a method for understanding and reducing variations in multicrystalline Si solar cell production,“ *Energy Procedia vol. 27*, p. 203–207, 2012.
 - (12) H. Wagner, M. Müller, G. Fischer, P. P. Altermatt, “Modeling of multicrystalline Si solar cells based on lifetime distributions,” in *Proc. 27th EU PVSEC*, Frankfurt, Germany, 2012.
 - (13) T. Weber, G. Fischer, A. Oehlke, C. Kusterer, K. Strauch, R. Schiepe, M. Mühlbauer, M. Müller, R. Köhler, F. Wolny, G. GruppMüller, E. Schneiderlöchner, K.-H. Stegemann, H. Neuhaus, „High Volume Pilot Production of High Efficiency PERC Solar Cells - Analysis Based on Device Simulation,“ *Energy Procedia vol. 38*, p. 474–481, 2013.
 - (14) F. Wolny, T. Weber, M. Müller, G. Fischer, „Light induced degradation and regeneration of high efficiency Cz PERC cells with varying base resistivity,“ *Energy Procedia vol. 38*, p. 523–530, 2013.
 - (15) M. Müller, G. Fischer, H. Wagner, P. P. Altermatt, „Understanding and reducing the variations in multicrystalline Si solar cell production,“ in *Proc. 28th EU PVSEC*, Paris, France, 2013. (Oral)

-
- (16) G. Fischer, K. Strauch, T. Weber, M. Müller, R. Schiepe, F. Lottspeich, A. Fülle, F. Wolny, E. Schneiderlöchner, K. Stegemann und H. Neuhaus, „Simulation based development of industrial PERC cell production beyond 20.5% efficiency,“ in *Proc. 4th SiliconPV*, 's-Hertogenbosch, Netherlands, 2014, in press.
- (17) G. Fischer, M. Müller, P. P. Altermatt, H. Neuhaus, „Yield Enhancement in Advanced Silicon Photovoltaic Production based on TCAD Device Simulation and Statistical Analysis”, *14th European advanced process control and manufacturing (apc|m) Conference*, Rome, Italy, 2014.

Danksagung

Mein großer Dank gilt PD Dr. Pietro P. Altermatt, der mir in den letzten 3 Jahren als Betreuer freundschaftlich zur Seite stand. Sein Vertrauen und seine Zuversicht in mich, seine Anleitung zum wissenschaftlichen Arbeiten, unsere gemeinsame Arbeit im SIMPSONS Projekt waren immer wieder Ansporn an mir zu arbeiten und brachten mir Motivation und Inspiration.

Prof. Dr. Herbert Pfnür möchte ich für seine freundliche Übernahme des Koreferats danken.

Prof. Dr. Achim Schulze danke ich gleichfalls herzlich für die Bereitschaft 3. Korreferent zu sein. Unser gleichzeitiger Start in der Photovoltaik bei Q-Cells mit den gemeinsamen Übungsstunden in Solarzellenphysik und die vertrauensvolle Zusammenarbeit waren mir eine große Freude.

Bei Dr. Gerd Fischer möchte ich mich sehr herzlich für die Betreuung und die Zusammenarbeit im SIMPSONS Projekt bedanken. Unschätzbar sind für mich seine Offenheit, sein strategisches Gespür, seine angewandten Statistikenkenntnisse und die abendlichen Gespräche auf Dienstreisen gewesen.

Mein Dank gilt Dr. Dirk-Holger Neuhaus für seine ansteckende Begeisterung für die Photovoltaik, die wir gemeinsam in seine Vorlesungsreihe „Physik und Charakterisierung von Industriesolarzellen“ einbringen konnten, sowie für die Urheberschaft des Simulationsprojektes SIMPSONS und die fruchtbaren Randbedingungen für meine Zeit als Doktorand bei der SolarWorld Innovations.

Für meine Unterstützung und Förderung an der Hochschule Magdeburg-Stendal, sowie ihr Vertrauen in mich möchte ich Prof. Dr.-Ing. Dieter Haentzsch, Prof. Dr.-Ing. Albert Seidl und Prof. Dr. habil. Hans-Georg Beyer danken. Die Arbeit mit den Magdeburger Studenten in der Vorlesungsreihe „Photovoltaiksysteme an Gebäuden“ in den letzten 4 Jahren war und ist mir immer wieder eine Freude.

Herrn Kristian Schlegel danke ich für seine Hilfe bei der Laserprozessierung während der Herstellung der J_{0e} -Proben mit selektiven Emittern.

Meinem Kollegen Friedrich Lottspeich gilt mein großer Dank für das gemeinsame Experiment und die Diskussionen zur Bestimmung des Rückseitenkontaktwiderstandes von PERC Solarzellen, bei dem er federführend in der Zellherstellung war. Ich wünsche ihm viel Erfolg beim Promovieren.

Meinen Dank richte ich an die Doktoranden in Hannover Hannes Wagner und Tobias Ohrdes, die mir mit Rat und Tat bei Sentauros Device halfen und mich trotz meiner wenigen Hannoverschen Aufenthalte freundschaftlich aufgenommen haben.

Herzlich bedanke ich mich bei Herrn Dr. Eric Schneiderlöchner und Dr. Matthias Wagner für Ihr Korrekturlesen meiner Publikationen und dieser Dissertation, sowie für die Freiheiten in ihren Gruppen, die mir zuteilwurden.

Dank richte ich an alle externen Partner, die mit mir zusammenarbeiteten, besonders Herrn Dr. Karsten Bothe und Dr. Bianca Lim vom ISFH für ihre Einführung in die QSSPC Messung und die Unterstützung des SIMPSONS Projektes, Amir Dastgheib-Shirazi und Michael Steyer von der Universität Konstanz für die Erweiterung meiner Kenntnisse über phosphordiffundierte Emitter, Johannes Greulich und Nico Wöhrle vom ISE für unseren Austausch über optische und elektrische Simulationen mit Sentauros Device, Dr. Jan Bauer und Dr. Otwin Breitenstein vom MPI Halle für ihre Einführung in lokale Solarzellenkennlinien mittels DLIT und die Möglichkeit einen Gastvortrag über numerische Solarzellensimulationen halten zu können.

Den Doktoranden der SWIN Juliane Walter (Danke für 3 Jahre lustige, erfolgreiche und fußballerische Raumteilung), Lydia Lottspeich, Andrey Raykov, Daniel Oriwol, Kaspars Dadzis und Markus Beutel möchte ich für Ihr Interesse am Doktorandentreff, sowie die spannenden fachlichen und wichtigen organisatorischen Gespräche danken. Gleichfalls danke ich den Doktoranden der Graduiertenschule Photovoltaik der TU Bergakademie Freiberg unter Vorsitz von Herrn Robert Zierer für ihre Einladungen zu den Klausurtagungen 2012 und 2013 und der Möglichkeit eigene Gastvorträge einzubringen.

Großer Dank für die herzliche und aufrichtige Arbeitsatmosphäre, für viele fruchtbare Diskussionen, für das gemeinsame Fußballspielen, für das fröhliche Fußballschauen, für die Mittagslaufgruppe gilt meinen Kolleginnen Andrea Reichert, Claudia Hanisch, Franziska Wolny, Irina Große, Jana Jungandreas, Kerstin Strauch, Kristin Herzog, Maria Mühlbauer, Melanie Hentsche, Ramona Fiedler, und meinen Kollegen Alexander Fülle, Alexander Oehlke, Andreas Krause, Bernd Bitnar, Christian Koch, Christian Kusterer, Denny Weller (Vielen Dank für die TLM Testmessung!), Dirk Schulze, Gunter Erfurt, Harald Hahn, Karl-Heinz Stegemann, Lamine Sylla, Martin Kutzer, Michael Wolf, Norbert Finke, Pawel Raschtschepkin, Phedon Palinginis, Philipp Richter, Rene Härtwig, René Köhler, Rico Petereit, Roman Schiepe, Sebastian Gatz, Stefan Steckemetz, meinem Bacheloranten Thomas Robel, Torsten Weber, Wieland Pethe und allen weiteren Kollegen, die zum Gelingen dieser Arbeit beigetragen haben.

Des Weiteren danke ich Herrn Dr. Matthias Strobel für seine Bereitschaft Promotions-erfahrungen zu teilen und mich in meinen Anstrengungen in der Anfangszeit zu fördern.

Wenn der gute Zufall für mich einen Namen bekommen sollte, wäre dieser mit Herrn Jörn Suthues verbunden. Ihm danke ich für die guten Hinweise für mein Berufsleben zur richtigen Zeit am richtigen Ort.

Ich danke meinem Cousin Markus für das Korrekturlesen des TLM Kapitels, sowie meiner ganzen Familie für viele ablenkende Momente.

Mein größter Dank gilt meiner Frau Julia für ihre Rücksichtnahme, Unterstützung und Liebe.

Lebenslauf

Angaben zur Person

Name: Matthias Müller
 Geburtsdatum/-ort: 26.07.1983 in Meiningen
 Familienstand: verheiratet
 Staatsangehörigkeit: deutsch
 Anschrift: Bertholdsweg 29 in 09599 Freiberg

Schulbildung

08/1990 – 07/1994 Grundschule 43. Polytechnische Oberschule Leipzig
 08/1994 – 06/2002 Immanuel-Kant-Gymnasium Leipzig

Zivildienst

07/2002 – 04/2003 Mitarbeiter in der Informations- und Koordinierungsstelle des Deutschen Roten Kreuzes Kreisverband Leipzig Stadt e.V.

Studium

10/2003 Diplomstudium der Physik an der Universität Leipzig
 Schwerpunkte: Halbleiterphysik, Astrophysik,
 Computersimulationen in der Statistischen Physik
 01/2009 Abschluss: „Diplom-Physiker“

Tätigkeiten

11/2007 – 12/2007 Praktikum bei der Firma Q-Cells SE in der Charakterisierungsgruppe
 01/2008 – 01/2009 Diplomarbeit bei der Firma Q-Cells SE zum Thema: „Modellierung und Verifizierung des Jahreswirkungsgrades von Solarzellen“
 02/2009 – 04/2009 Mitarbeiter in der Zellanalysegruppe der Abteilung Forschung und Entwicklung bei der Firma Q-Cells SE
 07/2009 – 12/2009 Mitarbeiter in der Entwicklungsabteilung der GP Inspect GmbH
 02/2010 – 02/2011 Wissenschaftlicher Mitarbeiter an der Hochschule Magdeburg-Stendal
 03/2011 – 02/2014 Mitarbeiter in der Charakterisierungsgruppe der Abteilung Forschung und Entwicklung bei der Firma SolarWorld Innovations GmbH mit der Zielstellung einer Promotion
 Seit 04/2014 Mitarbeiter in der Solarzellenentwicklungsgruppe der Abteilung Forschung und Entwicklung bei der SolarWorld Innovations GmbH
 Seit 10/2010 Lehrbeauftragter an der Hochschule Magdeburg-Stendal: Vorlesung „PV-Systeme an Gebäuden“ im Masterstudiengang
 Seit 04/2012 Lehrbeauftragter an der Technischen Universität Bergakademie Freiberg: Vorlesung „Physik und Charakterisierung von Industriesolarzellen“ im Masterstudiengang